Charles University in Prague

Faculty of Mathematics and Physics

Department of Surface and Plasma Science

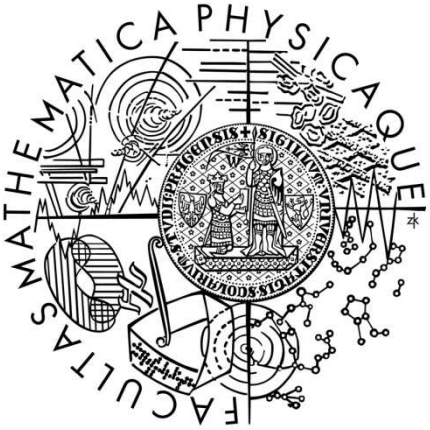

DOCTORAL THESIS

Preparation and Characterization of Novel Oxide Catalysts for Fuel Cell Applications

Mgr. Ivan Khalakhan

Supervisor: Prof. RNDr. Vladimír Matolín, DrSc.

Prague 2013

Acknowledgements

First of all I am very grateful to my supervisor Prof. RNDr. Vladimír Matolín, DrSc. for valuable guidance and support during my study. I would also like to thank my consultant Doc. Mgr. Iva Matolínová, Dr. for useful advises, Dr. Jonathan P. Hill and Dr. Katsuhiko Ariga for their kind support during my stay at the Supermolecules Group of the National Institute of Material Science (NIMS) in Japan.

I would further like to thank Mgr. Mykhailo Vorokhta, Mgr. Martin Dubau, Mgr. Andrii Rednyk, Mgr. Mykhailo Chundak, and Mgr. Roman Fiala for their helpful cooperation in the experiments described in this work. At the end, I would like to thank all my colleagues who warmly accepted me in their Surface Science Team.

I declare that I carried out this doctoral thesis independently, and only with the cited sources, literature and other professional sources.

I understand that my work relates to the rights and obligations under the Act No. 121/2000 Coll., the Copyright Act, as amended, in particular the fact that the Charles University in Prague has the right to conclude a license agreement on the use of this work as a school work pursuant to Section 60 paragraph 1 of the Copyright Act.

Prague date.. signature

Název práce: Příprava a charakterizace nových oxidových katalyzátorů pro palivové články

Autor: Mgr. Ivan Khalakhan

Katedra / Ústav: Katedra fyziky povrchů a plazmatu, Matematicko-fyzikální fakulta Univerzity Karlovy v Praze

Vedoucí doktorské práce: Prof. RNDr. Vladimír Matolín, DrSc., Katedra fyziky povrchů a plazmatu, Matematicko-fyzikální fakulta Univerzity Karlovy v Praze

Abstrakt:

Disertační práce je zaměřena zejména na studium morfologie nových oxidových katalyzátorů pro palivové články s polymerní membránou (PEMFC) připravovaných magnetronovým naprašováním. V této práci byly použity různé metody analýzy povrchů, jako jsou řádkovací elektronová mikroskopie (SEM), mikroskopie atomárních sil (AFM) a rentgenová fotoelektronová spektroskopie (XPS).

V první kapitole je studován vliv různých depozičních podmínek na morfologii naprašovaných vrstev CeO_2, a vrstev CeO_2 dopovaných Au a Pt. Bylo zjištěno, že morfologie a stechiometrie vrstev katalyzátoru je silně závislá na depozičních parametrech a typu použitého substrátu. Dále jsme ukázali, že vrstvy připravované současným naprašováním platiny a oxidu ceru vykazují velmi vysokou katalytickou aktivitu jako anody v PEMFC. Velká plocha povrchu, nízké množství platiny a vynikající katalytické vlastnosti činí z tohoto typu materiálu slibnou alternativu k daleko dražším komerčně dostupným katalyzátorům.

V druhé kapitole byla studována morfologie vrstev PtO_x připravovaných reaktivním magnetronovým naprašování platiny v kyslíkové atmosféře. Ukázalo se, že vzorky PtO_x po redukci H_2 mají nanostrukturní charakter s velkou aktivní plochou povrchu. Takovéto platinové vrstvy jsou rovněž vhodné jako vysoce efektivní katalyzátory pro PEMFC.

Klíčová slova: Oxid Ceru, Platina, Oxid Platiny, Magnetronové Naprašování, Palivový Článek

Title: Preparation and Characterization of Novel Oxide Catalysts for Fuel Cell Applications

Author: Mgr. Ivan Khalakhan

Department/Institute: Department of Surface and Plasma Science, Faculty of Mathematics and Physics, Charles University

Supervisor of the doctoral thesis: Prof. RNDr. Vladimír Matolín, DrSc., Department of Surface and Plasma Science, Faculty of Mathematics and Physics, Charles University

Abstract:

Present doctoral thesis focuses mainly on the morphological investigation of novel oxide catalysts prepared by magnetron sputtering deposition for fuel cell applications. Surface characterization techniques such as scanning electron microscopy (SEM), atomic force microscopy (AFM) and X-ray photoelectron spectroscopy (XPS), were used in this work.

In the first chapter, the influences of different preparation parameters on the morphology of CeO_2, Au doped CeO_2 and Pt doped CeO_2 sputtered films were investigated. It was found that morphology and stoichiometry of the catalyst film is strongly dependent on the deposition parameters and the type of substrate. We have also shown that catalyst films prepared by magnetron co-sputtering of platinum and cerium oxide exhibit high catalytic activity as anode in proton exchange membrane fuel cell (PEMFC). High surface area, low platinum loading and excellent catalytic performance make this material a promising alternative to more expensive commercial catalysts.

In the second chapter, the morphology of PtO_x films prepared by reactive magnetron sputtering of platinum in oxygen atmosphere were examined. It was shown that PtO_x, when reduced by H_2, exhibit large active surface area. Such platinum films were found to be high active catalyst as anode in PEMFC.

Keywords: Cerium Oxide, Platinum, Platinum Oxide, Magnetron Sputtering, Fuel Cell

Preface

The present doctoral thesis is based on experimental work carried out at the Department of Surface and Plasma Science of Charles University in Prague and at the Supermolecules Group of National Institute of Material Science (NIMS) in Tsukuba, Japan within the period from 2008 to 2013 and from 2010 to 2011, respectively. The aim of this work was searching for cheap and efficient anode catalyst for PEMFC.

The main results presented in this work are based on the following original publications:

1. I. Khalakhan, M. Dubau, S. Haviar, J. Lavková, I. Matolínová, V. Potin, M. Vorokhta, V. Matolin. Growth of nano-porous Pt-doped cerium oxide thin films on glassy carbon substrate. *Ceram. Int.*, 2013, **39**, 3765-3769. ISSN 0272-8842.

2. I. Khalakhan, M. Vorokhta, M. Chundak, V. Matolín. Au-CeO_2 nanoporous films/carbon nanotubes composites prepared by magnetron sputtering. *Appl. Surf. Sci.*, 2013, **267**, 150-153. ISSN 0169-4332.

3. M. Vorokhta, I. Khalakhan, I. Matolínová, M. Kobata, H. Yoshikawa, K. Kobayashi, V. Matolín. Nanostructured Pt-CeO_2 thin film catalyst grown on graphite foil by magnetron sputtering. *Appl. Surf. Sci.*, 2013, **267**, 119-123. ISSN 0169-4332.

4. V. Matolín, R. Fiala, I. Khalakhan, J. Lavková, M. Václavů, M. Vorokhta. Nanoporous Pt^{n+}-CeO_x catalyst films grown on carbon substrates. *Int. J. Nanotechnol.*, 2012, **9**, 680-694. ISSN 1475-7435.

5. R. Fiala, I. Khalakhan, I. Matolínová, M. Václavů, M. Vorokhta, Z. Sofer, S. Huber, V. Potin, V. Matolín. Pt-CeO_2 coating of CNTs grown on anode GDL of the polymer electrolyte membrane fuel cell. *J. Nanosci. Nanotechnol.*, 2011, **11**, 5062-5067. ISSN 1533-4880.

6. V. Matolín, I. Matolínová, M. Václavů, I. Khalakhan, M. Vorokhta, R. Fiala, I. Piš, Z. Sofer, J. Poltierova-Vejpravova, T. Mori, V. Potin, H. Yoshikawa, S. Ueda, K. Kobayashi. Platinum-doped CeO_2 thin film catalysts prepared by magnetron sputtering. *Langmuir*, 2010, **26**, 12824-1283. ISSN 0743-7463.

Accept of those papers, the following list consists of original publications in which Mgr. Ivan Khalakhan is co-author but they are not included in present doctoral thesis:

7. S. Haviar, M. Dubau, I. Khalakhan, M. Vorokhta, I. Matolínová, V. Matolin, V. Valeš, J. Endres, V. Holý, M. Buljan, S. Bernstorff. X-ray small-angle scattering from sputtered CeO_2/C bilayers. *J. Appl. Phys.*, 2013, **113**, 024301-7. ISSN 0021-8979.

8. I. Matolínová, R. Fiala, I. Khalakhan, M. Vorokhta, Z. Sofer, H. Yoshikawa, K. Kobayashi, V. Matolín. Synchrotron radiation photoelectron spectroscopy study of metal-oxide thin film catalysts: Pt-CeO_2 coated CNTs. *Appl. Surf. Sci.*, 2012, **258**, 2161-2164. ISSN 0169-4332.

9. M. Unterlass, E. Espinosa, F. Boisson, F. D'Agosto, C. Boisson, K. Ariga, I. Khalakhan, R. Charvet, J.P. Hill. Polyethylenes bearing a terminal porphyrin group. *Chem. Commun*., 2011, **47**, 7057-7059. ISSN 1359-7345.

10. S. Malik, A. Vijayaraghavan, R. Erni, K. Ariga, I. Khalakhan, J.P. Hill. High purity graphenes prepared by a chemical intercalation method. *Nanoscale*, 2010, **2**, 2139-2143. ISSN 2040-3364.

11. V. Matolín, I. Khalakhan, I. Matolínová, M. Václavů, K. Veltruská, M. Vorokhta. $Pt^{2+,4+}$ ions in CeO_2 rf-sputtered thin films. *Surf. Interface Anal*., 2010, **42**, 882-885. ISSN 0142-2421.

CONTENTS

1. OVERVIEW

1.1. Proton exchange membrane fuel cell (PEMFC) – Basic Principles

Rising global energy demands has stimulated humanity to develop alternative sources of energy. However, at the same time ecologically friendly alternatives are required. Those alternatives should have comparable or even better performances than those already existing, but also do not emit carbon dioxide which is a major cause of the so called “Global Warming Effect”. Such requirements give a strong boost to the field of electrocatalysis. Electrocatalysis is the ability of different substances to accelerate the rate of a given electrochemical process when used as an electrode surface under the same conditions. Electrocatalysis became widespread after 1960, mainly as a result of investigations related to fuel cell technology.

A fuel cell is a device which converts the chemical energy from a fuel into electricity through chemical reactions. There are many different types of fuel cells but all of them consist of three main parts: an anode, a cathode and an electrolyte. At the interfaces of these three different parts chemical reactions occur. Fuel cells can be divided into types depending on the kind of chemical reactions that take place in the cell, the temperature range, in which the cell operates, the kind of catalysts and fuel required etc. The following list consists of the most widely used types of fuel cell devices:

- Proton Exchange Membrane Fuel Cells
- Direct Methanol Fuel Cells
- Alkaline Fuel Cells
- Phosphoric Acid Fuel Cells
- Solid Oxide Fuel Cells

The Proton Exchange Membrane Fuel Cell (PEMFC) is one the most promising and challenging subjects of research because it is one of proposed candidates for the practical use of fuel cells in vehicles. PEMFCs convert chemical

energy of the fuel (hydrogen) into electrical energy with high efficiency (~60%). PEMFCs have zero pollutant emissions when using hydrogen as a fuel. One of their distinguishing features is the low operational temperature/pressure ranges (50 to 100 °C)

These advantages make them potentially attractive for a variety of applications including electric vehicles, generation of heat and power in buildings, etc. Fuel cell technology has been used to power automobiles, buses, power generators, and laptop computers [1].

A PEMFC consists of a proton exchange membrane (polymer electrolyte membrane) sandwiched between two electrodes: an anode and a cathode (Fig. 1)

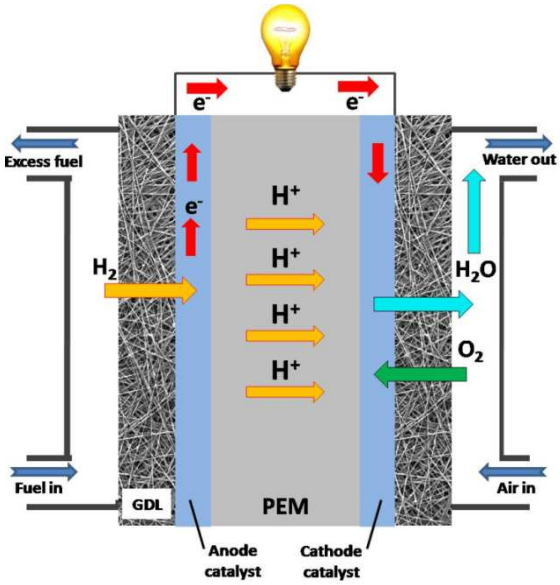

Fig. 1. *Schematic illustration of PEMFC.*

Hydrogen gas flows through channels to the anode, where a catalyst causes the hydrogen molecules to split into protons and electrons.

$$H_2 \rightarrow 2H^+ + 2e^-$$

A proton exchange membrane (PEM) is a membrane designed to conduct protons while being non-transmissive to gases such as oxygen or hydrogen. Hence, it allows only protons to pass through it. In turn, the current of negatively-charged

electrons follows an external circuit to the cathode. This generates electricity which can be used to do work. On the other side of the cell (cathode side), oxygen gas flows through channels to the cathode and react with the electrons, returned from doing work and the protons (which have moved through the membrane) to form water.

$$\tfrac{1}{2}O_2 + 2H^+ + 2e^- \rightarrow 2H_2O$$

Overall reaction in PEM fuel cell can be written as:

$$H_2 + \tfrac{1}{2}O_2 \rightarrow H_2O$$

Commercialization of PEMFCs technology depends on achieving a high specific power and power density for a given cost, so that its characteristics are competitive with traditionally used energy conversion devices.

However, PEM fuel cells are still far from reliable commercial realization, which is mainly caused by two issues: production cost and poor durability and reliability. Catalysts can greatly influence both the cost and the durability of PEM fuel cells, thus, attracting the interest of many researchers in this field.

1.2. Catalyst in PEMFC

In PEM fuel cells, typically platinum based catalysts are used for both reactions: on anode and cathode sides. So far, platinum in pure form or mixed with other elements is considered as the only choice for high and stable performance [2, 3]. As a result, fabrication of such fuel cells is quite expensive. Hence, the most significant barrier that PEM fuel cells had to overcome is the costly amount of platinum required as a catalyst. The early generation of PEMFCs used platinum loadings of 0.12 mg/cm^2. Such catalyst exhibited excellent long-term stable performance but, of course, very high cost [4]. To solve this problem, the development of a low-cost PEMFC system and the search for new, low cost anode materials with high activity has been the focus of researchers in the field of fuel cells over the past few years [5].

To maximize the surface area and minimize the catalyst amount at the same time, Pt nanoparticles which have high surface area-volume ratio were used as the catalyst in PEMFCs. It was found that the catalytic activity of such catalyst is strongly dependent on their particle size, shape, and distribution [6]. To avoid segregation (decreasing platinum surface area) Pt nanoparticles often mixed with some support material (usually carbon).

On the other hand, physical methods such as plasma sputtering of metals [7, 8] and chemical vapor deposition [9] were used for preparing low loaded platinum based electrodes for PEM fuel cell. Platinum films with the Pt amount as low as 0.014 mg/cm^2 have been reported using sputtering methods [10, 11]. Later, it has been shown that thin Pt films prepared using magnetron sputtering at glancing angle deposition (GLAD) conditions have improved catalytic activity due to higher surface area of platinum films [12]. The catalytic activity of those layers was estimated to be comparable with activities of Pt nanoparticles.

Meanwhile, scientist came across the problem that the PEMFC anode catalyst, when operating with hydrogen, is easily poisoning by carbon monoxide (CO) that exist in the fuel (mostly due to manufactured process) [13]. This poisoning can cause performance degradation and sometimes damage to the PEMFC. Such problems have to be resolved for development of long life-time fuel cell system operating in contaminated environments. A promising approach to solve the CO related problem is to increase PEMFC operating temperature because higher temperature operation can reduce the CO negative effects on platinum catalysts. On the other hand Pt based alloys such as PtRu and PtMo have been developed for the improvement of CO tolerance of the Pt anode [14]. It was shown that in the PEMFC at 80ºC PtRu alloys are much more tolerant to CO poisoning than pure Pt electrocatalysts.

The complex nanostructures often show properties that strongly differ from the properties of their components because of so-called support interactions occurring at the interface between the active metal phase and the support [15]. Hence, many oxides have been studied as support materials to promote the catalytic activity of platinum in PEMFCs, including TiO_x [16], WO_x [17], RuO_x [18], SnO_x [19], CeO_x [20] etc. These studies showed that metal oxides have promising effects on the catalytic activity of platinum based PEMFC catalysts.

1.3. Catalyst support in PEMFC

No less attention has been paid to research into the catalyst support (electrode) in PEM fuel cells as they can also influence activity. Support for PEMFC should have high specific area to disperse the catalyst and high electron conductivity to provide electron flow from catalyst to electron collector. In recent years, there has been increasing interest in different carbonaceous materials as heterogeneous catalyst support in the field of electrocatalysis [7, 21, 22]. The physicochemical characteristics and surface chemistry of carbon might also influence the properties of catalysts [23-25]. Platinum based catalyst supported on carbon is one of the most studied systems. The electrocatalytic activity of these catalysts, the effects influencing their performance and their application in fuel cells has been discussed in the literature [25, 26-30].

Preparation of catalyst on the high surface area support can increase the catalyst cost-efficiency. Hence, supports with high specific surface area are used to obtain highly active catalysts. Ordered mesoporous carbons have recently received great attention because of their potential use as catalytic supports in fuel cell electrodes [31, 32]. The advantages of these materials are controllable pore size and high surface area.

In recent years, there has also been increasing interest in carbon nanotubes as heterogeneous catalyst support. The tubular structure of carbon nanotubes makes them unique among different forms of carbon, and they can thus be exploited as an alternative material for catalyst support in fuel cells due to the high surface area, excellent electronic conductivity, and high chemical stability [33, 34]. These catalyst/nanotubes hybrids exhibit interesting structural, electrochemical, electromagnetic, and other properties that are not found in the individual components. A CNTs supported PtRu anode catalyst for direct methanol FC applications has been successfully tested [33-36]. Pt coating of the CNTs in form of supported nanoparticles was also reported [37, 38].

Despite intensive work in this field, the search for a cheap and efficient catalyst for PEMFCs remains a challenge for researchers.

2. EXPERIMENTAL

2.1 Materials

Different types of target and substrate materials have been used in experiments described in this work.

Target materials:
Cerium dioxide (CeO_2)
Platinum (Pt)
Gold (Au)

Substrates:
Silicon wafer, Si (100), (ON Semiconductor)
Multiwall carbon nanotubes (MWCNT), (Sigma Aldrich)
Microporous gas diffusion layer (GDL), (Alfa Aesar)
Highly ordered pyrolytic graphite (HOPG), (Alfa Aesar)
Graphite foil, (Alfa Aesar)
Glassy Carbon (GC), (Alfa Aesar)

2.2. Deposition of composite catalyst thin films. Magnetron sputtering

Magnetron sputtering has rapidly developed in recent years for the deposition of a wide range of important coatings for both industry and research [39]. Schematic illustration of magnetron sputtering process is shown in Fig. 2. It involves ejection of sputtered material from a target by energetic particle bombardment, mostly ions and deposition of it on a substrate. In magnetron sputtering ions (usually Ar ions) are

generated from the plasma. By applying high negative voltage to the target, positively charged ions from plasma are attracted to the target and initiate sputtering.

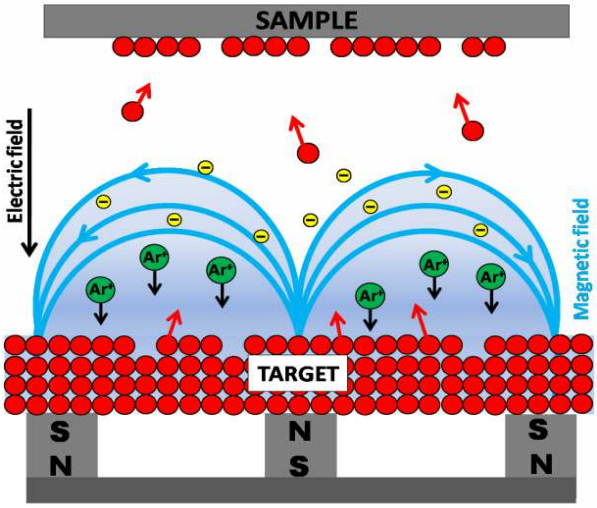

Fig. 2. *Schematic illustration of magnetron sputtering deposition processs.*

There are different kinds of magnetrons. Among them: radiofrequency (RF), direct current (DC), and pulsed DC magnetrons. In this work only DC and RF magnetron sputtering processes were used.

Within the DC sputtering process a negative potential U up to hundred Volts is applied to the target. As a result, the Ar^+ ions are accelerated towards the target, which consists of the material to be deposited. Material is sputtered off from the target and, afterwards, deposited on a substrate. On the other hand secondary electrons are produced which causes a further ionization of the working gas. To increase the ionization rate by emitted secondary electrons, a ring magnet below the target is used in magnetron sputtering. The magnets are arranged in such way that one pole is positioned at the central axis of the target and the second pole is formed by a ring of magnets around the outer edge of the target. The electrons in its field are trapped in cycloids and circulate over the targets surface. In such way higher deposition rate is realized. The dc-sputtering can operate only with conducting materials like metals or doped semiconductors.

The bombardment of a non-conducting target with positive ions results in charging of the surface and to a shielding of the electrical field and eventual

disappearing of the ion current. The solution is to use an alternative current at high frequency. Therefore the RF (radio frequency) sputtering was developed to enable the sputtering of dielectric materials. In the RF sputtering high frequency voltage (typically of 13.56 MHz) is used. In one phase ions are accelerated towards the target surface and sputter material. In the next phase charge neutrality is achieved. The use of RF sputtering allows deposition of any material in general. Ionic and covalent compounds and even polymers may be sputtered away at rates depending on their particular sputtering yield.

Alternatively, for reactive sputtering other working gases in addition to the argon can be used. It can be any gas which will react with the target atoms to form the desired compound. Usually oxygen or nitrogen gases are used to produce oxidic or nitridic films by reactive sputtering.

In this work we used simultaneous magnetron sputtering from two magnetrons: RF magnetron and DC magnetron to prepare catalysts thin films of different composition. Schematic illustration and photo of the deposition equipment is shown on the Fig. 3.

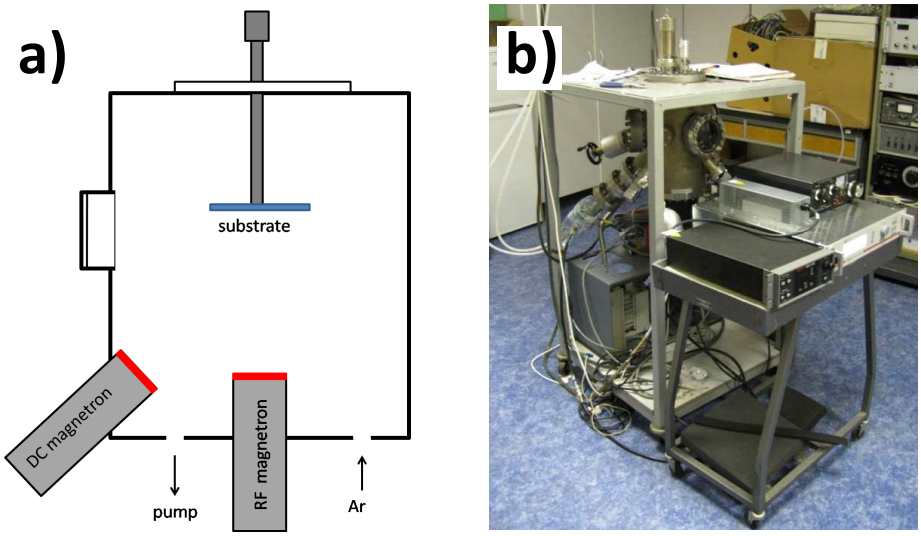

Fig. 3. *a) Schematic illustration; and b) photo of deposition equipment.*

The CeO_2 RF sputtering was performed by using a disk target of 2 inches in diameter at distance of 90 mm from the substrates. Platinum and/or gold were added by using a second DC magnetron tilted by 45° relative to the CeO_2 target.

Simultaneous magnetron sputtering of Pt/Au and CeO_2 allowed us to prepare oxide layers continuously doped with Pt/Au atoms during the films growth.

Deposition was carried out at room temperature of the substrate in an Ar atmosphere by keeping the total pressure in the deposition chamber constant at 2.7 Pa. Additionally, pure oxygen and mixed argon/oxygen atmosphere in deposition chamber can be used in this equipment. The deposition rate of composite catalyst films was about 1 nm/min. It was determined from AFM measurement of the thickness of the films deposited on the silicon substrate. Hence, knowing the film deposition rate, the equivalent film thickness was easily determined from the deposition time. However, the deposition rate can be controlled by varying RF, DC power or pressure in deposition chamber. Concentration of Pt or Au in the metal-cerium oxide composite films can be changed by changing DC power while keeping RF power constant or, conversely, by changing RF power while keeping DC power constant.

Usually substrate and target surface were parallel to each other. A variation of the deposition angle (sputtering under glancing angle deposition (GLAD) conditions) can be achieved by tilting the substrate holder. Thereby, a new preferential direction for the film growth can be produced in this equipment.

2.3. Film characterization

2.3.1. Scanning electron microscopy (SEM)

The scanning electron microscope (SEM) images the topography and structure of samples by collecting variety of signals which occur at the surface of the sample (Fig. 4a) after it has been irradiated by a focused beam of high-energy electrons. The SEM generates a beam of incident electrons in an electron gun, where electrons are produced by a thermal emission source or by a field emission cathode. The energy of the incident electrons can be varied from 100 eV to 30 keV. The electrons are focused into a narrow beam by a series of electromagnetic lenses in the SEM column (see Fig. 4b). The beam of electrons impinging the sample surface can be focused to a final probe diameter as small as 1 nm. The SEM column and sample chamber are at

a vacuum to allow the electrons freely travel from the electron beam source to the sample and then to the detectors.

To create a SEM image, the incident electron beam is scanned over the sample surface in a raster pattern. The emitted signals are detected for each position in the scanned area by a detector. The intensity of the emitted signal is displayed as brightness on a on a computer monitor. Each pixel of computer videomemory is synchronized with the position of the beam on the specimen, and the resulting image is therefore a distribution map of the intensity of the signal being emitted from the scanned area. This map represents the morphology of the sample surface scanned by the electron beam. Magnification in this case is the ratio of the image display size to the sample area scanned by the beam.

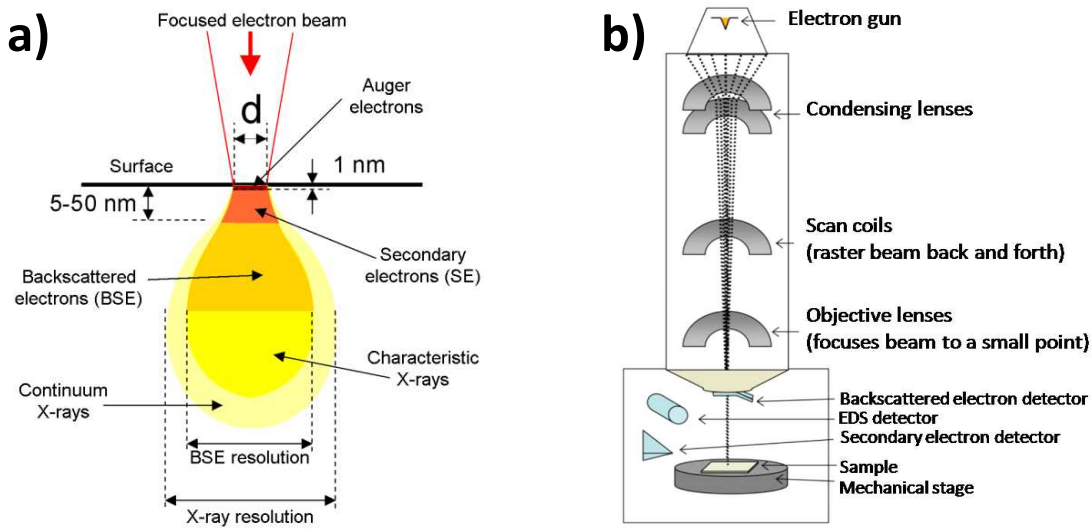

Fig. 4. *a) Generalized illustration of interaction volumes for various electron-sample interactions; b) schematic diagram of SEM equipment.*

There are several SEM operation modes depending on which signal is detected after incident electron-sample interaction.

Secondary electron (SE) imaging mode provides high-resolution imaging of surface morphology. It is the most common imaging mode that collects low-energy (<50 eV) secondary electrons emitted due to inelastic electron scattering. They are ejected from the k-orbitals of the atoms on the sample's surface. The topography of

the surface influences the number of electrons that reach the secondary electron detector from any point on the scanned surface. This local variation in electron intensity creates the image contrast that reveals the surface morphology. The secondary electron image resolution for an ideal sample is almost 1.5 nm.

Backscatter electron (BSE) imaging mode provides image contrast as a function of elemental composition, as well as, surface topography. Backscattered electrons are produced by the elastic interactions between the sample and the incident electron beam. These high-energy electrons (~20 keV) can escape from much deeper regions than secondary electrons, so surface topography is not as accurately resolved as for secondary electron imaging. The intensity of the emitted backscattered electrons signal is proportional to the sample material's atomic number, which results in image contrast as a function of composition, i.e., higher atomic number material appears brighter than low atomic number material because heavier elements reflect more electrons. The optimum resolution for backscattered electron imaging is lower than that for SE detectors and is about 5.5 nm. However, it is possible to use both detectors (SE and BSE detectors) simultaneously to obtain high resolution image and composition contrast.

Qualitative and quantitative chemical analysis can be also obtained using an energy dispersive x-ray spectrometer (EDS) integrated into the SEM instrument. EDS systems includes a sensitive x-ray detector and software to collect and analyze energy spectra. The number and energy of the X-rays, emitted from a sample after interaction with electron beam, can be measured by an energy-dispersive spectrometer. As the energy of the X-rays is characteristic of the difference in energy between the two shells, and of the atomic structure of the element from which they were emitted, this allows to measure the elemental composition of the sample.

Morphology of thin films in this work was examined by means of scanning electron microscopy using TESCAN-MIRA shown in Fig. 5. It is equipped with SE and BSE detectors. However, only secondary electron imaging was performed in experiments, described in this work. It is possible to vary electron beam energy from 1 to 30 kV. The measurements were done at 30 keV electron beam energy and 1×10^{-2} Pa working pressure in the sample chamber.

***Fig. 5**. TESCAN – MIRA scanning electron microscope.*

SEM is also equiped with EDS detector from BRUKER. EDS analysis using ESPRIT software was provided in this work mainly in addition to XPS because it allows us to collect information about the catalyst composition from deeper regions of the layers.

2.3.2. Atomic force microscopy (AFM)

Atomic force microscopy (AFM) is a powerful surface characterization tool, which provides a 3D profile of the surface, by monitoring the forces between a sharp probe (<10 nm) and surface at very small distances (0.2-10 nm). The AFM was developed to overcome a basic problem with STM – that it works only with conducting or semiconducting surfaces. AFM can image almost any type of surface, including polymers, ceramics, composites, glass, and even biological samples. Typically, AFM has a very high vertical resolution (1Å). The lateral resolution of AFM is about 5 nm. A schematic illustration of the main part of the AFM instrument is shown in Fig. 6a. The sharp silicon probe, supported on a flexible cantilever, is a force sensor that deflects as a result of probe-sample interaction.

The force most commonly associated with AFM is an interatomic van der Waals force. The relation between the force and tip-surface distance is shown in Fig. 6b. Usually, the energy of van der Waals force based interaction of two atoms is

described by Lennard-Jones equation, i.e. the interaction potential between two electrically neutral objects:

$$U(r) = -U_0\left[\left(\frac{r_0}{r}\right)^{12} - \left(\frac{r_0}{r}\right)^{6}\right]$$

where U_0 - energy in balance conditions, r_0 - interatomic distance in balance conditions, r - effective interatomic distance.

The total tip-sample interaction energy can be written as:

$$W_{PS} = \int_{Vp}\int_{Vs} U_{LD}(r - r')n_P(r')n_S(r)dVdV'$$

where $n_s(r)$ and $n_p(r')$ are concentrations of atoms in sample and probe respectively.

Hence, the force will be:

$$\vec{F}_{PS} = -\text{grad}(W_{PS})$$

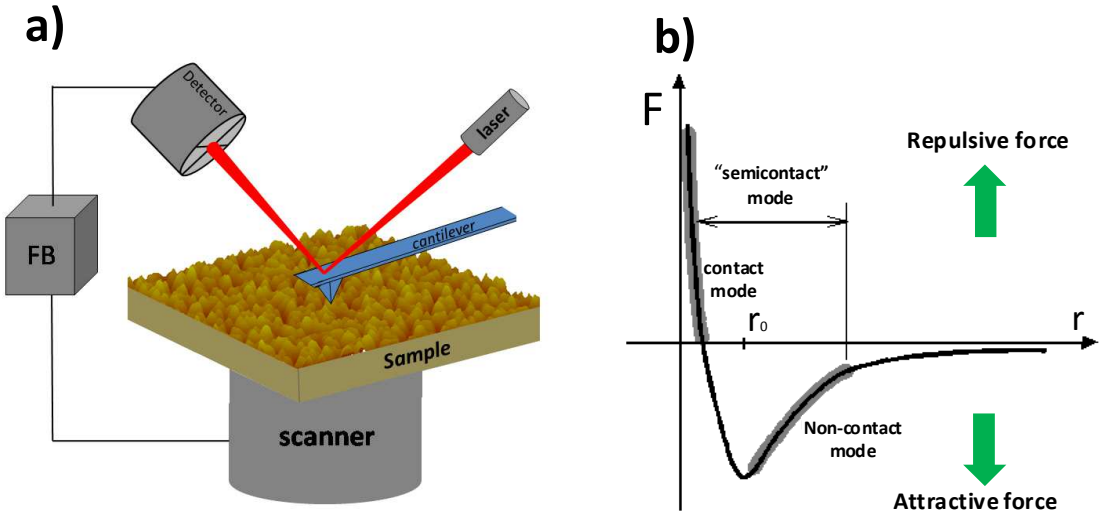

Fig. 6. *a) Schematic illustration of the main parts of AFM; b) force versus tip-sample distance curve.*

The AFM employs an optical detection system in which a diode laser is focused onto the back side of a reflective cantilever and deflects into the center of quadrant photodiode (see Fig. 6a). When the tip scans the surface of the sample it

moving up and down copying the contour of the surface, the deflected laser beam is shifted from the center of quadrant photodiode. The photodetector measures the difference in light intensities between the photodetector's segments, and then converts to voltage. Then, feedback (FB) from the photodiode applies the voltage to the scanner through software control from the computer, in order to maintain a constant height of the tip above the sample. The voltage, which is applied to the scanner, is used to generate a topographic image of the sample.

The AFM can operate in a number of imaging modes. According to the tip-sample interaction during scanning, there are three basic modes of an atomic force microscope: contact mode, non-contact mode, and "semicontact" or "tapping" mode which is intermediate between contact and non-contact modes.

In the contact mode, the relatively soft tip copying the surface relief during scanning while is in direct contact with the sample surface. In this case, the interatomic force between the cantilever and the sample is repulsive (see Fig. 6b). The main disadvantage of this mode is that it can cause damage to the surface during scanning.

In the non-contact region, the tip is oscillated at its resonance frequency with amplitude of about 1 nm and is held on the order of tens to hundreds of angstroms from the sample surface. In this case, the interatomic force between the cantilever and sample is attractive. Tip-surface interaction causes the resonant frequency of the cantilever to shift. The signal applied to the scanner needed to keep the resonance frequency constant is then used to generate a topographic image of the sample. This AFM mode is mostly used in vacuum systems to minimize the influence of surface adsorbates.

In tapping AFM mode the probe tip is oscillated at/or near its resonant frequency with the amplitude of 10-100 nm. The oscillating tip is then scanned the sample at a height where it barely touches the surface. The system monitors the probe position, vibration amplitude and phase to obtain topographical and additionally other proper information (phase contrast mode, amplitude error mode). The advantage of tapping mode over contact mode is that accurate topographical information can be obtained even for very fragile surfaces.

Find out more in detail about AFM technique you can in ref. [40].

The purpose of AFM instrument in this work was to measure the surface roughness of the catalyst films. The surface morphology of sputtered thin films was

examined using AFM “Veeco di MultiMode V”. All AFM measurements were performed at ambient conditions. Sharpened silicon probes with nominal tip radius of curvature 8-10 nm and resonance frequency of 300 kHz were used. Fig. 7 illustrates a detailed scheme of “Veeco di MultiMode V”.

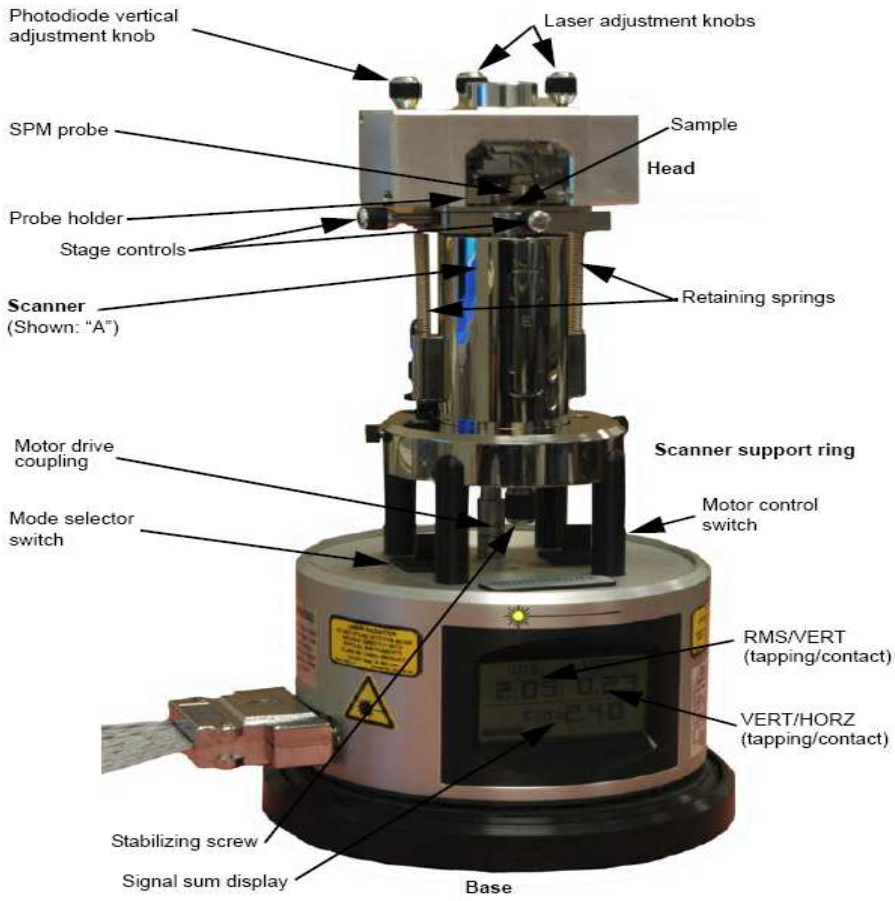

Fig. 7. *Detailed scheme of “Veeco di MultiMode V” AFM.*

In addition to basic AFM modes, “Veeco di MultiMode V” is capable of producing images in a number of other modes, including, magnetic force mode, electrical force mode, etc. However, sputtered thin films in this work were investigated mostly using “tapping” AFM mode.

The surface roughness was calculated from AFM images using “Nanoscope 7.30” software. The roughness parameters should not be considered absolute values of roughness, they merely permit to compare roughness parameters for different samples measured in the same instrument configuration. For each experiment we

used the same type of AFM tip and the same fitting procedure. Surface roughness was expressed by the mean roughness (R_a) parameter, which averages the height relative to the centre plane and it is calculated as:

$$R_a = \frac{1}{L_x L_y} \int_0^{Lx} \int_0^{Ly} |f(x,y)| dxdy$$

where f(x,y) is the surface height relative to the centre plane and L_x and L_y are the dimensions of the surface scan area.

2.3.3. X-ray photoelectron spectroscopy (XPS)

X-ray photoelectron spectroscopy (XPS) is the most widely used surface spectroscopic technique. It allows measuring the elemental composition, chemical state and electronic state of the elements within a measured substrate. Surface analysis by XPS is based on the irradiation of a sample with a beam of X-rays which cause electrons emitting from the sample surface due to photoelectric effect and Auger process. An electron energy analyzer determines the binding energy (energies which are characteristic of the elements within the sampling volume) and number of electrons that escape from the material being analyzed, thus, produce a spectrum of emission intensity versus electron binding energy (Fig. 8). The presence of peaks at particular energies indicates the presence of a specific element in the sample. Moreover, the intensity of the peaks is related to the concentration of the element within the irradiated region.

XPS requires an ultra-high vacuum (UHV) conditions because electron counting detectors in XPS instruments are usually placed above one meter away from the material irradiated by X-rays.

For each element, a unique set of electron binding energies, which corresponds to each core atomic orbital, i.e. each element will give a set of peaks in the photoelectron spectrum at kinetic energies determined by the photon energy and the respective binding energies.

The binding energy of the emitted electrons E_b is given by equation:

$$E_b = h\nu - E_k - \Phi_s$$

Where *hν* – photon energy; E_k – kinetic energy of ejected electrons; Φ_s – is the work function of the spectrometer.

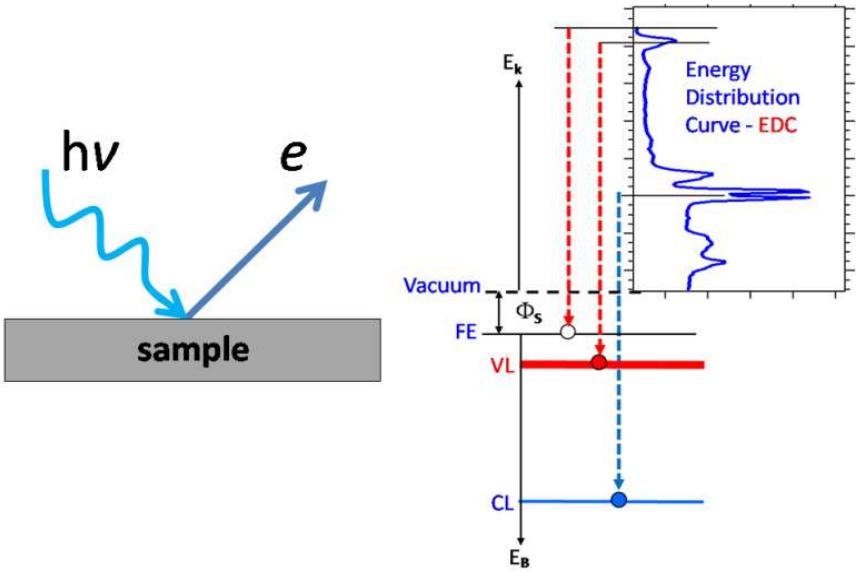

Fig. 8. *Basic principles of X-ray photoelectron spectroscopy.*

As it was already mentioned, XPS peak areas at nominal binding energies can be used to quantify concentration of the elements within the irradiated region. If we assume that the sample M is uniformly illuminated and the entrance aperture of a spectrometer is small, the general expression for the intensity of an XPS peak can be written as:

$$I_A = I_0 \sigma_A(h\nu) T(E_A) D(E_A) \int_0^\infty N_A(z) \exp\left[-\frac{z}{\lambda_M(E_A)\cos\theta}\right] dz$$

where

I_0 is the X-ray flux on the sample,

$\sigma_A(h\nu)$ is the photoionisation cross-section,

$T(E_A)$ is transmission efficiency,

$D(E_A)$ is the electron detector efficiency,

$N_A(z)$ is the A atom distribution with depth z into the sample surface,

$\lambda_M(E_A)\cos\theta$ is the depth from which photoelectrons can be emitted,

It is also important to note that XPS detects only those electrons that have escaped into the vacuum of the instrument, i.e. those, originated from within the top 1 to 10 nm of the material, depending on the X-ray energy. All photo-electrons emitted from deeper parts of the sample are either recaptured or trapped in various excited states within the material.

Since the photoionisation process results in both core-level electron and Auger electron emission in addition to the XPS peaks, measured spectrum also contains the Auger peaks.

In fact, XPS is very complicated technique and learn more in detail about it you can in ref. [41].

The chemical composition and structural properties of the sputtered thin films in this work were analyzed by *ex situ* X-ray photoelectron spectroscopy (XPS). Experiments were performed on an ultra high vacuum system shown in Fig. 9.

Fig. 9. *XPS spectrometer.*

System is built around an UHV spherical experimental chamber pumped by a chain of titanium sublimation pump, a turbomolecular pump and an oil-free scroll rotary pump. The chamber base pressure is in the 10^{-8} Pa range. A preparation chamber is connected to the experimental one and its base pressure is around 5×10^{-6} Pa. XPS system is equipped with an energy analyzer SPECS Phoibos MCD 9 and a dual Mg/Al X-ray source with total energy resolution ΔE = 1 eV. For measurements described in this thesis only Al Kα X-ray source (1486.6 eV) was chosen because lower photon energy of the Mg Kα X-ray source (1253.6 eV) would lead in principle to higher and more inclined non linear Ce 3d spectrum background and consequently to lower peak fitting precision. Mg Kα X-ray source was used only to indentify auger peaks on the photoemission spectra.

The atomic concentration of platinum in the Pt-CeO_2 catalysts was calculated from areas of Ce 3d, Pt 4f and O 1s XPS peaks by using XPS sensitivity factors. However, it should be noted that the obtained values corresponded only to the surface concentration due to surface sensitivity of XPS.

2.3.4. Measurements of the film thickness

Measuring the thickness of the deposited films very precisely is important for the experiments described in this work. Thicknesses were determined using the AFM technique by measuring the height of a step from the substrate surface to the film surface. Step is formed by masking fresh Si substrate by a droplet of varnish during deposition of the films. After deposition, the varnish droplet is removed (see Fig. 10a).

This procedure allows us to obtain the perfect sharp edge (see Fig. 10b) between bare substrate (surface, masked by varnish) and catalyst films on Si (non masked surface). By using an AFM scanning of the surface profile in direction perpendicular to the edge we can calculate the actual film's thickness which directly corresponds to the height of the step on AFM image (see Fig. 10b, c and d). As the vertical resolution of AFM is 1Å, the calculated film's thickness would be very accurate.

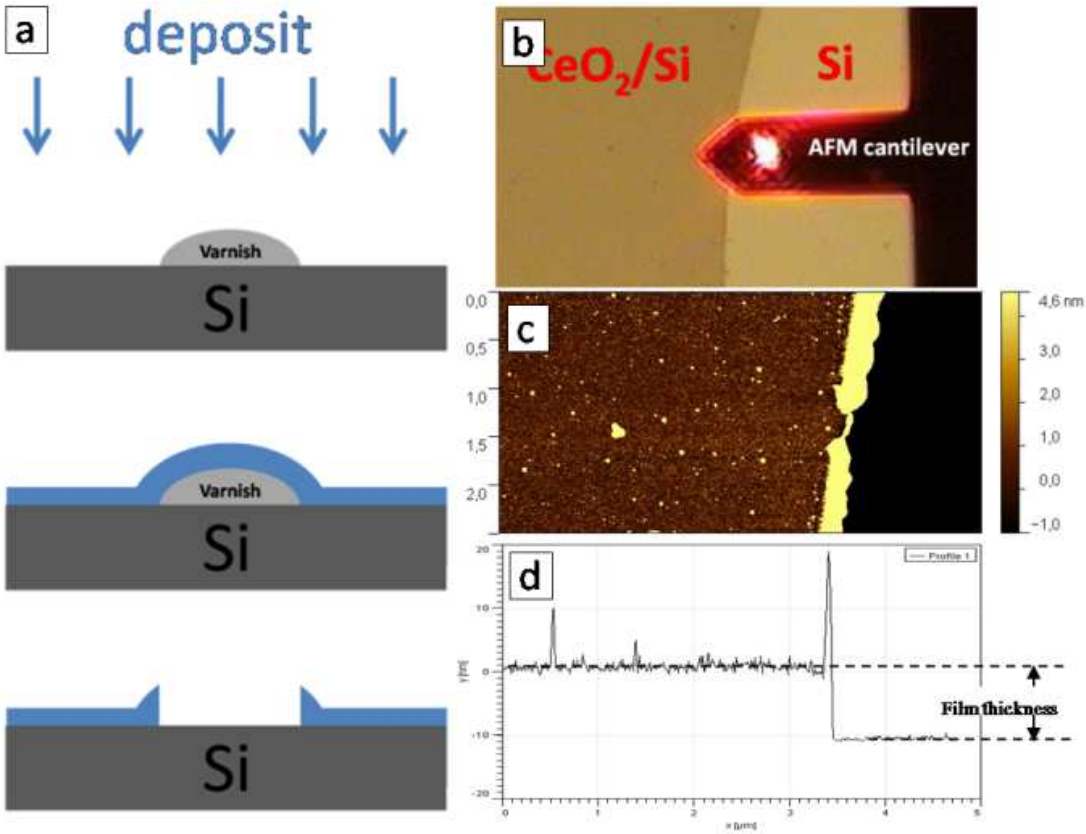

***Fig. 10**. Schematic illustration of the film thickness measurements process using AFM.*

3. RESULTS

3.1. Cerium oxide based catalyst prepared by magnetron sputtering

3.1.1. Introduction

Cerium (cerium oxide, CeO_2) is a member of the lanthanide series of metals and is the most abundant amongst the rare-earth elements in the earth's crust. It exists in two stable stoichiometries: CeO_2 and Ce_2O_3. The electronic structure of the CeO_2 is characterized by unoccupied 4f states of Ce^{4+} whilst the Ce_2O_3 trioxide (Ce^{3+}) has $4f^1$ configuration [42]. CeO_2 is the most stable phase at room temperature and under atmospheric conditions. It is one of the most widely used rare earth metal oxides in catalyst science where it plays an important role because of its unique feature – the Ce^{3+}/Ce^{4+} redox couple, with its ability to switch between CeO_2 and Ce_2O_3 providing the active oxygen in the catalytic reactions [43, 44]. This makes CeO_2 a promising substance either as a support or as an active catalyst. All these properties, combined with the abundance of cerium on earth, make ceria a low-cost highly effective alternative to noble metal catalysts.

CeO_2 crystallizes in the fluorite structure in which each cerium ion is coordinated to eight oxygen neighbours, which makes CeO_2 more stable and the reduction of Ce^{4+} to Ce^{3+} unfavourable. Hence, the promoting effect of pure CeO_2 in oxidation reactions is poor. One of the best solutions to overcome this problem is to create defects or substitute another metal or metal oxide into the ceria lattice. Such modifications in the structure of ceria give new properties to the catalysts, such as density, ionic conductivity, higher catalytic activity [45-47].

Many studies have been published concerning ceria mixed with a noble metal for boosting catalytic activity. Such systems are widely used as a catalyst in different oxidation processes such as oxidation of CO [48], elimination of CO and NO_x

contaminants from automotive exhaust gases [49], water-gas shift reactions [50], oxidation of ethanol [51], and decomposition of methanol [52]. The most studied systems are ceria doped with more active, but at the same time more expensive, metals such as Pd, Pt and Au.

Cerium oxide supported gold catalyst prepared by different methods has been proposed as promising candidate for applications in CO oxidation reactions [53, 54]. It was shown that the catalytic activity of Au clusters supported on ceria increases with increasing concentration of oxidized gold species [55, 56].

One of the most important catalytic properties of ceria is its ability to oxidize hydrocarbons along with carbon monoxide and hydrogen. For these reasons the properties of ceria containing small amounts of Pt have been investigated for the development of PEMFCs [20, 57, 58]. Interaction of ceria with hydrogen leads to formation of higher concentration of Ce^{3+} ions due to surface reduction [59], i.e., creation of oxygen vacancies. Density Functional Theory (DFT) study [60] shows that the adsorption of molecular hydrogen on ceria surface is energetically favoured and depends on the surface structure. Adsorption of H atom causes $Ce^{4+} \rightarrow Ce^{3+}$ reduction of the neighbouring single Ce ion. Pt incorporated in CeO_2 matrix enhance hydrogen molecule dissociation to protonic hydrogen and increase hydrogen storage capacity of the catalyst [61, 62]. Taking all this into account, Pt mixed with CeO_2 looks to be very promising as a heterogeneous catalyst in the field of fuel cell technology.

As already mentioned in the “Overview”, the morphology of a catalyst plays a crucial role in catalytic activity. Increasing the specific surface area of the same amount of catalyst would lead to a significant increase its activity and at the same time will reduce catalyst cost.

It is possible to modify the morphology of deposited films by changing the preparation parameters, such as the deposition methods, working pressure, inert and reactive gas flow, substrate temperature, type of substrates, the film thickness etc [63, 64] and thus to form a catalyst with high surface area. Hence, the deposition process should be optimized to be able to controllably produce a high surface area catalyst. This chapter is devoted to the investigation of the influence of different parameters on structure and surface morphology of CeO_2 as well as Pt-CeO_2 and Au-CeO_2 composite catalyst thin films prepared by magnetron sputtering deposition. Characterization tools such as XPS, SEM and AFM were used to monitor variation

of the surface morphology and the structural properties of catalyst films with deposition parameters. The activity of Pt-CeO_2 anode catalysts prepared by magnetron sputtering deposition was investigated in laboratory-scale PEM fuel cell.

3.1.2. Deposition angle influence

In subsequent section we will investigate the deposition angle influence on the morphology and stoichiometry of sputtered Pt doped CeO_2 catalyst films.

Glancing angle deposition (GLAD) quickly attracted attention of the thin film community. This technique is capable of fabricating ordered nanostructures when the flux of deposited molecules or atoms arrives at an oblique angle from the substrate normal, and under conditions of limited adatom mobility. These lead to the formation of thin films with large surface area [65].

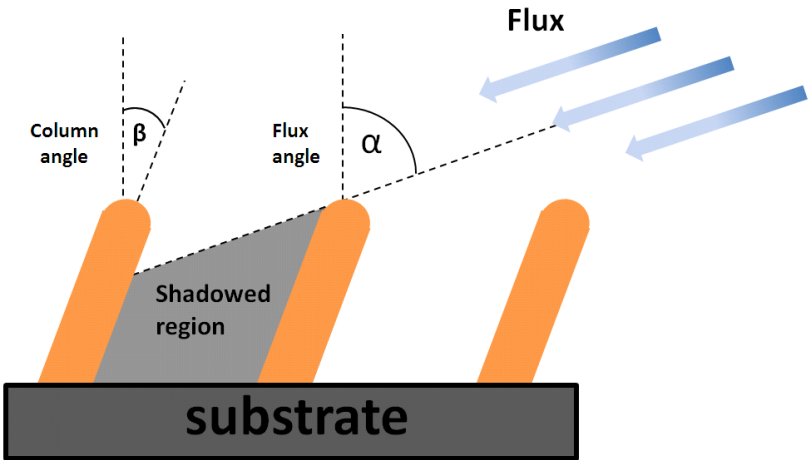

Fig. 11. *Schematic illustration of GLAD process.*

The GLAD process is schematically shown in Fig. 11. It utilize the ballistic self-shadowing effect which occurs when a flux of vaporized atoms or molecules arrives to substrate at oblique angle (>70°). In this case, the growing nuclei shadow the area opposite to incoming flux and therefore the film grows through formation of columnar structures separated from each other by voids and inclined toward the source of the flux [66-69]. All these are perfectly working when using vapor

deposition techniques where the trajectories of deposited atoms are straight lines and the flux is well collimated.

In order to support the assumption about the deposition angle influence on the morphology of thin films prepared by magnetron sputtering deposition technique, where the mean free pass for atoms is limited by relatively high working pressure, we sputtered simultaneously the Pt-CeO_2 thin films on the Si(001) wafer substrates placed in direction parallel and almost perpendicular to the sputtering target, i.e. at normal deposition (ND) and GLAD conditions. The composite films were prepared by using simultaneous magnetron sputtering of Pt and CeO_2 from two targets using two magnetrons: RF magnetron for CeO_2 and DC magnetron for Pt. The thickness of the film was estimated to be around 20 nm. The GLAD angle determined from the deposition distance and size of the circular sputtering target was smaller than 6°s to the surface plane. Argon pressure in the deposition chamber was kept constant at 2.7 Pa.

High resolution SEM was performed for investigation of surface morphology of coated Si(001) substrates. Detailed SEM images of the ND and GLAD samples are shown in Fig. 12 and indicate significant difference in surface morphology between those two samples. The ND sample exhibits relatively flat continuous morphology (Fig. 12a) while the GLAD sample surface is composed of larger grains (Fig. 12b).

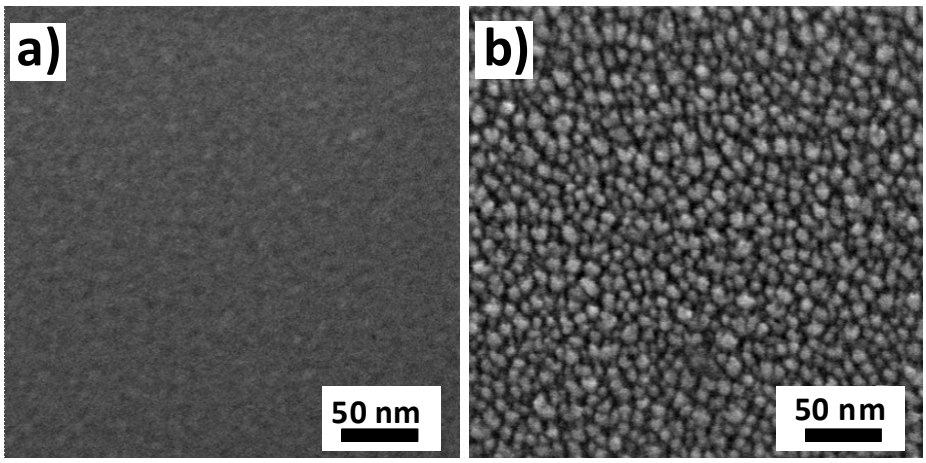

Fig. 12. *SEM images of Pt-CeO_2 thin film sputtered on Si(001): a) ND; b) GLAD.*

The morphology of the Pt-CeO_2/Si(001) was further characterized using atomic force microscopy (AFM). 3-dimensional AFM images (500×500 nm) recorded in height scan mode are plotted in Fig. 13a, b. The film roughness (R_a) for ND and GLAD samples calculated using AFM software were 0.6 nm and 2 nm respectively. The increase of the surface grain size and of the surface roughness suggests that GLAD leads to the formation of columnar structure of the films, which is in agreement with previously published results [66-69]. The important observation of this study was that this changes in morphology lead to significant changes in the chemical composition of the catalyst.

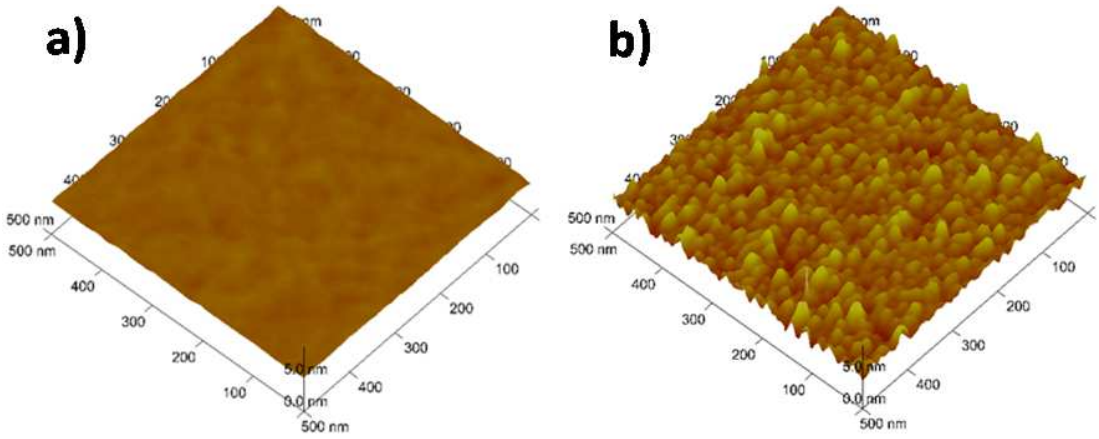

Fig. 13. *AFM images of Pt-CeO_2 thin film sputtered on Si: a) ND; b) GLAD.*

Chemical state and composition of the catalysts were investigated by X-ray photoelectron spectroscopy. The Ce 3d core level XPS spectra of the Pt-CeO_2 film deposited on the flat Si substrate using ND and GLAD conditions are presented in Fig. 14a. The bottom spectrum (ND) consists of three $3d^{3/2}$-$3d^{5/2}$ spin-orbit-split doublets characteristic of stoichiometric CeO_2 (gray lines in Fig. 14a). In Fig. 14a, the upper spectrum (GLAD) shows the XPS Ce 3d spectrum obtained for the film deposited on Si at GLAD conditions. It reveals small contribution of Ce^{3+} states characterized by two additive doublets (blue lines) [70]. Appearance of Ce^{3+} corresponds to a partial reduction of cerium oxide. According to these results we can conclude that the deposition of Pt-CeO_2 at GLAD conditions leads to a partial reduction of cerium oxide.

The corresponding Pt 4f XPS spectra are shown in Fig. 14b. The spectrum of the ND films (see the bottom spectrum) exhibits a Pt $4f^{7/2}$-$4f^{5/2}$ doublet at 74.4-77.8 eV corresponding to Pt^{4+} [71]. In case of GLAD sample (upper spectrum) new doublet appears in addition to Pt^{4+} at energies of 72.7 and 75.9 eV which can be attributed to the Pt^{2+} species [43]. No metallic Pt signal (71 eV) was detected, which showed that platinum atoms in the ceria layers are fully ionic. Mechanism of formation of platinum ionic phases during magnetron co-sputtering of Pt and CeO_2 can be explained in following way. Intensive argon ion bombardment of the CeO_2 target causes emission of cerium and oxygen atoms. Oxygen is mixed with argon in the deposition chamber by forming reactive plasma above the target surfaces. Consequently Pt and Ce atoms travelling through the reactive plasma are oxidized and mixed at the substrate. The hypothesis of an oxygen plasma oxidation of Pt is supported by work of McBride et al [72], showing that reactive sputtering of Pt in oxygen leads to growth of platinum oxide film without any metallic platinum. In addition, one can see that platinum oxidation states and ceria stoichiometry are related somehow. The appearance of Pt^{2+} is accompanied by the formation of reduced ceria.

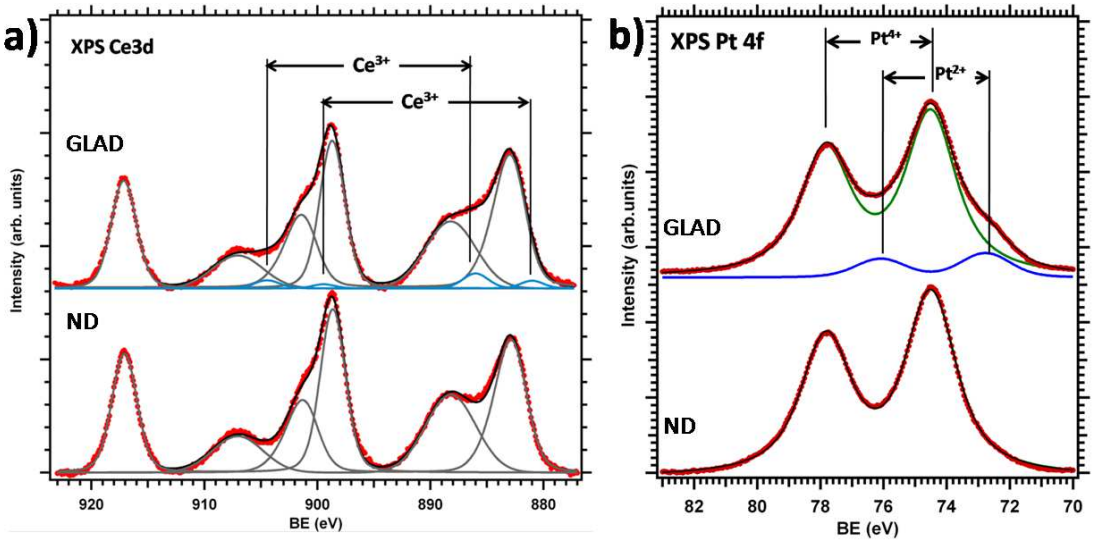

Fig. 14. *XPS a) Ce 3d and b) Pt 4f spectra of Pt-CeO_2 thin film sputtered on Si at ND and GLAD conditions.*

In summary, Pt-doped cerium oxide catalyst films prepared by co-sputtering of Pt and CeO_2 reveal only cationic platinum in Pt^{2+} and Pt^{4+} oxidation states in agreement with our previous published works [73-76]. In the case of the deposition on the Si wafer at glancing angle deposition conditions, we have the formation of Ce^{3+} and Pt^{2+}. Because GLAD leads in general to formation of porous columnar structures, the simultaneous CeO_2 reduction and Pt^{2+} appearance may be related to morphological changes in the films. The reduced character of rough layers can be explained by a general effect of formation of defects and oxygen vacancies at oxide edges and steps [77].

According to the described above results it seems reasonable to expect the same effect in the case of catalyst film deposition on CNTs as well. The main difference between the flat substrate and the CNTs is in the deposition angle. In case of the flat sample we used normal deposition (ND) conditions, while in the case of cylindrical substrates, like CNTs, a noticeable part of the films grow at grazing incidence, i.e. at GLAD conditions. Therefore, it seems reasonable to expect a variation of the film homogeneity as a function of the deposition angle across the single nanotube (Fig. 15a).

To prove our suggestion, Pt-CeO_2 films were deposited on MWCNTs at equal conditions to that described above in this section. Detailed SEM image of the MWCNT/GDL sample coated by Pt-CeO_2 film is shown in Fig. 15b.

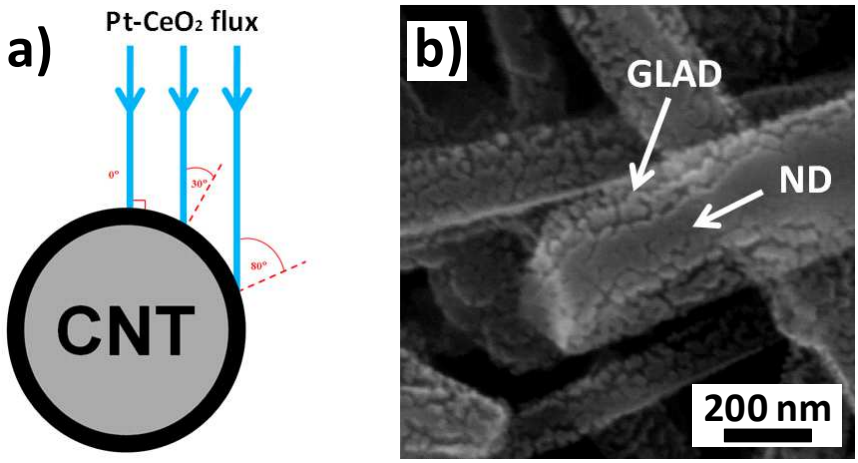

Fig. 15. *a) Schematic illustration of deposition angle variation across single CNT; b) SEM image of the MWCNT/GDL sample coated by Pt-CeO_2 film.*

Indeed, it represents the morphology of the catalyst films characterized by partially porous coating. From this image one can distinguish that the film morphology changes from top part, where the film reveals a compact structure, to side part, where structure is rough.

According to experiments provided in this section, it is obvious that for the preparation of the catalyst films with higher specific surface area we just need to change the angle of deposition or deposit films on cylindrical substrates (CNTs). Additionally, the adjustment of the morphology of the films leads to changes in the chemical composition.

3.1.3. Support influence

The choice of suitable support materials for the PEMFC catalysts is also an important factor that can significantly affect the performances by modifying its catalytic activity. Therefore, to continue our investigations regarding the morphology of Pt-CeO_2 films prepared by magnetron sputtering, we investigated an influence of different types of substrates on the film's morphology. We deposited the catalyst films on different planar substrates at ND conditions. Contrary to the CNTs substrate in this case the deposition angle influence can be excluded and the film thickness is constant across the whole sample.

First, it is essential to measure fresh substrates to be sure its initial roughness will not influence the further growth of the films. Fig. 16 shows AFM images of silicon, graphite foil, HOPG and glassy carbon fresh substrates recorded using height scan mode.

Without proper treating, surface of Si(100) wafer always covered by natural silicon oxide. It should be noted that in all experiments described in this work we will use only as-received Si(100) wafers i.e. covered by silicon oxide. According to AFM investigation the Si wafer substrate has very flat continuous morphology (Fig. 16a). The surface roughness (R_a) determined from presented AFM image was about 0.06 nm.

Bare graphite foil is composed of graphite sheets with a very flat surface (Fig. 16b). Selected AFM image shows hexagonal shallow structures. Each graphite sheet is atomically flat and the thickness of each sheet was estimated to be 0.3 nm.

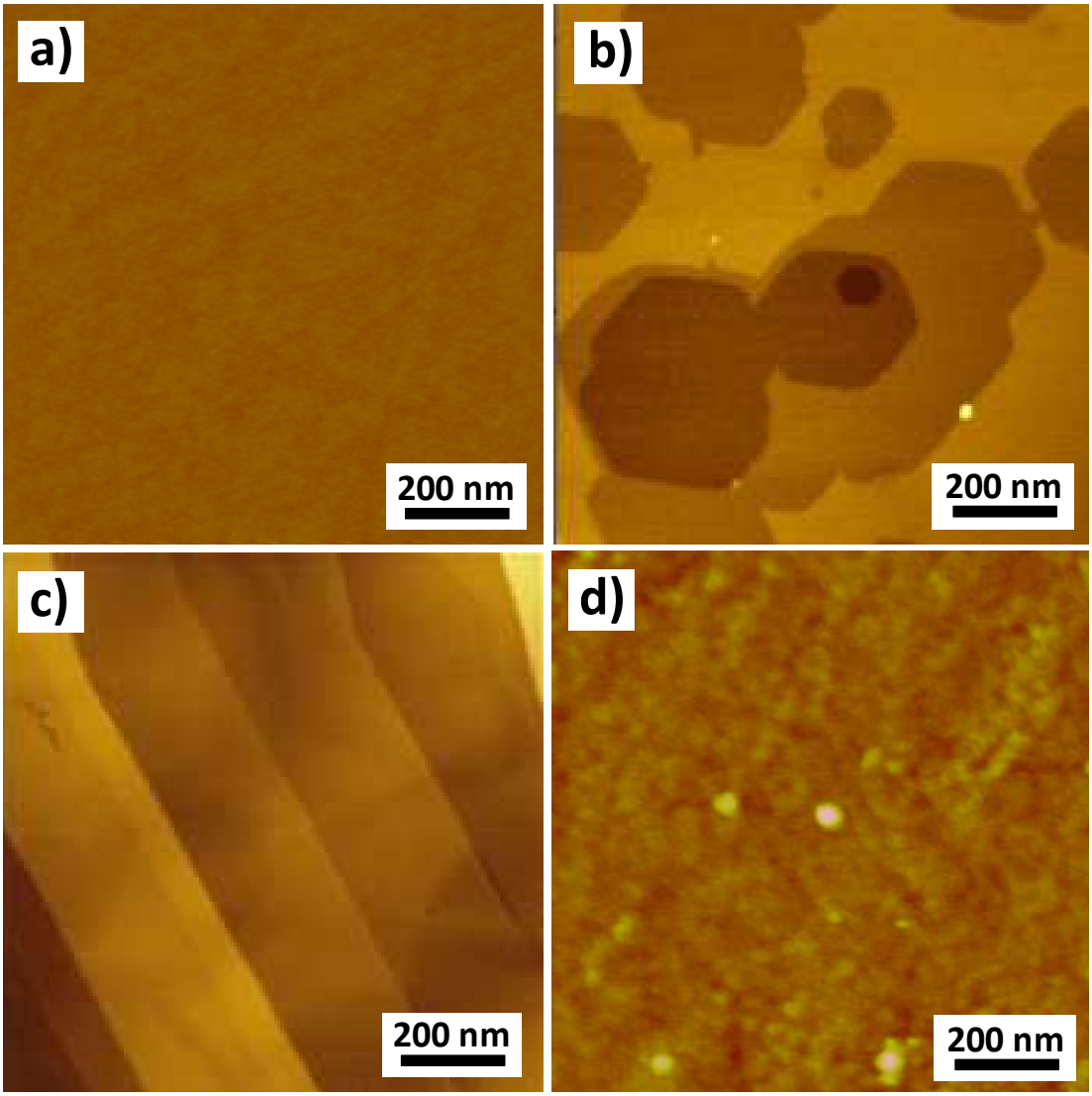

Fig. 16. *AFM images of fresh substrates: a) Si(100); b) graphite foil; c) HOPG; d) glassy carbon.*

Highly ordered pyrolytic graphite (HOPG) is a carbon material with crystalline structure. It is well known that the surface of HOPG is easy to prepare, chemically and thermally stable and it have atomically flat surfaces with large terraces (see Fig. 16c).

Glassy carbon is another interesting carbon material. It is a non-graphitizing carbon which combines glassy and ceramic properties with those of graphite. It has also relatively flat surface (Fig. 16d). The R_a of fresh GC surface was estimated to be about 0.2 nm.

We can conclude that all described above substrates have a relatively flat surface, which can not affect substantially the morphology of sputtered Pt-CeO_2 thin films.

In order to verify how the Pt-ceria catalysts would interact with different types of substrates we first deposited 20 nm thick catalyst films simultaneously on the silicon and graphite foil wafers placed together on the sample holder of the deposition system. We used the same deposition parameters as described in previous section (see "Deposition angle influence" section). Selected SEM images representing the substrate influence on morphology of the films are shown in Fig. 17. The high resolution micrographs of the silicon reveal a homogeneous surface structure giving no structural features resolved by SEM (Fig. 17a). Contrarily, Fig. 17b shows very rough surface morphology of the catalyst film deposited on graphite foil.

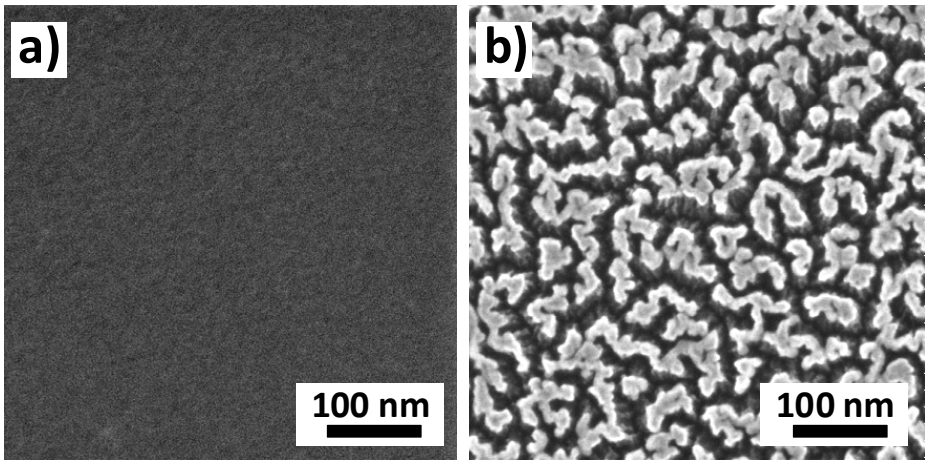

Fig. 17. *SEM images of Pt-CeO_2 films sputtered on different substrates: a) Si(100); b) graphite foil.*

We additionally carried out inspection of the same samples by AFM. In Fig. 18a and b we show AFM images of Pt-CeO_2/Si and of Pt-CeO_2/graphite foil respectively. Calculated surface roughness (R_a) showed a dramatic difference in morphology between those two samples: 0.1 nm for films deposited on silicon and 6 nm for Pt-CeO_2 on graphite foil, which confirms SEM investigation.

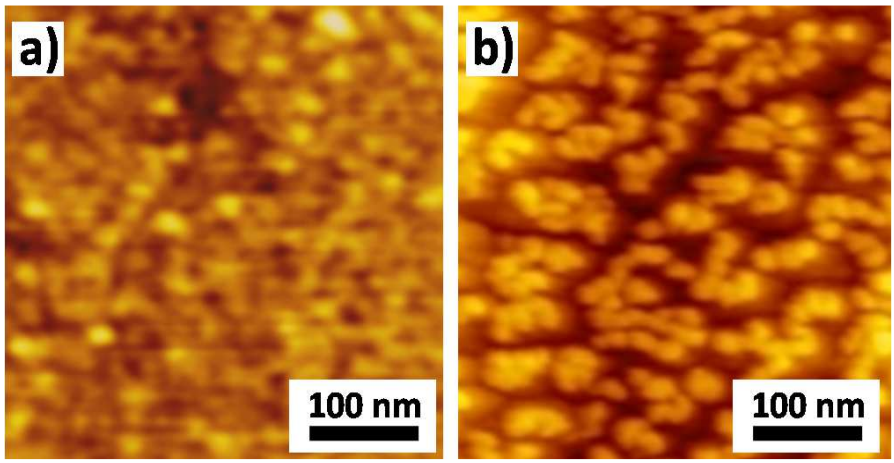

Fig. 18. *AFM images of Pt-CeO_2 films sputtered on different substrates: a) Si(100); b) graphite foil.*

It should be also noted that the same flat structure as observed for the silicon substrate were obtained for copper and gold substrates (not shown herein). These results clearly showed that an interaction with the carbon substrate played a crucial role in predetermination of the growth mode of the Pt-CeO_2 films prepared by magnetron sputtering.

We should emphasize that even ND on carbon substrates leads to the formation of extremely rough structure. Therefore, in addition to the graphite foil we deposited Pt-ceria composite films at conditions equal to those described above, on different types of carbon substrates: MWCNTs, HOPG and GC.

Fig. 19a and b represent SEM images of Pt-CeO_2 films deposited on MWCNTs at different magnifications. We can see that the catalyst film exhibits very rough structure in the case of MWCNTs substrate as well. Comparing with our previous results (See “Deposition angle influence” section), where the morphology of the films deposited on MWCNTs was inhomogeneous with nonporous parts due to the

effect of the deposition angle (see Fig. 15b), in this case catalyst films exhibit higher porosity over the whole MWCNT. From these results, it can be assumed that besides the deposition angle influence, carbon substrate drastically affect the morphology of the deposited Pt-ceria films in the case of deposition on MWCNTs.

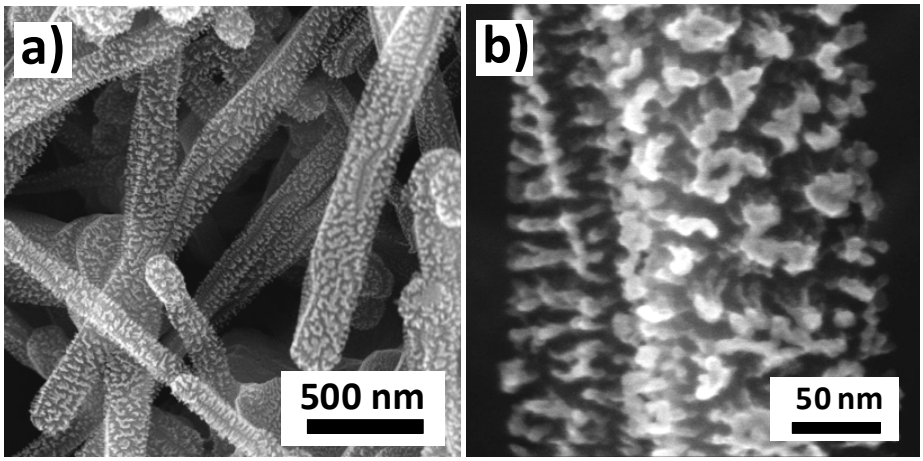

Fig. 19. *SEM image of MWCNTs coated by the porous catalyst films at different magnifications.*

The additional information about the film morphology can be obtained from the side view of coated MWCNT (Fig. 20a). From this image one can clearly distinguish well separated columnar-like structure of deposited films. This image also shows that even screened side of the coated MWCNTs (opposite to the sputtering target) is covered with the catalyst film which can be explained by the surface diffusion of deposited species and/or by scattering of incoming particles with background Ar atoms.

In order to obtain AFM image of CNT covered by the catalyst, the pristine nanotubes were first dispersed in N,N-dimethylformamide (DMF) at a concentration of 1 mg/30 mL in ultrasonic bath and then deposited onto a Si wafer using spin-coater. This technique allows us to prepare separated nanotubes on a flat substrate and avoid the formation of nanotubes bunches which is more suitable for AFM measurements. After this we deposited Pt-CeO_2 films on those nanotubes. Fig. 20b represents corresponding AFM image of single MWCNT covered by the catalyst film.

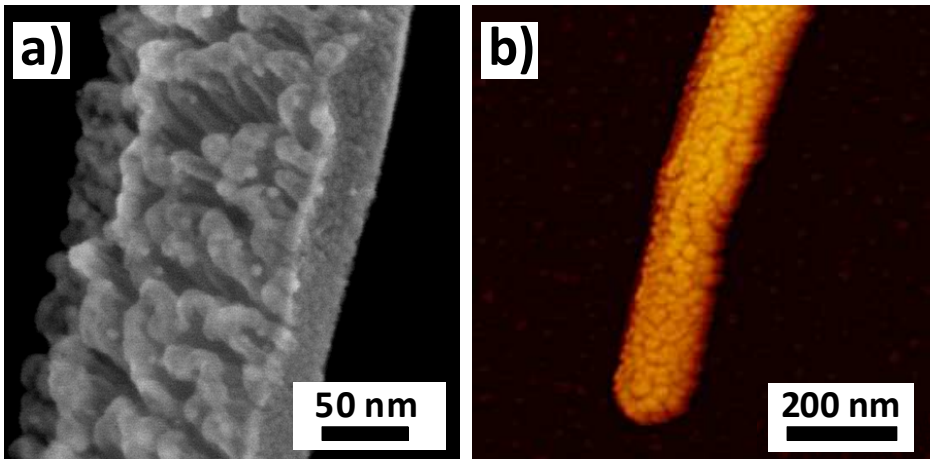

Fig.20. *a) SEM image of MWCNT coated by the porous catalyst film (side view); b) AFM image of single MWCNT covered by the Pt-CeO_2 catalyst.*

It confirms the rough character of the films observed by SEM. Film roughness calculated from this image along MWCNT was around 7 nm, which is even higher than in case of catalyst films deposited on flat carbon substrate (see Fig. 18b). This can be explained by deposition angle influence additionally to the carbon influence on the film growth.

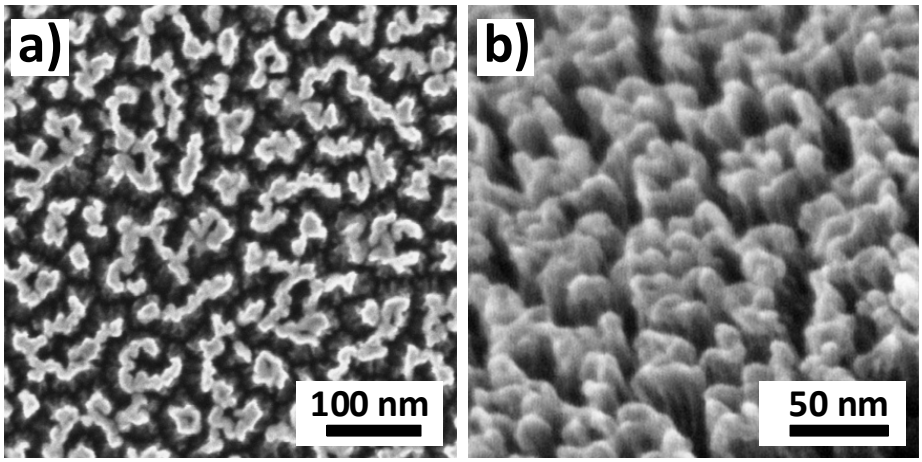

Fig. 21. *SEM image of HOPG coated by the Pt-CeO_2 catalyst: a) normal view; b) tilted view.*

On Fig. 21a we show the SEM image of the catalyst films deposited on HOPG. We can see that we obtained the same morphology of the films, as in case of the

graphite foil substrate (see Fig. 17b). High porosity of the films is given by a growth of catalyst islands separated by open, voided boundaries. Due to planar character of the sample we could also check the layer vertical morphology by using a tilted view. The sample was tilted by 45° relative to the surface normal towards the view plane. The tilted SEM image (Fig. 21b) showed columnar growth of the deposit as in case of the MWCNT substrate (see Fig. 20a). The vertical structures are composed of bonded vertical nanorods forming together wall like structures.

Fig. 22 contains the SEM images of the same catalyst films deposited on flat glassy carbon, i.e. on non-crystalline carbon substrate. We can again see that we obtained similar films morphology to that of the HOPG substrate in Fig. 21a and graphite foil in Fig. 17b. High porosity of the film again is given by a growth of well separated catalyst islands which seems to be a little bit smaller regarding the previous cases.

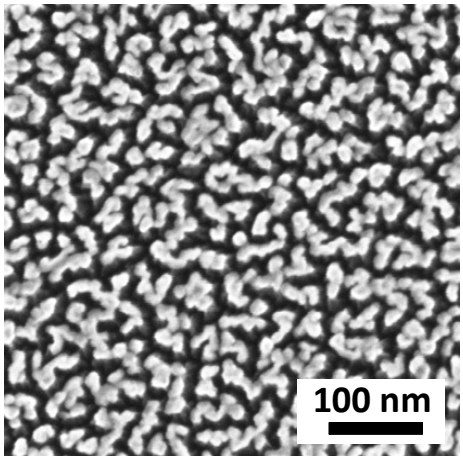

Fig. 22. *SEM image of glassy carbon coated by the Pt-CeO_2 catalyst.*

The results obtained on different carbon substrates suggest that the observed catalyst-support interaction is a general behavior of the platinum-ceria film interaction with any type of carbon surface.

In summary, we have found that morphology of Pt-ceria composite films prepared by magnetron sputtering depends on the type of substrate. It leads to the formation of extremely rough structure when deposited on carbon substrates.

It is likely that growing mechanism and stoichiometry of the films also depend on working conditions, particularly gas pressure, oxygen concentration in the plasma, the deposition speed etc. For better understanding of this complex process, further study focused on influence of working parameters is necessary.

3.1.4. Doping influence

In this section we investigated Pt and Au doping influence on morphology of metal-cerium oxide co-sputtered films deposited on carbon substrates.

3.1.4. 1. Platinum doped CeO_2 films

In order to do this we first deposited cerium oxide doped with Pt and undoped cerium oxide films on graphite foil at equal conditions. The thickness of the films was estimated to be about 20 nm in both cases. Pt concentration determined by XPS for Pt doped CeO_2 film was about 4 at% relative to a total amount of Ce and O atoms.

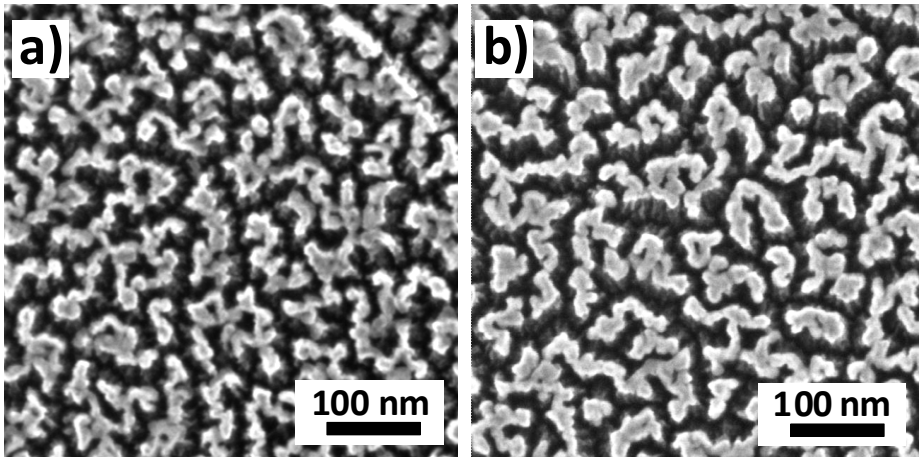

Fig. 23. *a) CeO_2; b) Pt-CeO_2 films deposited on graphite foil.*

Fig. 23 represents selected SEM images of CeO_2 (Fig. 23a) and Pt-CeO_2 (Fig. 23b) films. These images clearly demonstrate that there is no significant influence of platinum on the films growth. In both cases films reveal similar (very

rough) morphology. Therefore one can conclude that embedded Pt atoms do not make significant influence and porous films are given only by interaction of CeO_2 with carbon substrate.

3.1.4.2. Gold doped CeO_2 films

More precisely we studied the effect of CeO_2 doping by gold. We used MWCNTs as the substrate for this investigation.

In order to investigate sputtered thin film properties we first prepared two samples with different thickness of CeO_2 films sputtered on MWCNTs: CeO_2 (10 nm) and CeO_2 (30 nm). High resolution SEM was used for investigation of surface morphology of the CeO_2 coated MWCNTs. Detailed SEM observation of CeO_2 films with different thicknesses, deposited on MWCNTs is presented in Fig. 24a, b.

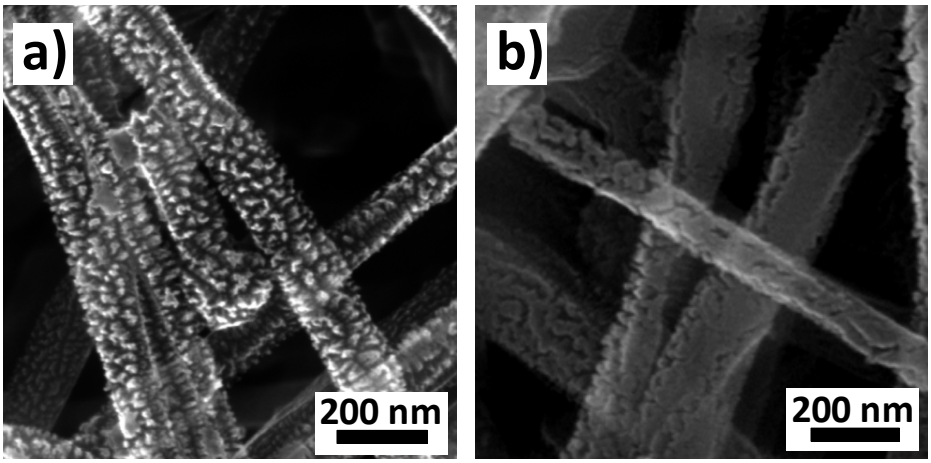

Fig. 24. *SEM image of CeO_2 films with different thicknesses on MWCNTs: a) 10 nm; b) 30 nm.*

These images show that the roughness is decreasing with increasing film thickness. The thinner CeO_2 film (10 nm) reveals highly porous structure with isotropic porosity over the whole coated MWCNT surface (same as it was observed for Pt-CeO_2 on MWCNTs in previous section). Unlike the CeO_2 (10 nm), the thicker CeO_2 coating (30 nm) reveals much less porous structure with nonporous parts.

Chemical state and composition of the films were investigated by using X-ray photoelectron spectroscopy. The Ce 3d core level XPS spectra obtained for CeO_2 film deposited on MWCNT/Si for both samples are presented in Fig. 25. Ce 3d spectrum consists of three $3d_{5/2}$-$3d_{3/2}$ spin-orbit-split doublets characteristic of Ce^{4+} (CeO_2) states and two doublets of Ce^{3+} (Ce_2O_3). The Ce $3d_{5/2}4f^2$ peak is fitted by an asymmetric feature accordingly to [78]. The appearance of Ce^{3+} means that the deposition of CeO_2 on the MWCNTs leads to a partial reduction of cerium oxide. The Ce^{3+}/Ce^{4+} peak area ratio for CeO_2 (10 nm), is higher than for CeO_2 (30 nm), (see Table 1) indicating that more oxygen vacancies are present in a more porous structure. Ce^{4+}, in turn, is characteristic of the thicker films, i.e. less porous structure. It suggests that cerium oxide bulk is stoichiometric whilst Ce^{3+} can be associated with cerium oxide film surface. Comparing these results with those obtained in "Deposition angle influence" section, where CeO_2 was sputtered on Si(001) substrate and no evidence of reduced ceria was observed (see Fig. 14a, bottom spectrum) we can assume that carbon substrate exhibits a significant influence not only on morphology but on stoichiometry of sputtered CeO_2 thin films as well.

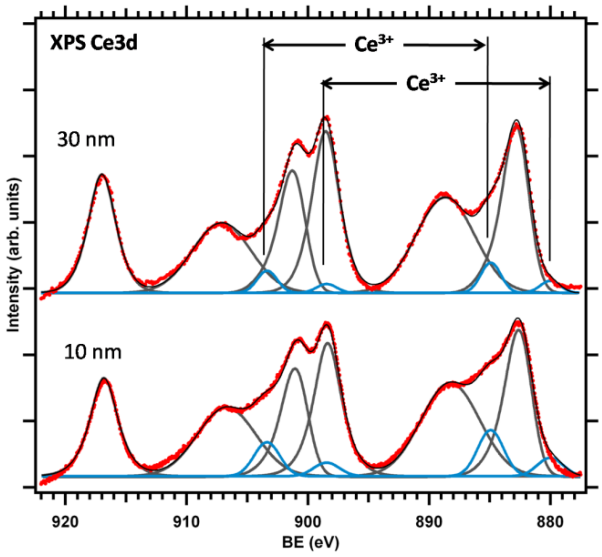

Fig. 25. *Ce 3d XPS spectra of the CeO_2 films with different thicknesses on MWCNTs: 10 nm and 30 nm.*

Next step of our work was devoted to doping of CeO_2 films by gold. The films of the same thickness as described above in this section were prepared by using

simultaneous magnetron sputtering of Au and CeO_2 from two magnetrons. Simultaneous magnetron sputtering of gold and cerium oxide on MWCNTs provides oxide layer continuously doped with Au atoms during the growth. Atomic concentration of Au related to ceria was about 1%. It was calculated from Ce 3d, and Au 4f peak areas by using the XPS atomic sensitivity factors.

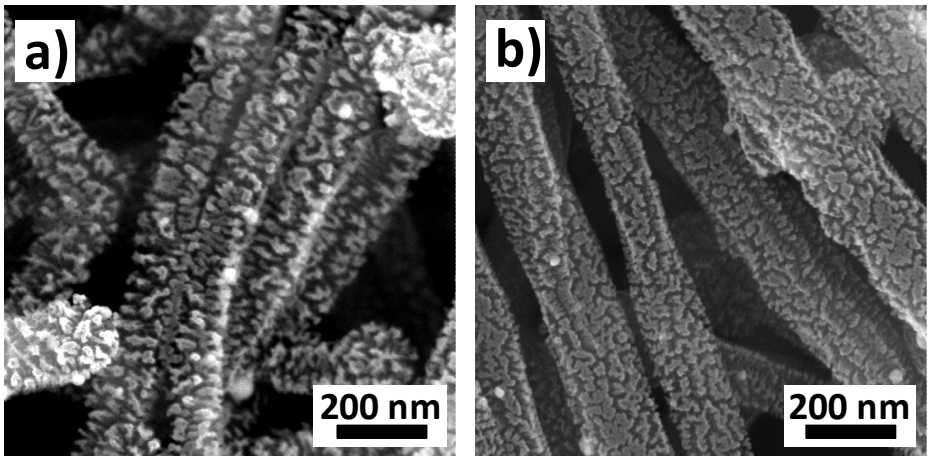

Fig. 26. *SEM image of Au-CeO_2 films with different thicknesses on MWCNTs: a) 10 nm; b) 30 nm.*

Fig. 26 shows SEM images of MWCNTs coated by two types of the Au-CeO_2 thin films: a) 10 nm; b) 30 nm. They reveal morphologies very similar to those obtained for undoped CeO_2 films (Fig. 24a, b). The Ce 3d spectra (Fig. 27a) also showed the same tendency for Au doped and undoped CeO_2 films, i.e. Ce^{3+}/Ce^{4+} peak area ratio decreased with increasing film thickness (see Fig. 27a and Table 1). Therefore one can conclude that embedded Au atoms do not make significant influence on ceria stoichiometry.

	CeO_2(10 nm)	CeO_2(30 nm)	Au-CeO_2(10 nm)	Au-CeO_2(30 nm)
Ce^{3+}/Ce^{4+}	0.12	0.06	0.11	0.05

Table 1. *Ce^{3+}/Ce^{4} peak area ratios for different CeO_2 and Au-CeO_2 thicknesses.*

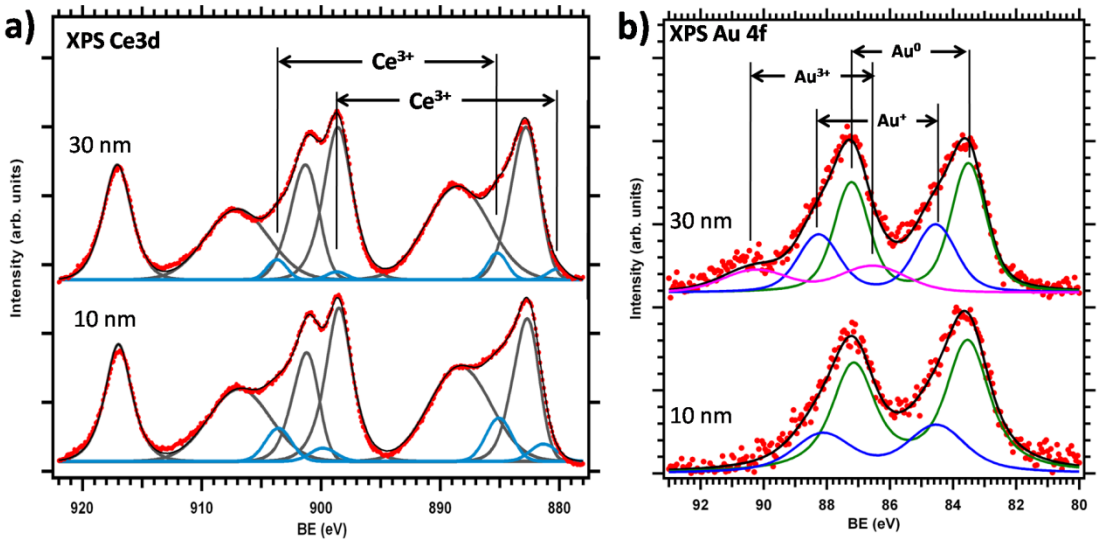

Fig. 27. *XPS a) Ce 3d and b) Au 4f spectra of the Au-CeO_2 films with different thicknesses on MWCNTs: 10 nm, 30 nm.*

The Au 4f XPS spectra obtained from the Au-doped ceria films with different thickness deposited on MWCNTs are plotted in Fig. 27b. In the case of Au-CeO_2 (10 nm) (bottom spectrum), the Au 4f spectra are composed of two doublets at binding energies 83.5/87.3 eV and 84.7/88.3 eV, respectively. The first doublet corresponds to metallic Au^0 while the second state can be associated with oxidized Au^+ species [79, 80]. In case of thicker films (upper spectrum) new doublet appears in addition to Au^0 and Au^+ at energies of 86.8 and 90.4 eV which can be attributed to the Au^{3+} species [80, 81]. Absolute concentrations of Au^0, Au^+ and Au^{3+} for different Au-CeO_2 thicknesses are shown in Table 2.

	Au-CeO_2(10 nm)	Au-CeO_2(30 nm)
Au^0	0.68	0.53
Au^+	0.32	0.29
Au^{3+}	0	0.18

Table 2. *Au^0, Au^+ and Au^{3+} absolute concentrations for different Au-CeO_2 thicknesses.*

We can conclude that low concentration of embedded Au atoms does not make significant influence on morphology of thin films and ceria stoichiometry but in turn, ceria stoichiometry makes influences on gold oxidation states [82]. It leads to the formation of a relatively high concentration of oxidized gold (50%). According to these results for further investigation of the catalyst films growth we will use the undoped ceria films.

By comparing the XPS spectra we can also assume that chemical composition of the catalyst changes with increasing film thickness in following way: 1) decrease of Ce^{3+} and increase of Ce^{4+} concentrations; 2) decrease of Au^{+} intensity and appearing of Au^{3+} states. Therefore, it seems reasonable to investigate the influence of film thickness on the morphology and stoichiometry of the films prepared by magnetron sputtering.

3.1.5. Film thickness influence

Thickness of deposited catalysts is another important parameter, influencing its activity [83]. It affects the cost of catalysis (through the catalyst loading) and can have a crucial impact on the film structure and morphology.

As already mentioned above, the morphology and stoichiometry of catalyst films depend on the film thickness (see “Doping by gold” subsection). In order to investigate this phenomenon more in detail, CeO_2 films with different thicknesses were deposited on graphite foil by simply controlling the deposition time. This experiment will allow us to monitor the morphology changes from the early stage of the film growth. Deposition was carried out using magnetron sputtering of CeO_2 in an Ar atmosphere at 2.7 Pa working pressure. We should also mention that the deposition rate in this case was estimated to be around 1 nm/min.

In order to follow the effect of film thickness influence on the morphology of deposited CeO_2 films, all samples were studied using high resolution SEM. Morphology evolution of CeO_2 thin films during sputter deposition studied by SEM is plotted on Fig. 28 (the width of each stripe is 200 nm).

We can observe dramatical change in the surface morphology after increasing the deposition time from 30 sec to 30 min. These images show that the roughness

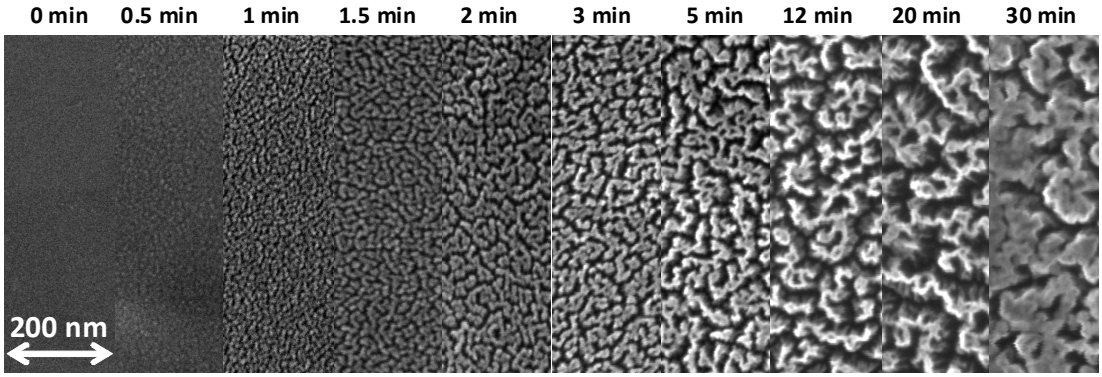

Fig. 28. *Morphology evolution of CeO_2 sputtered on C-foil for different deposition time studied by SEM.*

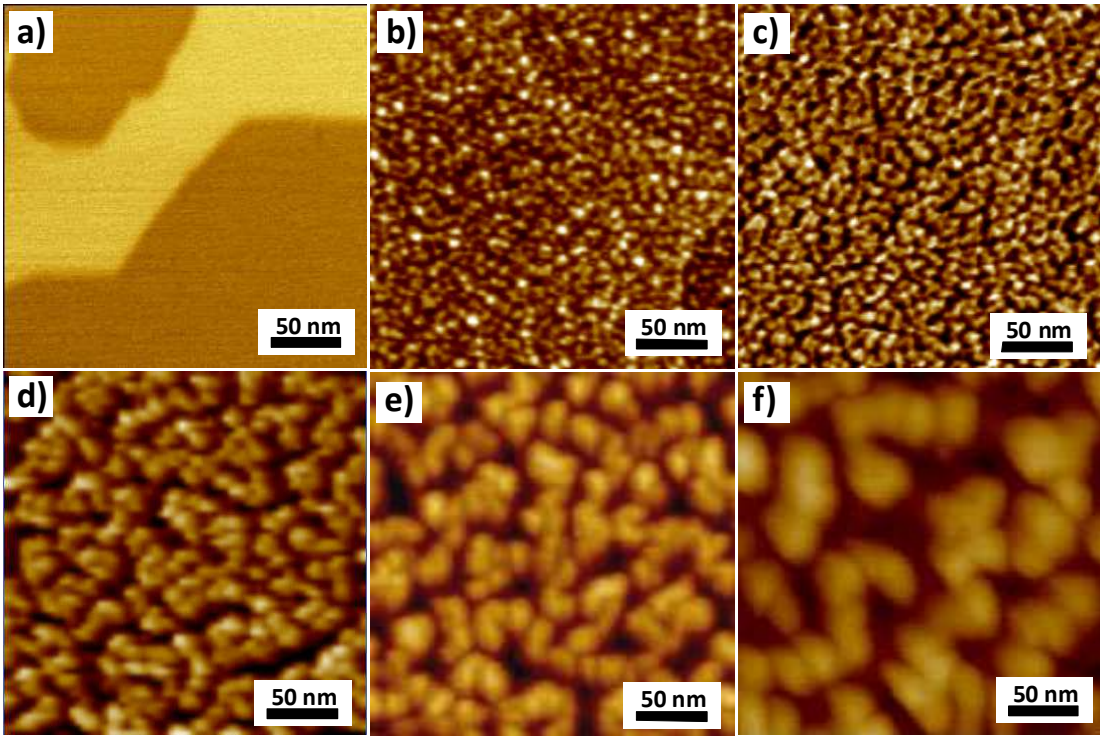

Fig. 29. *Morphology evolution of CeO_2 deposited on graphite foil for different deposition time studied by AFM: a) 0 min (fresh graphite foil); b) 30 sec; c) 1 min; d) 3 min; e) 5 min; d) 12 min.*

tends to gradually increase with increasing film thickness unless the film is thick enough and eventually covers porous structure forming denser films.

As the resolution of SEM does not allow us to observe small structures of thin films at the early stages of the growth, the AFM analyses were additionally undertaken for samples from 30 sec to 12 min deposition time. Fig. 29 shows the morphological changes in CeO_2 thin films during the sputter deposition studied by AFM. Table 3 shows the R_a roughness parameters calculated from represented AFM images using AFM software.

Deposition time	30 sec	1 min	3 min	5 min	12 min
R_a	0.5 nm	1 nm	2.5 nm	3.2 nm	6.3 nm

Table 3. *R_a values obtained for CeO_2 films with different thicknesses deposited on graphite foil.*

Fig. 29a shows atomically flat surface of fresh graphite foil. At the beginning of the growth (30 sec of deposition) we observed the formation of slightly rough surface, which consists of small grains (Fig. 29b). With increasing of the deposition time the grains are increasing in size and coalescence forming fractal like structure and, at the same time, we observe larger voids in between the grains (Fig. 29c, d). At 12 min of deposition time a significant increase in surface morphology was observed. We can distinguish columnar structure of the films and it seems that the columns originate from individual nucleus formed at the beginning of the growth (see Fig. 28). Further increase of the deposition time (30 min of deposition) leads to further morphological changes: cerium oxide pillars bind together and reveal much less porous structure (see Fig. 28). We can conclude that at the carbon-catalyst interface the sputtered CeO_2 film forms a nanorod structure. In the case of thicker layers the effect of the interface decreases and less porous films are grown. This actually explains appearance of the partial porosity on MWCNTs on Fig. 15b (See “Deposition angle influence” section). The thickness of deposited films changes across the single MWCNT: it is thicker on top of the MWCNT and thinner at its

edges. However, the assumption about the deposition angle influence in case of MWCNTs still remains valid.

We also carried out the XPS study for 1, 5 and 20 min of deposition samples. The Ce 3d core level XPS spectra of the CeO_2 films with different film thicknesses deposited on the flat graphite foil substrate are presented in Fig. 30.

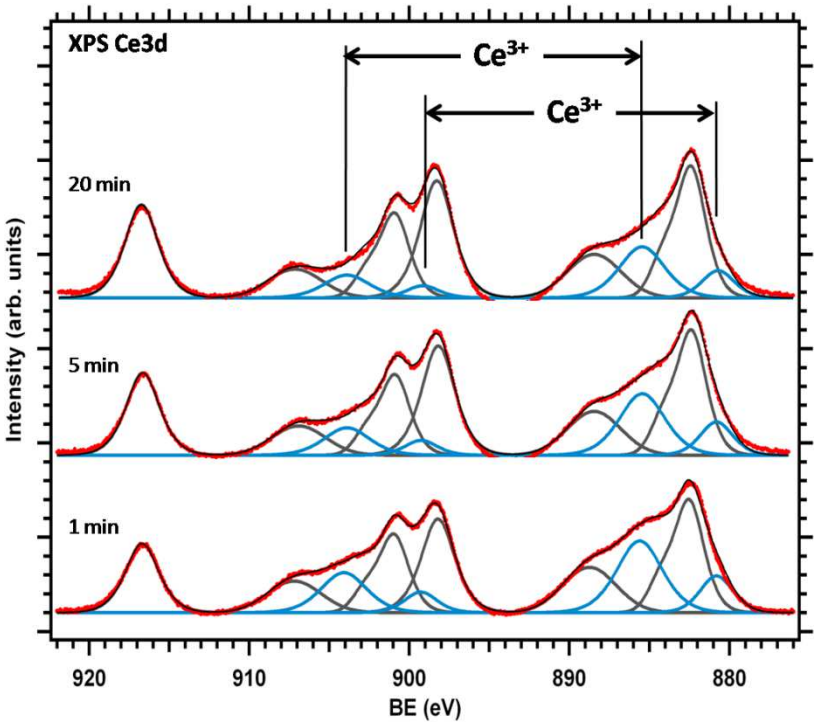

Fig. 30. *XPS Ce 3d spectra obtained for CeO_2 deposited on graphite foil for 1, 5 and 20 min.*

We can observe the Ce^{3+} state intensity in all cases, which confirms that the deposition of CeO_2 on graphite foil leads to a partial reduction of cerium oxide [26]. In the case of the films deposited for 20 min the relative concentration of Ce^{3+} states is less pronounced (upper spectrum) than in the case of the films deposited for 1 min (bottom spectrum). Calculated Ce^{3+}/Ce^{4+} peak area ratios for all three samples are shown in the Table 4. These results indicate that more oxygen vacancies are present in thinner films i.e. closer to the carbon-ceria interface. Ce^{4+}, in turn, characterizes thicker films.

Comparing these results with previous work (see “Deposition angle influence” section), where CeO_2 was sputtered perpendicularly on Si(001) substrate

(see Fig. 14a), we can assume that carbon-cerium oxide interaction exhibits a significant influence on stoichiometry of sputtered CeO_2 thin films resulting to the formation of reduced ceria layers as it was in case of GLAD conditions (see Fig. 14a).

Deposition time	1 min	5 min	20 min
Ce^{3+}/Ce^{4+}	0.43	0.33	0.25

Table 4. *Ce^{3+}/Ce^{4+} ratios for CeO_2 deposited on graphite foil for 1, 5 and 20 min.*

This experiment proves that morphology and stoichiometry of ceria based films prepared by magnetron sputtering strongly depends on the film thickness. Hence, we are able to tune the morphology, i.e. the active surface area, and stoichiometry of the ceria based catalyst by simply changing the deposition time.

To understand the mechanism which takes place at the interface between deposited CeO_2 films and carbon substrate, the ceria films deposited onto graphite foil were dissolved out in 50 % sulfuric acid solution afterwards [84]. The acid treatment was carried out at 50 °C for 24 hours. In Fig. 31 we present SEM and AFM images of 5 nm thick CeO_2 films on graphite foil before (Fig. 31a, c) and after (Fig. 31b, d) the H_2SO_4 treatment. XPS spectra (not shown herein) showed no evidence of ceria after H_2SO_4 treatment. As XPS is well known as surface technique, EDS was applied in addition to XPS. EDS spectra also contained no ceria peaks indicated that ceria was truly vanished. According to microscopy study it is evident that the carbon surface, after the ceria film has been removed, revealed very similar surface morphology to that of the CeO_2 coating structure. R_a calculated from presented AFM images were 2.7 nm and 2.1 nm respectively. It seems that only the top parts of the vertical structures have been removed by the acid treatment. As we observed no evidence of ceria on the acid treated sample, these top parts of vertical structures probably were the cerium oxide films.

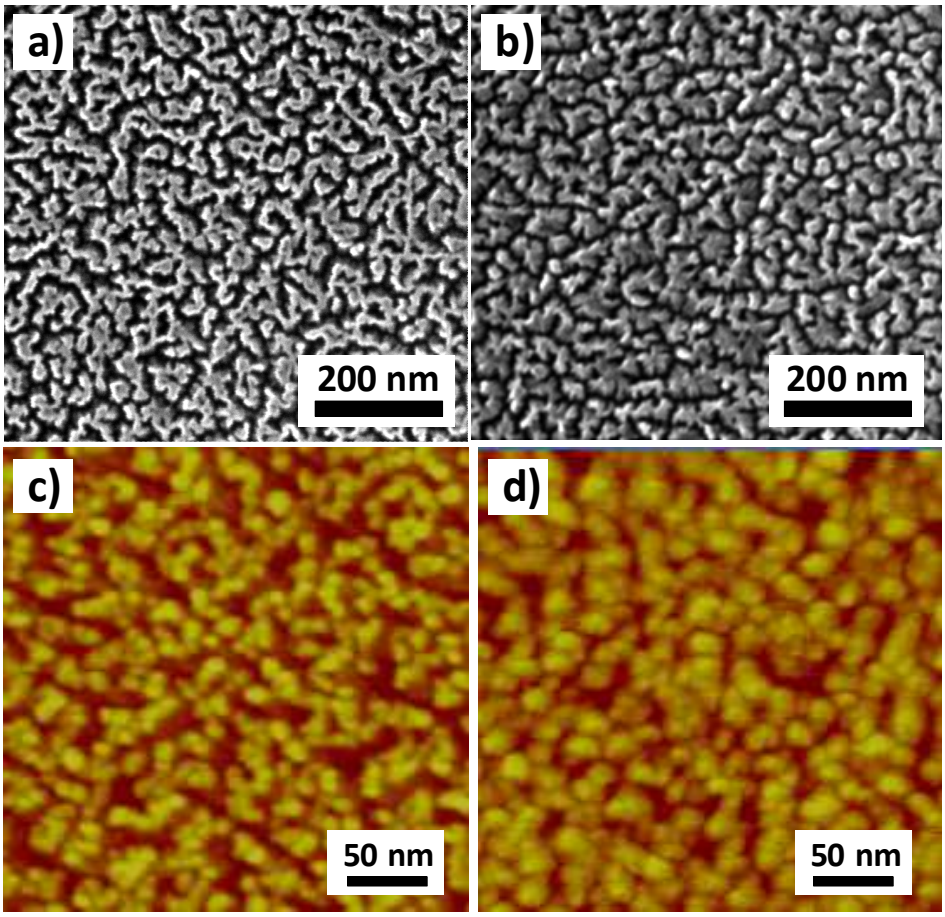

Fig. 31. *SEM images of CeO_2(5 nm) on C-foil: a) before H_2SO_4 treatment; b) after H_2SO_4 treatment, and AFM images of CeO_2(5 nm) on C-foil: c) before H_2SO_4 treatment; d) after H_2SO_4 treatment.*

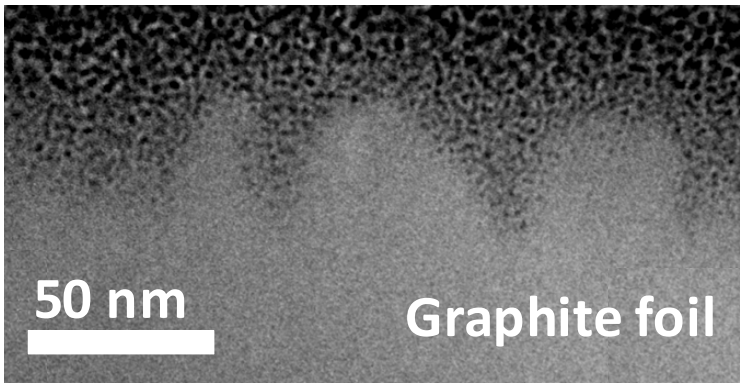

Fig. 32. *Cross-section TEM image of CeO_2 (5 nm) on C-foil after H_2SO_4 treatment prepared by means of FIB.*

This experiment shows that the rough structure formed by the deposition of CeO_2 on the carbon substrate using magnetron sputtering is determined by the carbon surface structure created during the films growth. Hence, the cerium oxide is just copying the substrate structure during the deposition.

In addition, for the acid treated sample we provided transmission electron microscopy (TEM) imaging of a lamella cut out perpendicularly to the interface by using a focused ion beam (FIB) technique. It confirms our suggestion about the rough carbon structure formation during the CeO_2 sputtering on graphite foil. We can clearly distinguish this structure in Fig. 32 (lighter part of image) in contrast with a platinum film (dark part of image), which we are usually using as a protection during the FIB lamella cutting. We should also note that TEM confirmed cerium oxide vanishing after acid treatment.

3.1.6. Different deposition techniques

In order to find out if the growth of such porous films is a special feature of carbon substrate and/or deposition technique we prepared 1 nm thick CeO_2 films on graphite foil using two different deposition techniques: electron beam physical vapor deposition (PVD) and magnetron sputtering. In case of the PVD, CeO_2 films were grown by evaporation of Ce from a molybdenum crucible heated by electron bombardment in 5×10^{-5} Pa oxygen atmosphere. 1 nm thickness was chosen because it takes a very long time to prepare thicker film using PVD technique. Magnetron sputtered CeO_2 films were prepared using the same condition as described above in this work. Selected SEM images of those two samples are demonstrated in Fig. 33.

Electron microscopy investigation clearly illustrates that only magnetron sputtering deposition leads to the formation of rough surface structure of CeO_2 (Fig. 33b), while the sample prepared by electron beam PVD method reveals a relatively flat morphology (Fig. 33a). This clearly shows that combination of use of carbon substrate and of the deposition technique influence is responsible for unique growth of the cerium oxide thin films.

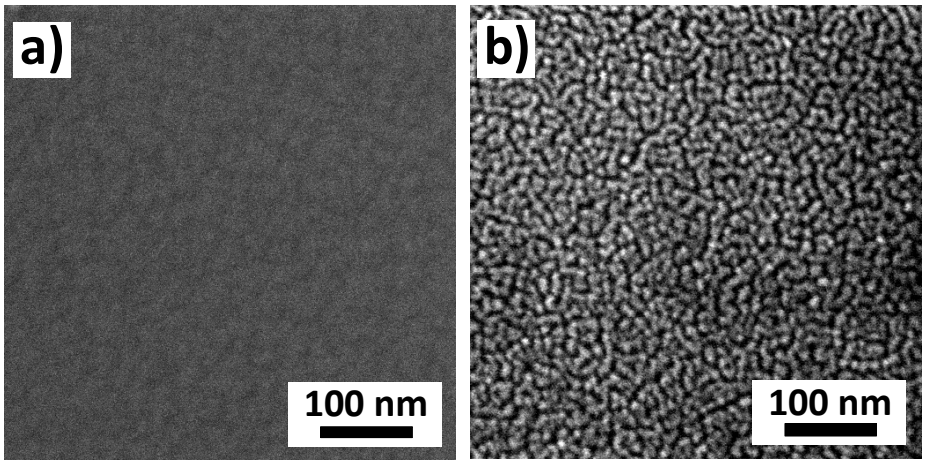

***Fig. 33**. 1 nm thick CeO_2 on graphite foil prepared by: a) electron beam PVD; b) magnetron sputtering deposition.*

According to these results, the key to understanding why the ceria films grow on the carbon substrates in such way lies in some particular features of magnetron sputtering. The main difference between PVD and magnetron sputtering is that the latter involves plasma in the deposition process. Hence, further work was provided to evaluate the impact of plasma on carbon surface.

3.1.7. Oxygen plasma etching

It has been shown in literature that the morphology of carbon materials surface can be modified by oxygen plasma [85-88], which is always present during magnetron sputtering of cerium oxide.

In order to investigate the oxygen plasma interaction with the carbon substrates we started by exposing the glassy carbon (GC) substrates to oxygen plasma for different periods of time: 20 and 40 min.

Oxygen plasma etching of GC was carried out in a MED 020 BalTec Modular High Vacuum Coating System. The etching device consisted of a ring-shaped driven electrode, placed 2 cm above the grounded substrate holder. The etching was carried out in pure oxygen (purity 99.999%) with total gas pressure of 20 Pa. The discharge current was set to 10 mA. The discharge voltage was automatically adjusted by the MED 020 system to 650 V.

A variation of surface morphology of GC surface in dependence on the oxygen plasma treatment time was investigated by high resolution SEM. In Fig. 34 we show selected SEM images representing GC substrate: untreated and treated by oxygen plasma for 20 and 40 min respectively. From these images it is evident that morphology of glassy carbon strongly depended on the oxygen plasma exposure time. The 40-min of treatment led to the formation of nanostructured surface consisting of well separated vertical nanostructures oriented perpendicularly to the substrate surface whilst the 20 min of treatment resulted in a finer dispersion of the surface nanostructures.

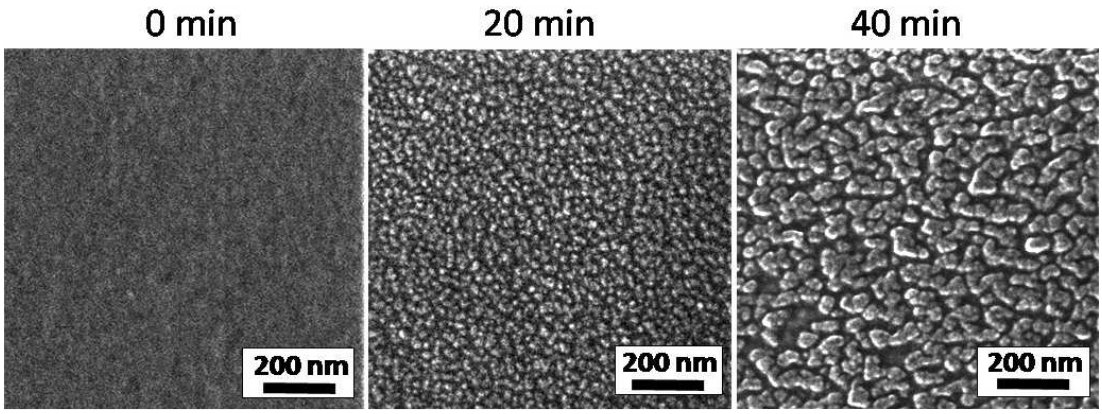

Fig 34. *SEM images of untreated and treated for 20 and 40 min GC surface.*

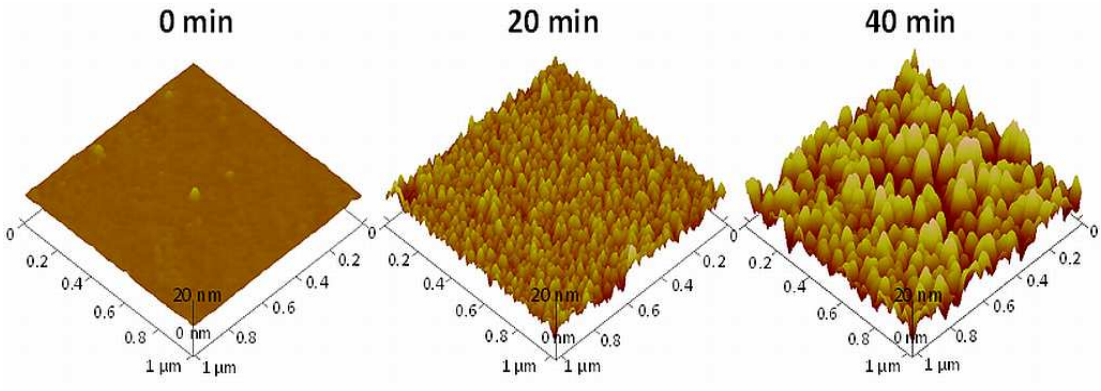

Fig. 35. *AFM 3D images of 1×1 µm GC surface: nontreated and treated for 20 and 40 min.*

In order to obtain more information about the surface roughness, in addition to the SEM characterization, AFM observations were performed. Morphology evolution during plasma modification of GC substrates studied by AFM is plotted on Fig. 35. AFM imaging confirms the morphology of etched GC and it gives additional information regarding the surface roughness. Morphology of plasma modified GC surface has been analyzed in terms of a surface roughness (R_a). The R_a values determined from 1×1 μm AFM scan area for each sample are shown in Table 5. It clearly shows that the increase of the plasma treatment time is accompanied by the increase in the surface roughness.

Treatment time	0 min	20 min	40 min
R_a	0.2 nm	2 nm	4.8 nm

Table 5. *R_a values obtained for nontreated and treated for 20 and 40 min GC surface.*

For further investigation of the oxygen plasma etching of GC we partially masked a part of fresh GC surfaces by a droplet of varnish and placed the substrates into oxygen plasma for the same period of time as described above in this section, and additionally we put one more sample for 10 min of treatment. After removing the varnish drops we observed formation of a steps between non-etched (masked by varnish) and etched GC surfaces (Fig. 36a). In Fig. 36b, a SEM image and an AFM profile of the step obtained for the 20-min treated sample are shown. We can clearly distinguish the treated and untreated parts of the substrate and determine the amount of material etched away by simple measurement of the step height from the AFM profile across the edge. The step height values obtained from AFM profiles of all samples are shown in Table 6. This means that during the oxygen plasma etching of the GC surface two processes take part simultaneously: a removal of a part of the GC material and a surface nanostructuring.

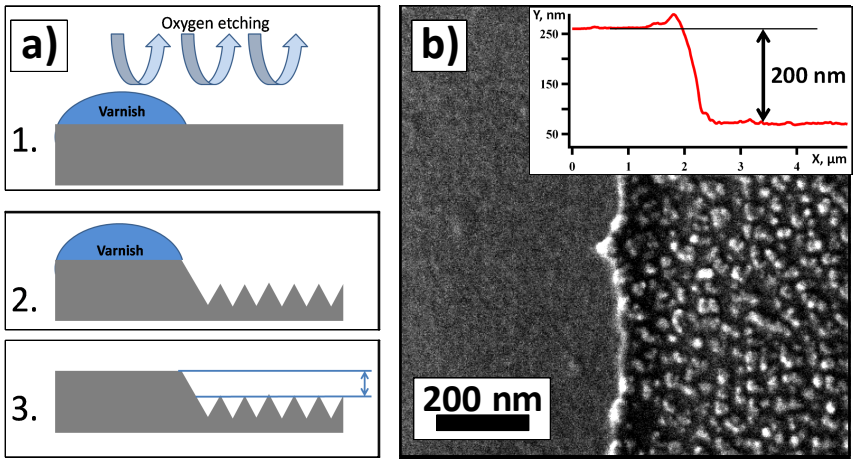

Fig. 36. *a) Schematic illustration of a step formation; b) SEM image and AFM profile of the edge obtained for the 20 min treated sample.*

Treatment time	0 min	10 min	20 min	40 min
Step height	-	60 nm	200 nm	320 nm

Table 6. *Step height values obtained for treated for 10, 20 and 40 min GC surface.*

Oxygen plasma etching technique allows us to prepare high surface area glassy carbon substrate and to tune the surface roughness and porosity by varying the treatment time. Such modified glassy carbon makes this material interesting as a catalyst support in the field of electrochemistry, particularly for cyclic voltammetry study of morphology-dependent thin film catalyst activity.

In the second part of the experiment we prepared CeO_2 films by magnetron sputtering of cerium oxide onto the GC substrate. The working pressure was 2.7 Pa and calculated deposition rate was about 1 nm/min. Although the deposition takes place in an Ar atmosphere, the working atmosphere contains oxygen sputtered off from the cerium oxide target. Therefore, one can expect that growth of oxide thin films on carbon substrate is accompanied by a simultaneous oxygen plasma etching of the carbon substrate surface.

Indeed, in the case of a 20 min of deposition time we observed a formation of a rough structure (Fig. 37) similar to the case of 20 min oxygen plasma etching of GC (see Fig. 34).

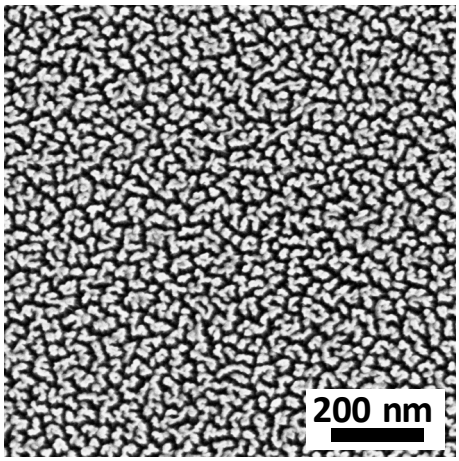

Fig. 37. *SEM image of CeO_2 films sputtered on GC substrate for 20 min.*

In order to continue investigations of carbon modification by oxygen plasma etching during oxide material deposition on carbon substrate, we looked at the roughness of the catalyst film/substrate interface using transmission electron microscopy imaging of a lamella cut out perpendicularly to the interface using a FIB technique.

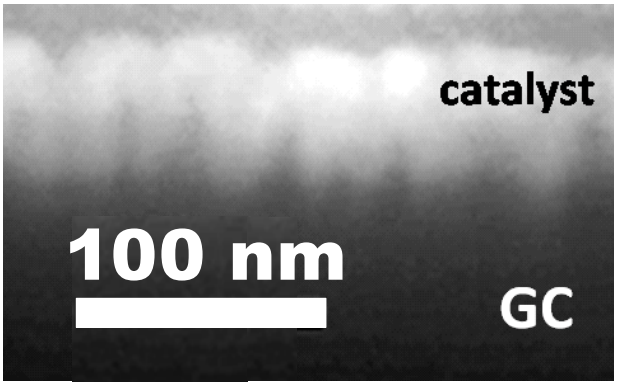

Fig. 38. *TEM image of CeO_2/GC interface prepared by means of FIB.*

Fig. 38 provides clear evidence of simultaneous carbon etching during the deposition showing the formation of a rough interface with about 30 nm deep cavities etched in the GC surface coated by the 20 min deposition catalyst film. This well explains formation of the carbon rough structure after removing ceria by H_2SO_4 treatment. Therefore, we can conclude that the GC substrate is modified during the magnetron sputtering of CeO_2 in a way similar to the case of the oxygen plasma etching. Thus, the observed behavior of porous CeO_2 films growth can be explained by a simultaneous growth of the catalyst and etching of the GC substrate [89].

We are expecting that randomly distributed Ce-O islands are formed at the early stages of the growth and, simultaneously, the oxygen plasma is etching the GC substrate in the space between the islands. These islands serve as an etching mask and define the film morphology (see Fig. 39a). The sputtering rate in this case should be small enough to ensure sputtered particles migration at the surface and nucleus formation, which is necessary for keeping the CG surface partially uncovered for oxygen interaction with carbon. We suppose that during the growth the incoming particles will preferentially deposit on top of the nuclei due to higher accessibility of the upper parts of the 3D structures [90] and cerium oxide forms three dimensional catalyst structures (Fig. 39b). Cerium oxides pillars are growing while oxygen is still etching non covered graphite.

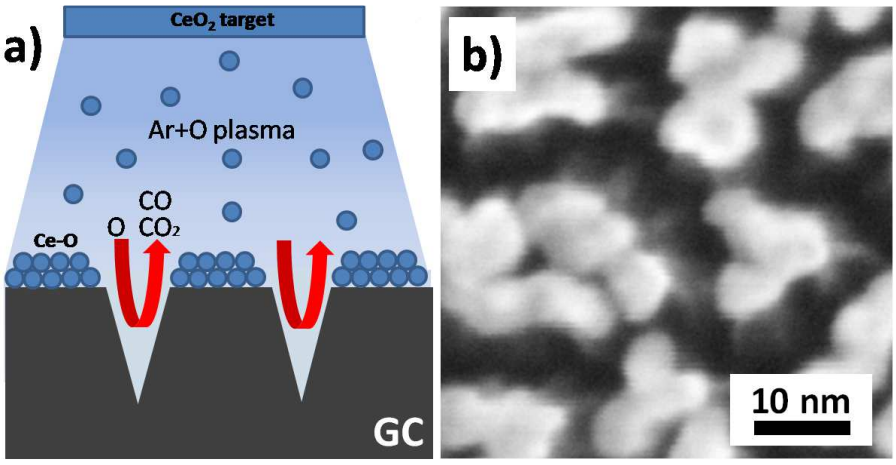

Fig. 39. *a) Model of simultaneous deposition and etching during magnetron sputtering deposition of CeO_2; b) high resolution SEM image of CeO_2 film on GC prepared by magnetron sputtering.*

Moreover, oxygen plasma etching of carbon is responsible for the formation of oxygen deficient cerium oxide at the film-substrate interface. It perfectly agrees with previous results (see “Film thickness influence” section) where we showed by using the photoelectron spectroscopy that the porous CeO_2 films deposited on graphite foil were partially reduced (see Fig. 30). The dependence of the Ce^{3+}/Ce^{4+} ratios on the film thickness pointed out that the films were more reduced closer to the interface.

Generally, oxygen plasma etching involves reaction of oxygen species in the plasma with the substrate. Plasma is formed by a partially ionized gas consisting of equal numbers of positive and negative charged species and different number of neutral species. According to the literature, free oxygen atoms (O), formed by dissociation and ionization in plasma between electrons and oxygen molecules, have been shown to be the dominant reactive species involved in oxygen plasma etching process [91, 92]. In order to prove or disprove that in case of magnetron sputtering of cerium oxide, we modified our deposition system.

We added the metallic grid inside the deposition chamber which separated carbon sample from the magnetron plasma, as shown in Fig. 40. On the grid we applied either positive bias (to reflect positively charged species) or negative bias (to reflect negatively charged species).

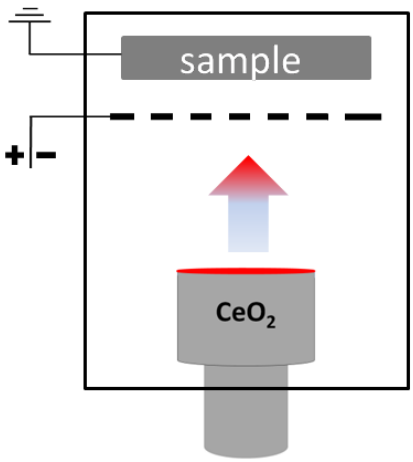

Fig. 40. *Schematic illustration of modernized magnetron sputtering equipment.*

The experiment gave us clear evidence that there is no influence of positively and negatively charged particles on the morphology of ceria films. According to the

SEM investigation (not shown herein) the morphology of ceria films remained porous even when we putted positive or negative bias on the grid. This means that only neutral particles, which are able to pass through the grid, are responsible for the carbon substrate etching.

In our case, the etching process is assigned to the chemical oxygen plasma etching, where the reactive oxygen atoms diffuse out of the plasma, adsorb onto the carbon substrate surface and react chemically with the carbon atoms forming volatile products (CO or CO_2) which are pumped away during the etching. This process has already been proven by monitoring CO_2 production using mass spectrometer during the etching process [93]. It also explains the fast removal of carbon from the sample, see Fig. 36b.

The above presented results demonstrated example of the catalyst-substrate interactions, which were enhanced by interaction of plasma species with substrates during ceria films growth. It resulted in influencing substantially physical and chemical properties of the catalyst films.

3.1.8. Deposition rate influence

It is likely that deposition rate should be small enough to ensure carbon etching by oxygen plasma during CeO_2 deposition and thus, to form porous catalyst structure. In order to estimate an influence of deposition rate on the morphology of thin films, we deposited CeO_2 films on graphite foil at different deposition rates. At the same time the film thicknesses were kept constant to exclude films thickness influence (see “Film thickness influence” section). To obtain different deposition rates and keep the film thickness constant, RF power as well as the deposition time had to be changed accordingly.

First, we checked how deposition rate depended on RF power. The deposition was carried out at constant value of pressure (2.7 Pa). Calibration was provided by ceria deposition on the varnish drop/Si substrate to evaluate the correct films thicknesses. In Table 7 we show the results of this experiment. We found that such RF power/deposition rate dependence is almost linear (Fig. 41).

Using this graph we can predict the deposition rate from the value of RF power applied on the ceria target. We should mention, however, that when we set 10 W of RF power we could not measure the film thickness (even after 1 hour of sputtering). Obviously, 10 W of RF power is not sufficient to sputter off ceria atoms and/or molecules from the CeO_2 target. On the other hand it is enough power to sputter off the oxygen atoms because the etched rough structure was still observed on graphite foil (not shown herein).

RF power, (W)	20	30	40	50	60	70	80	90	100
Deposition rate, (nm/min)	0.4	0.6	1	1.3	1.6	2	2.4	2.8	3.2

***Table 7**. Dependence of deposition rate of ceria films on RF power on CeO_2 target.*

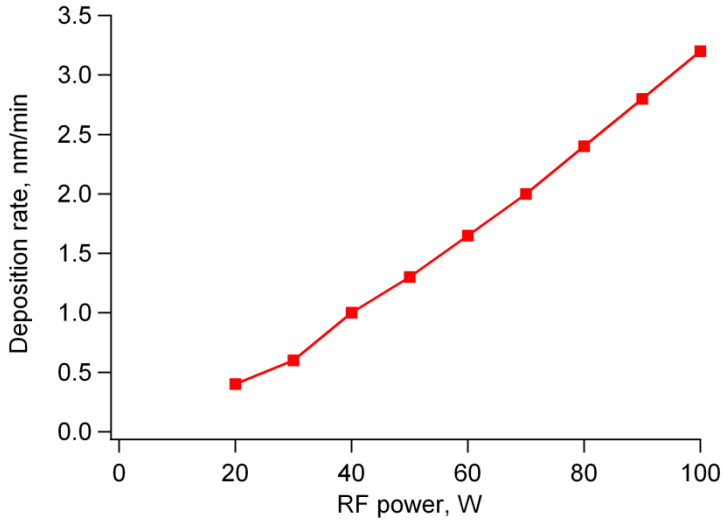

***Fig. 41.** Dependence of deposition rate of ceria films on RF power on CeO_2 target.*

For the experiment mentioned above, 0.3 nm/min, 1 nm/min and 3.2 nm/min deposition rates were chosen. The thickness of ceria films deposited on the graphite foil in all cases was about 10 nm. SEM observation of those three samples definitely proved our suggestions about the influence of the deposition rate on morphology of ceria films prepared by magnetron sputtering (Fig. 42). Indeed, the lower deposition

rates lead to the formation of rough structure (Fig. 42a). Contrary, higher deposition rates cause decreasing of the surface roughness (Fig. 42b). At 3.2 nm/min deposition rate porosity almost disappeared (Fig. 42c).

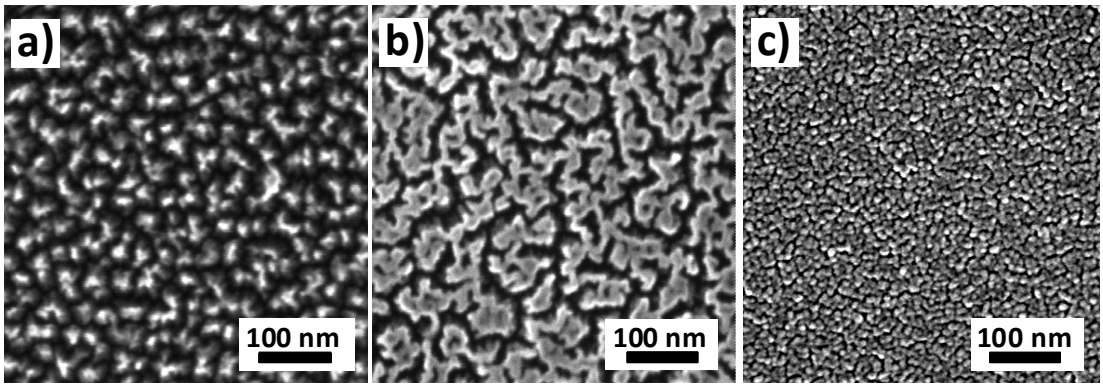

Fig. 42. *10 nm thick CeO_2 film on graphite foil prepared using: a) 0.2 nm/min; b) 1 nm/min; c) 3.2 nm/min deposition rates.*

Taking into account that the thickness of samples and deposition conditions were the same, we can state that the deposition rate is an important parameter, which significantly affects the morphology of the CeO_2 films prepared by magnetron sputtering.

These results are also in agreement with hypothesis, which we proposed to explain the formation of porous structure in the case of CeO_2 deposited on carbon substrates (see “Oxygen plasma etching” section). As we suggested, the growth of porous film on carbon substrates prepared by magnetron sputtering was caused by simultaneous deposit growth and oxygen plasma etching at the space between deposit nuclei. At low deposition rates sputtered particles migrate at the surface, i.e. they do not wet it, by forming ceria nucleus. There is lot of space for plasma etching between those nuclei. Contrary, at high deposition rates (generally above 3 nm/min) porosity of deposits disappears, apparently due to a rapid covering of the substrate by the deposited overlayer and preventing oxygen plasma etching of the carbon support. As a result, the films grow non-porous.

3.1.9. Two-step catalyst preparation

Using all results described above, we are now able to control preparation of a high-surface catalyst on carbon electrodes using two-step preparation: at the first stage carbon substrate is etched in oxygen plasma and, at the second stage, catalyst is deposited on top of the etched carbon surface with high deposition rate to avoid further etching during film deposition (see “Sputtering rate influence” section).

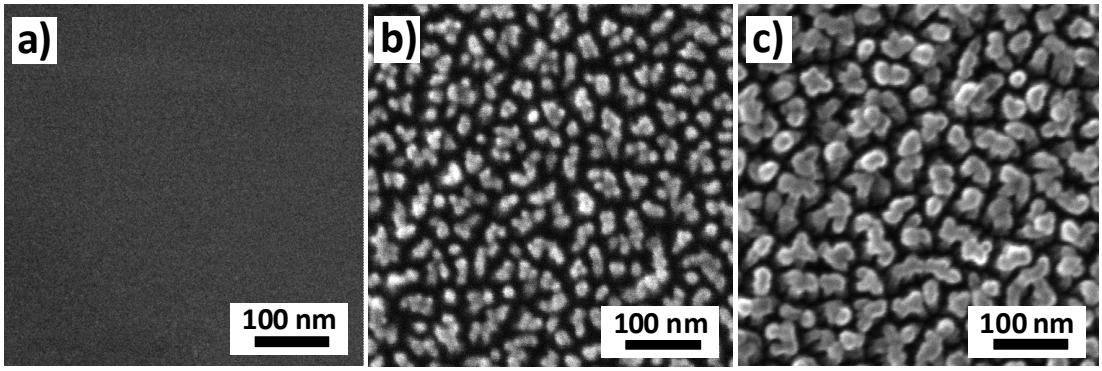

Fig. 43. *SEM images of: a) fresh carbon substrate; b) carbon substrate etched for 40 min; c) 5 nm thick Pt-CeO_2 deposited on top of carbon substrate etched for 40 min.*

Fig. 43 represents selected SEM images of: a) fresh carbon substrate, b) carbon substrate etched for 40 min, and c) 5 nm thick Pt-CeO_2 films deposited on top of etched for 40 min carbon substrate at 3.2 nm/min deposition rate. As a result, two step catalyst preparations allow us to prepare any type of high surface area catalyst film on carbon support minimizing the catalyst loading due to high specific area of carbon electrode.

3.1.10. Fuel cell test

As it was already mentioned in “Overview” part of present thesis, surface is vital in the field of catalysis and the carbon nanotubes can significantly increase the catalyst specific surface area. As we are showing in this work we are able to prepare highly porous Pt doped CeO_2 films on the carbon nanotubes which increases the

catalyst active surface area even more. Such nanoporous Pt-CeO_2/CNT composites should have a high catalytic activity when used as an anode in PEMFC.

In order to prove this suggestion, FC tests were performed using small fuel cell device. The membrane electrode assembly (MEA) components were similar to those typically used in polymer electrolyte membrane fuel cell. The pre-treatment of the Nafion membranes 0.125 mm thick (Alfa Aesar, Nafion NE-1035 perfluorosulfonic acid-PTFE copolymer) was performed by using a standard process of boiling in H_2O_2 solution, dilute H_2SO_4 and H_2O [94]. The pre-treated Nafion membrane was sandwiched by the catalyzed anode and cathode to form MEA of 1 cm^2. MEA was then sealed between graphite gas distributors. The cathode electrode was made by carbon-supported Pt powder (Alfa Aesar, Platinum, nominally 40% on carbon black) and deposited on the microporous GDL. Loading of Pt in the cathode catalyst layer was about 2 mg/cm^2. To evaluate cell performance pure humidificated hydrogen and air were used as fuel and oxidant under atmospheric pressure.

The CNTs were synthesized by chemical vapor deposition (CVD) on the GDL wafer using CH_4 as a carbon precursor, H_2/Ar as carrier gas and Pd nanoparticles as a catalyst precursor. Details of the preparation procedure can be seen in ref. [95]. Pt-doped ceria thin films were deposited on the CNTs by magnetron co-sputtering of CeO_2 and Pt. The catalyst thickness was estimated to be around 30 nm and deposition rate of about 1 nm/min.

High resolution SEM was performed for investigation of surface morphology of coated MWCNTs. SEM images of the anode catalysts deposited on the CNTs are presented in Fig. 44 at different magnifications. Fig. 44a shows pure GDL wafer. Fig. 44b shows dense CNTs forest, covering the GDL microfibers. Fig. 44c shows good dispersion of the CNTs. The average diameter of the CNTs was 25 nm. Fig. 44d shows details of one CNT covered by the catalyst layer. The catalyst film surface reveals rough structure similar to that we have seen above on the GC, HOPG, graphite foil and MWCNTs (see “Substrate influence” section). Dense “fur” of fine, long and well separated CNTs grown directly on the GDL is an excellent support of the catalyst thin films. The CNTs directly grown on GDL were chosen for the fuel cell test because they have good electrical contact between the grown CNTs and the GDL which is essential in the field of PEMFCs.

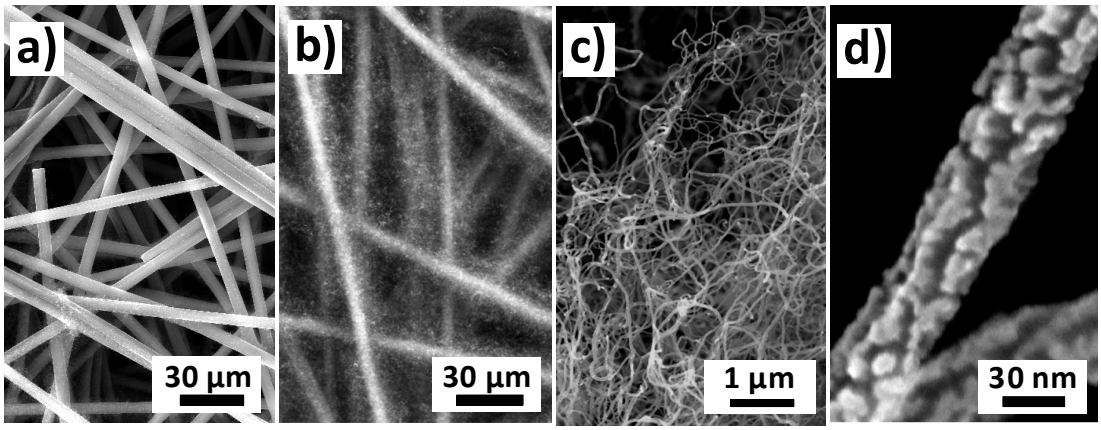

Fig. 44. *SEM images of: a) fresh GDL; b-d) CNTs grown on the GDL and coated by 30 nm thick Pt-CeO_2 catalyst films at different magnifications.*

XPS was also undertaken to investigate chemical composition of anode catalyst. As we have shown before, porous ceria layers exhibit reduced cerium oxide (see "Film thickness influence" section). This case is not an exception and we observed partially reduced cerium in the Ce 3d core level XPS spectrum shown in Fig. 45a.

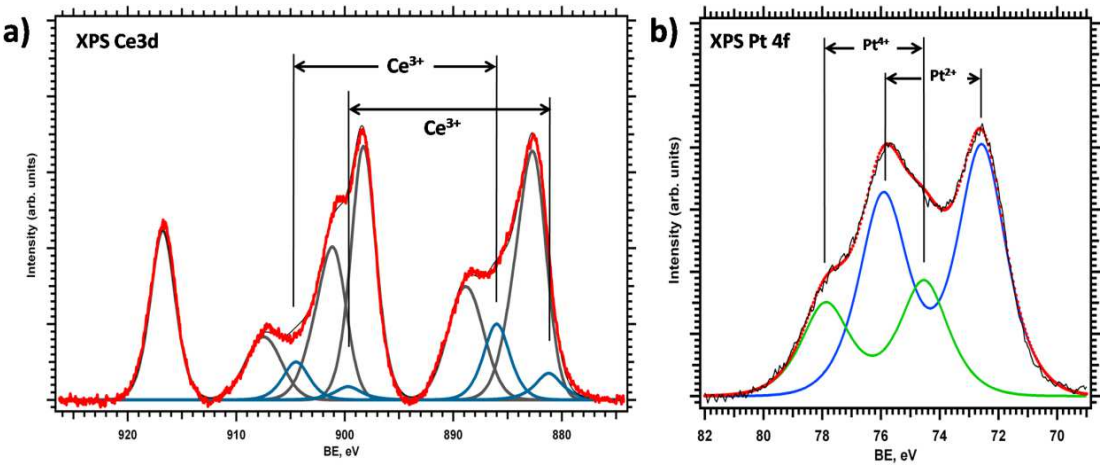

Fig. 45. *a) XPS Ce 3d and b) Pt 4f spectra of Pt-CeO_2 thin films sputtered on CNTs directly grown on GDL.*

The Pt 4f XPS spectrum is plotted on Fig. 45b. It consists only of platinum cations. The spectrum exhibits Pt $4f^{7/2}$-$4f^{5/2}$ doublet at 74.5-77.9 eV corresponding to

Pt^{4+} [74] and second doublet at energies of 72.6 and 75.9 eV, which can be attributed to the Pt^{2+} species [43]. Pt^{2+}/Pt^{4+} ratio was estimated to be 2.17.

Pt concentration in CeO_2 of about 4 at% was determined using the XPS data. It should be noted, however, that the Pt concentration determined in this way corresponded to an average Pt concentration in the surface layer probed by XPS which is approximately 2 nm thick, and could slightly differ from that of the film bulk. The Pt content in the anode catalyst was estimated to be about 2 μg/cm^2 of MEA.

Porous structures exhibit higher relative content of surface oxygen vacancies (see "Oxygen plasma etching" section) and neighboring Ce^{3+} cations (see Fig. 30). Those cations could strongly interact with Pt atoms. Therefore, high Pt^{2+}/Pt^{4+} intensity ratio observed for the CNTs can be explained by the formation of Pt^{2+} rich Pt-O-Ce clusters at the surface of reduced cerium oxide inside the porous structure of the catalyst film.

The performance of the PEMFC with the Pt-CeO_2 film coated CNT/GDL used as anode was investigated at 70 °C. The FC test was prepared by using commercial Pt/C cathode catalysts. The polarization V-I curves are shown in Fig. 46 together with the power density (PD) characteristics.

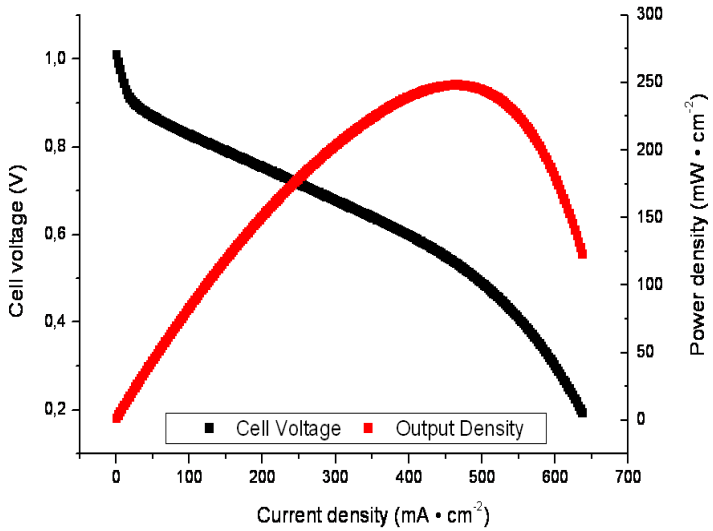

Fig. 46. *Polarization and power density versus current density using hydrogen/air flow of the fuel cell with Pt-CeO_2/CNT(CVD)/GDL anode at 70 °C.*

We can see that we obtained maximum power density PD_{max} = 248 mW/cm^2. This value corresponded to maximum specific power SP_{max}= 124 W/mg(Pt). The FC test confirmed our suggestion about excellent catalytic properties of the Pt-CeO_2 coated CNTs directly grown on GDL characteristic by high performance at very low platinum loading.

It is essential to compare obtained results with the reference ones. Commercial anode catalyst was tested on the same fuel cell equipment and at the same conditions. We used commercial PtRu anode and Pt/C cathode catalysts as the reference measurement. Loading of PtRu was about 4 mg/cm^2 and loading of Pt in the cathode catalyst layer was again about 2 mg/cm^2. The polarization V-I curves obtained at 70 °C for reference cell are shown in Fig. 47 together with the power density characteristic. We obtained PD_{max} = 438 mW/cm^2 which corresponds to the maximum specific power SP_{max} = 0.11 W/mg of precious metal (PtRu).

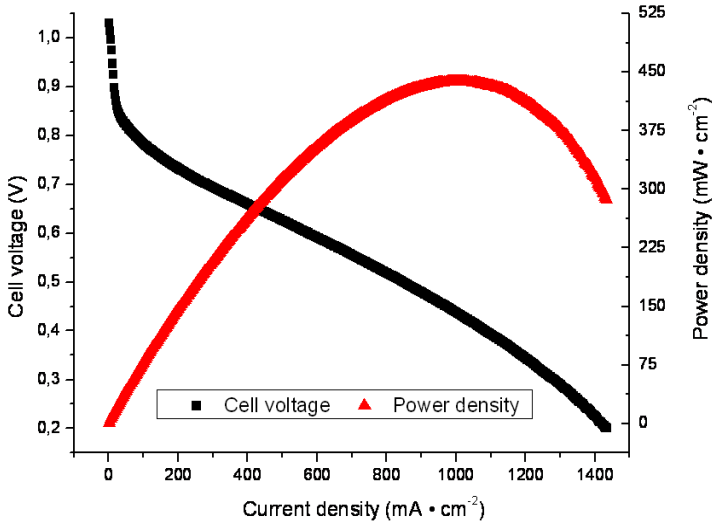

Fig. 47. *Polarization and PD versus current density using hydrogen/air flow of the fuel cell with reference PtRu anode at 70 °C.*

If we compare value of power density for commercial PtRu catalyst (PD_{max} = 450 mW/cm^2) with that obtained for magnetron co-sputtered Pt-ceria catalyst on the CNTs/GDL (PD_{max} = 248 mW/cm^2), we can see that PD value is almost twice larger in case of commercial catalyst but, on the other hand, if we compare power related to the amount of used platinum, i.e. specific power, we can

see an inverse effect. The maximum specific power for commercial catalyst is far lower (SP_{max} = 0.11 W/mg) comparing to Pt doped ceria catalyst deposited on the CNTs/GDL using magnetron sputtering (SP_{max} = 124 W/mg).

In summary, we have prepared and analyzed Pt-CeO_2 anode catalyst for PEMFCs. High surface area Pt-CeO_2 catalyst ensures high cost-efficiency of the PEMFCs. But, except of high surface area, an exclusive feature of the simultaneous magnetron sputtering of Pt and CeO_2 is the formation of fully cationic platinum within the oxide film lattice. Therefore, it seems reasonable to connect somehow high activity of the Pt-CeO_2 co-sputtered catalyst films with the formation of cationic platinum. The above described results demonstrate that co-sputtered Pt-CeO_2 catalyst films are promising alternative to more expensive commercial catalysts due to the low platinum loading and excellent catalytic performances.

3.2. Platinum oxide films prepared by magnetron sputtering

3.2.1. Introduction

As already mentioned in the "Overview", besides other applications, platinum and its oxides have been commonly used as a catalyst in fuel cells. Since platinum is (both in practical applications and model studies) often deposited on an oxide support, the oxygen can also be diffusively interchanged between the support and platinum [96]. In the previous chapter we showed that simultaneous magnetron sputtering of Pt and CeO_2 leads to the formation of fully oxidic platinum in Pt-CeO_2 catalyst films. Since the reactivity of metallic and oxidic form of platinum is generally different [97, 98], the performance of a Pt-based fuel cell may be sensitive to the oxidation state of platinum or the presence of oxygen within the catalyst volume. Therefore an investigation of platinum oxides catalysts is of a high interest.

Several types of platinum oxides have been reported so far. Pure crystalline compounds, including tetragonal PtO [99-101], cubic Pt_3O_4 [101, 102], Pt_5O_6 [102, 103], Pt_3O_8 [104], and PtO_2 [101] where the latter exists in two crystal modifications – α-PtO_2 [72, 101] with hexagonal structure and β-PtO_2 [102, 104, 105] with orthorhombic structure. Non-stoichiometric amorphous phases of platinum oxide (a-PtO_x) have also been prepared [106-109]. As a noble metal, platinum is relatively difficult to be bulk oxidized directly, the oxidation process can be, however, made electrochemically or by reactive sputtering, where either oxygen plasma induces formation of an oxide film on a pristine platinum surface [110] or platinum is sputtered away from a target in a mixture of oxygen and a noble gas (usually argon) using magnetron, and deposited onto a solid substrate; in this technique the resulting composition of oxide is determined by the deposition rate, the gas composition and pressure, and substrate temperature [72, 107, 111].

This chapter is devoted to the investigation of platinum oxides prepared by reactive magnetron sputtering as well as its interaction with hydrogen exposure using surface characterization techniques such as SEM, AFM and XPS.

3.2.2. Films preparation and characterization

Platinum oxide thin films supported on various substrates such as multi-wall carbon nanotubes, naturally oxidized Si(111) and graphite foil were prepared using reactive DC magnetron sputtering of platinum in pure oxygen atmosphere. Deposition was carried at room temperature and 2.7 Pa pressure of O_2. The applied power was 10 W yielding discharge voltage of about 280 V. The samples were placed 90 mm away from the 2 inch target. At these conditions the average deposition rate of 3 nm/min was achieved. According to ref. [100] platinum oxide was expected to grow as an amorphous PtO_x phase during reactive sputtering.

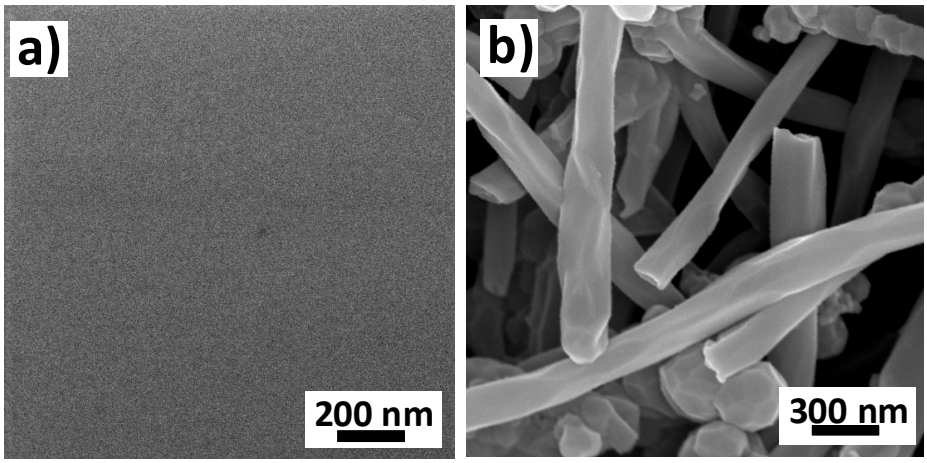

Fig. 48. *SEM images of: a) PtO_x(30 nm)/Si; b) PtO_x(30 nm)/MWCNTs.*

Platinum oxide (PtO_x) with thickness of 30 nm, deposited by magnetron sputtering on naturally oxidized Si(111) substrate, exhibits relatively flat and continuous morphology as it is demonstrated by SEM image in Fig. 48a. AFM investigation (not shown herein) permitted to determine the surface roughness of PtO_x films, which was around 0.1 nm. It should be noted, however, that morphology

of sputtered PtO_x films does not depend on the type of substrate as it was verified by comparing with MWCNTs (Fig. 48b) and graphite foil (not shown herein).

According to the literature, metal oxides can be reduced by hydrogen [112]. Platinum oxides (PtO and PtO_2) are known as not chemically stable and can be easily reduced to metallic state by hydrogen molecules forming water as a by-product [100]. The reduction process can be written as:

$$PtO_2 + 4H_2 \rightarrow Pt + 2H_2O$$

To understand what is going on with sputtered PtO_x thin films during/after interaction with hydrogen we exposed our sample (PtO_x (30 nm) on Si) to H_2 flow (20 sccm) at room temperature for 6 hours and checked the morphology again. PtO_x exhibited quite interesting behavior during the reduction process.

SEM analysis of PtO_x thin films deposited on the Si substrate after exposure to H_2 stream showed a massive disintegration of the originally smooth oxide layers of as-deposited PtO_x films. Fig. 49 illustrates the morphology of PtO_x films after interaction with H_2 at different magnifications. One can observe that interaction of PtO_x films with H_2 leads to the formation of cracked films structure with some islands partially piling off the Si substrate (Fig. 49a, b). At higher magnification we can distinguish significant roughening of the films surface (see Fig. 49c), thus increasing the specific surface area of the catalyst.

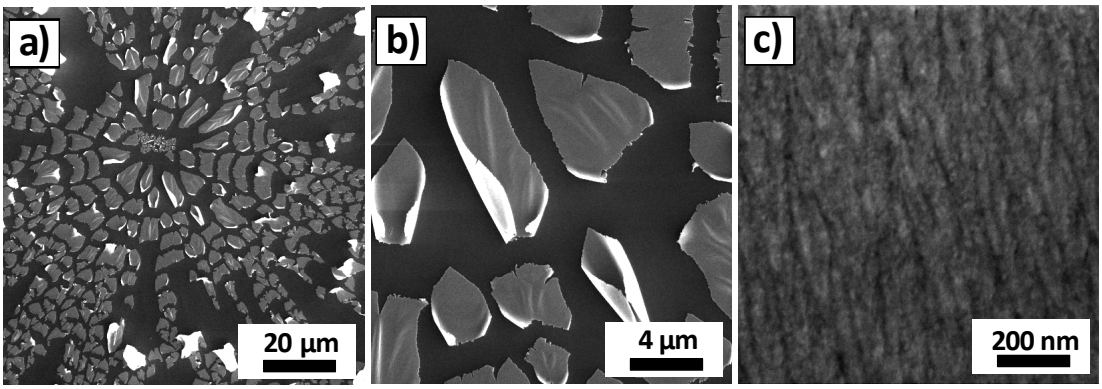

Fig. 49. *SEM images of PtO_x(30 nm)/Si(111) after exposure to H_2 stream at different magnifications.*

In addition to SEM we also carried out the AFM study of reduced PtO_x(30 nm)/Si(111). Fig. 50a and b illustrate AFM images of 30 nm thick PtO_x films after H_2 reduction at different magnifications. The AFM profile across the reduced PtO_x films is shown in Fig. 50c. The calculated surface roughness of the films from corresponding AFM images was about 1.7 nm which is much larger than in case of the PtO_x films before interaction with H_2 (0.1 nm).

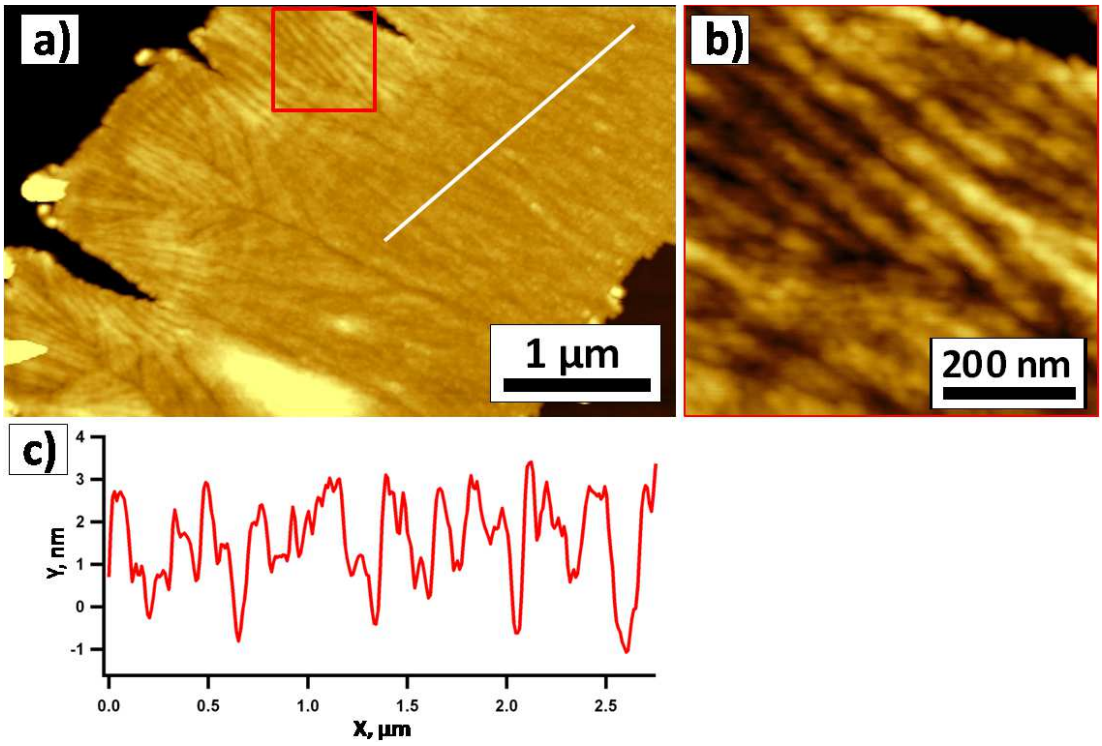

Fig. 50. *a, b) AFM images of PtO_x(30 nm)/Si(111)) after exposure to H_2 stream at different magnifications; c) AFM profile across the reduced PtO_x films.*

The chemical composition of the catalyst was also verified by XPS before and after interaction with H_2. Fig. 51 shows an example of analysis of the Pt 4f (Fig. 51a) and O 1s (Fig. 51b) spectra of PtO_x(30 nm)/Si(111) before and after exposure to H_2. We should mention that 30 nm thick films were thick enough to prevent any signal from the underlying silicon oxide substrate. The Pt 4f spectrum of as-prepared PtO_x/Si films (see Fig. 51a, the bottom spectrum) exhibits only a Pt $4f^{7/2}$-$4f^{5/2}$ doublet at 74.3-77.6 eV corresponding to Pt^{4+} (PtO_2) [113]. The upper spectrum on Fig. 51a represents Pt 4f spectrum of PtO_x/Si after interaction with H_2. It consists of

one doublet at 71.2-74.5 eV which is assigned to metallic platinum (Pt^0) [43]. Doublet, which indicates the presence of platinum oxide, (observed for as-deposited films) disappeared completely. As a result, the interaction of PtO_x with H_2 leads to complete reduction of the oxide films, which now consist only of the metallic platinum.

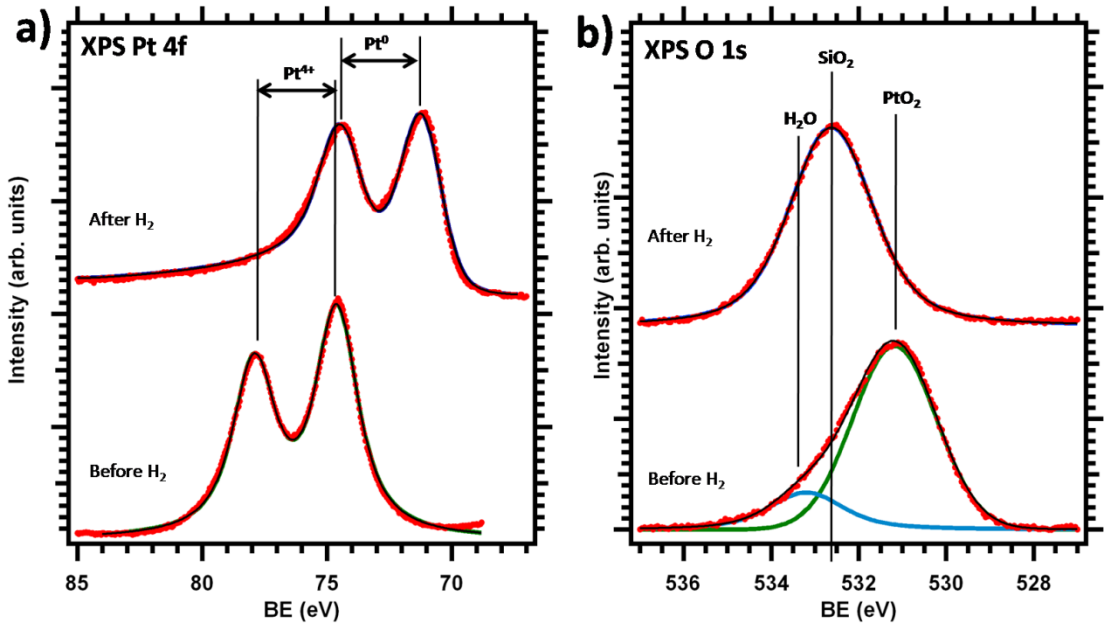

Fig. 51. *a) Pt 4f and b) O 1s XPS spectra of PtO_x(30 nm)/Si(111) before and after exposure to H_2.*

Corresponding O 1s spectra in Fig. 51b confirmed the above obtained results. In the case of as prepared films the O 1s spectrum consists of two peaks (bottom spectrum). The peak at 531.0 eV is matching the binding energy of lattice oxygen in stoichiometric PtO_2 [110], while the second peak at 533.3 eV can be attributed to residual water remaining at the surface in molecular form [114]. After H_2 interaction the PtO_2 peak disappears and a new peak appears at 532.7 eV which corresponds to SiO_2. This is in agreement with SEM study where we observed the Si surface after PtO_x films were cracked due to interaction with H_2.

The formation of cracked structure and increase of reduced films roughness, observed by SEM and AFM, can be explained by the platinum oxide reduction process. As the PtO_x films are reduced, it leads to the evolution of the mean molecular volume of the coating. As a result, the stress in the films occurs. The

platinum atoms try to minimize their surface energy, and the films begin to shrink (see Fig. 49c and Fig. 50b). As a result of the films shrinking we observe the formation of cracked structure (see Fig. 49a, b). It happens when the stress in the plane of the film exceeds the strength of the close packed network of substrate-bound particles [115].

For further investigation of sputtered platinum oxide reduction process we sputtered PtO_x films of different thickness: 10, 20 and 30 nm. We found that morphology of as-deposited oxide films does not much depend on the film thickness, revealing almost the same morphology as shown in the Fig. 48a in case of 10, 20 and 30 nm according to the SEM investigation (not shown herein). However, we monitored the dramatic changes in the morphology of reduced PtO_x films with different thicknesses. Fig. 52 illustrates the SEM images of PtO_x/Si(111): a) 10 nm, b) 20 nm, and c) 30 nm after H_2 reduction. One can observe that thinner films result in more dense cracked structure after the reduction.

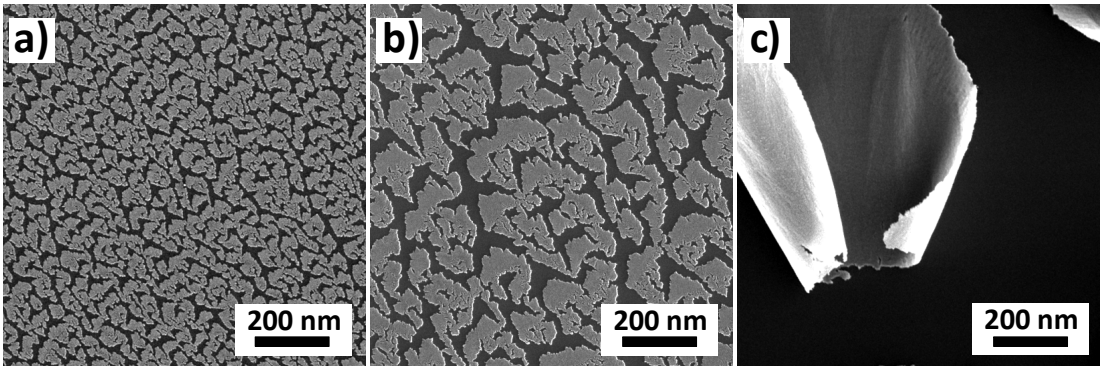

Fig. 52. *SEM images of PtO_x/Si(111) after H_2 reduction: a) 10 nm; b) 20 nm; c) 30 nm.*

All of these results describe a new method of preparation of platinum catalyst with very high surface area. Indeed, reducing of PtO_x by H_2 leads to the formation of a porous platinum structure as oxygen atoms are released from the PtO_x lattice due to the reduction process. We suppose that the Pt films prepared in such way might be very interesting as a catalyst for PEM fuel cell due to the high surface area and low platinum loading.

3.2.3. Fuel cell test

Fuel cell test was provided in order to confirm our suggestion. In this case we used commercial MWCNTs as an anode catalyst support. First, pristine MWCNTs were dispersed in N,N-dimethylformamide (DMF) at a concentration of 1 mg/30 mL using ultrasonic bath. The CNTs were then deposited onto a microporous gas diffusion layer (GDL) substrate by sedimentation from the suspension. This made possible to produces very uniform layers of dispersed MWCNTs. Typical time of precipitation was 24 h. We should mention, however, that dispersion in DMF gave the best results comparing our tests of HNO_3, water and ethanol. After this, PtO_x films with a thickness of 30 nm were deposited onto MWCNTs/GDL.

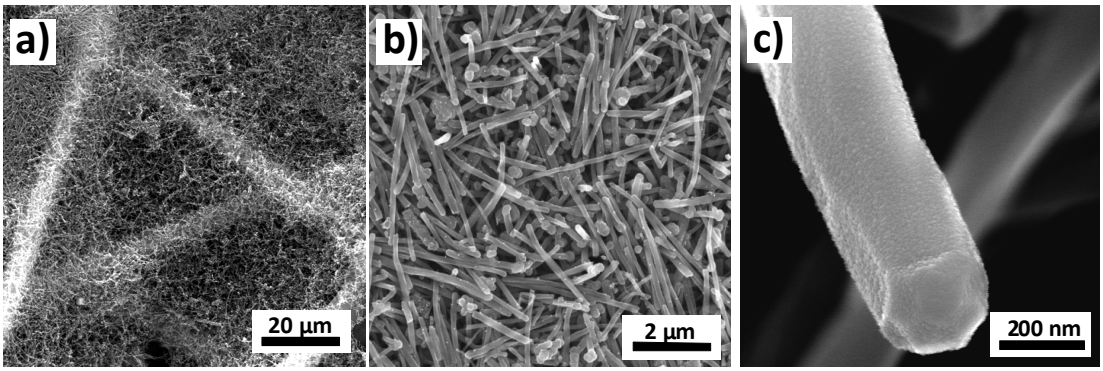

Fig. 53. *SEM images of: a) and b) dispersed MWCNTs on the GDL at different magnifications; c) detailed image of MWCNT/GDL coated by PtO_x films.*

High resolution SEM was used for investigation of the surface morphology of coated MWCNTs. Fig. 53a and b clearly show the uniform character of well spread MWCNTs overlaying the GDL microfibers which is suitable for preparation of large active surface catalyst. Outer diameter of the bare nanotubes, determined from the SEM images (not shown), reveals average value of around 100 nm. Length ranged from 5 to 10 µm. The MWCNTs reposed mostly in the position parallel to the GDL substrate and to the sputtering target as well. Fig. 53c shows a detail of MWCNT coated by the PtO_x films. At the next step, PtO_x films deposited on MWCNTs/GDL were reduced in H_2 flow to form porous Pt thin films.

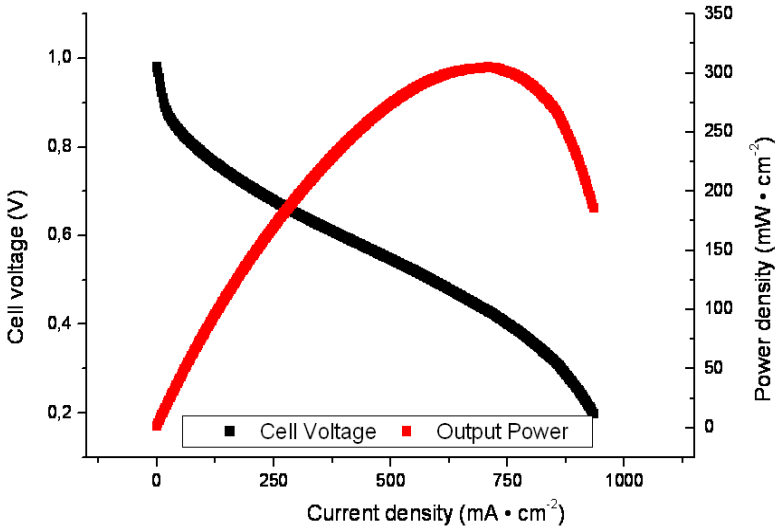

Fig. 54. *Polarization and power density versus current density using hydrogen/air flow of the fuel cell with reduced PtO_x on CNT/GDL anode at 70 °C.*

The Pt content in the anode catalyst was estimated to be about 40 μg/cm^2 of MEA. The FC test was performed at the same condition as described in previous chapter. Again we used commercial Pt/C cathode with about 2 mg/cm^2 loading of Pt. The performance of the PEMFC with the anode prepared by coating of MWCNTs by the 30 nm of PtO_x films, which were reduced in H_2 before measurements, was investigated at 70 °C. The polarization V-I curves are shown in Fig. 54 together with the power density (PD) characteristics. We can see that we obtained maximum power density PD_{max} = 305 mW/cm^2. This value corresponded to maximum specific power SP_{max} = 7.6 W/mg(Pt). Even though this value is lower than that obtained for Pt-CeO_2 catalyst, it is still one order of magnitude larger than that obtained for commercial PtRu catalyst (SP_{max} = 0.11 W/mg).

In summary, we have prepared and analyzed the platinum films with large active surface area. Such Pt nanoporous films were used as anode catalyst in PEMFC. The FC test confirmed excellent catalytic properties of the platinum nanoporous films characteristic by high performance at very low Pt loading.

CONCLUSIONS

Magnetron sputtering is a powerful deposition technique, which allows the easy combination of different dopants and oxides, which then opens the possibility of preparing a large variety of catalytic materials. This leads to the preparation of novel nano-structured materials different from those prepared by chemical methods.

In this doctoral thesis novel oxides such as CeO_2, Pt-CeO_2, Au-CeO_2 and PtO_x prepared by magnetron sputtering deposition technique were investigated.

The first chapter is devoted to investigation of the influence of different deposition parameters on structure and surface morphology of CeO_2, Pt-CeO_2 and Au-CeO_2 thin films.

Simultaneous magnetron sputtering of cerium oxide and gold/platinum allows the preparation of oxide layers continuously doped by gold/platinum atoms during the growth. It was found that the morphology of ceria based films prepared by magnetron sputtering depends on the type of substrate. It leads to the formation of very porous structure when deposited on carbon substrate. This phenomenon was explained by a simultaneous deposit growth and oxygen plasma etching of carbon during the sputtering process.

It was also shown that morphology and stoichiometry of the catalyst film vary with the deposition angle, the film thickness, inert and reactive gas flow and the deposition rate. This allows the tuning of catalyst film specific area and stoichiometry by changing the deposition parameters.

In addition, it was shown that low concentration of embedded Au or Pt atoms does not significantly influence the morphology of thin films and ceria stoichiometry, but in turn ceria stoichiometry does influences gold and platinum oxidation states, leading to the formation of high concentration of cationic gold and platinum. In case of Pt-CeO_2 co-sputtered thin films - entirely Pt^{2+} and Pt^{4+} are formed. The fully ionic Pt together with porous character of the films makes this material generally interesting as a catalyst for PEMFCs, water gas shift, CO oxidation etc.

In order to examine the activity of novel oxide catalyst prepared by magnetron sputtering, carbon nanotubes substrate were coated by porous Pt-CeO_2 catalyst, which allowed the fabrication of a large surface area catalyst supported by a highly

electrically conductive support, leading to an efficient transfer of reactants in the catalyst layer which is necessary for fuel cell reactions. Membrane electrode assembly made from a porous Pt-CeO_2 anode catalyst deposited on the gas diffusion layer covered by the CNTs revealed high activity in case of hydrogen fed PEMFC. High activity of the catalyst together with very low Pt loading resulted in high specific power SP_{max}= 124 W/mg (Pt). Except of high surface area of catalyst, high activity of Pt-CeO_2 anode was connected with the formation of fully cationic platinum. However, it requires an improved understanding of the mechanism of H_2 splitting over Pt-ceria catalyst, which remains an open question.

The results described in this chapter demonstrated that co-sputtered Pt-CeO_2 thin films are promising anode catalyst for PEMFCs which can substitute the expensive commercial catalysts due to its low cost and excellent catalytic performances. Use of the *ex-situ* prepared CNTs and sputtering techniques also makes this method convenient for large scale production of FC electrodes.

In the second chapter of this thesis, platinum oxide films were prepared by reactive magnetron sputtering of platinum in oxygen atmosphere.

According to XPS studies such thin films consist of only ionic platinum in 4+ oxidation state. Microscopy investigations showed a very flat homogeneous morphology of as-prepared oxide films.

It was shown that PtO_x films were unstable upon hydrogen exposure and undergo structural phase transition to fully reduced metallic platinum through the consumption of the lattice oxygen from the thin film due to the reduction process. According to the microscopy study, this process was accompanied with a significant roughening of the films surface.

The results described in second chapter represent a new method for the preparation of nanostructured platinum catalysts with a large surface area. Such platinum films have shown high activity when used as anode in PEM fuel cell. Platinum films prepared in such way might prove to be very interesting as a catalyst for PEM fuel cells because of their high activity and low platinum loadings.

References

[1] F. Barbir. PEM Fuel Cells: Theory and Practice. *Elsevier Academic Press*, New York, 2005, 456 pages. ISBN 0120781425.

[2] V.M. Vishnyakov. Proton exchange membrane fuel cells. *Vacuum*, 2006, **80**, 1053-1065. ISSN 0042-207X.

[3] H.A. Gasteiger, J.E. Panels, S.G. Yan. Dependence of PEM fuel cell performance on catalyst loading. *J. Power Sources*, 2004, **127**, 162-171. ISSN 0378-7753.

[4] M.S. Wilson, J.A. Valerio, S. Gottesfeld. Low platinum loading electrodes for polymer electrolyte fuel cells fabricated using thermoplastic ionomers. *Electrochim. Acta*, 1995, **40**, 355-363. ISSN 0013-4686.

[5] H.A. Gasteiger, S.S. Kocha, B. Sompalli, F.T. Wagner. Activity benchmarks and requirements for Pt, Pt-alloy, and non-Pt oxygen reduction catalysts for PEMFCs. *Appl. Catal. B*, 2005, **56**, 9-35. ISSN 0926-3373.

[6] T.S. Ahmadi, Z.L. Wang, T.C. Green, A. Henglein, M.A. El-Sayed. Shape-controlled synthesis of colloidal platinum nanoparticles. *Science*, 1996, **272**, 1924-1926. ISSN 0036-8075.

[7] P. Brault, A. Caillard, A.L. Thomann, J. Mathias, C. Charles, R.W. Boswell, S. Escribano, J. Durand, T. Sauvage. Plasma sputtering deposition of platinum into porous fuel cell electrodes. *J. Phys. D: Appl. Phys.*, 2004, **37**, 3419-3423. ISSN 0022-3727.

[8] A. Caillard, C. Charles, R. Boswell, P. Brault, C. Coutanceau. Plasma based platinum nanoaggregates deposited on carbon nanofibers improve fuel cell efficiency. *Appl. Phys. Lett.*, 2007, **90**, 223119-3. ISSN 0003-6951.

[9] E. Billy, F. Maillard, A. Morin, L. Guetaz, F. Emieux, C. Thurier, P. Doppelt, S. Donet, S. Mailley. Impact of ultra-low Pt loadings on the performance of anode/cathode in a proton-exchange membrane fuel cell. *J. Power Sources*, 2010, **195**, 2737-2746. ISSN 0378-7753.

[10] R. O'Hayre, S.J. Lee, S.W. Cha, F.B. Prinz. A sharp peak in the performance of sputtered platinum fuel cells at ultra-low platinum loading. *J. Power Sources*, 2002, **109**, 483-493. ISSN 0378-7753.

[11] S.Y. Cha, W.M. Lee. Performance of proton exchange membrane fuel cell electrodes prepared by direct deposition of ultrathin platinum on the membrane surface. *J. Electrochem. Soc.*, 1999, **146**, 4055-4060. ISSN 0013-4651.

[12] M.D. Gasda, R. Teki, T.M. Lu, N. Koratkar, G.A. Eisman, D. Gall. Sputter-deposited Pt PEM fuel cell electrodes: particles vs layers. *J. Electrochem. Soc.*, 2009, **156**, B614-B619. ISSN 0013-4651.

[13] X. Cheng, Z. Shi, N. Glass, L. Zhang, J. Zhang, D. Song, Z.S. Liu, H. Wang, J. Shen. A review of PEM hydrogen fuel cell contamination: Impacts, mechanisms, and mitigation. *J. Power Sources*, 2007, **165**, 739-756. ISSN 0378-7753.

[14] T.R. Ralph, M.P. Hogarth. Catalysis for Low Temperature Fuel Cells. *Platinum Met. Rev.*, 2002, **46**, 117-135. ISSN 0032-1400.

[15] G. Ertl, H. Knözinger, J. Weitkamp. Handbook of Heterogeneous Catalysis. *Wiley-VCH*, Weinheim, 1997, 2479 pages. ISBN 978-3-527-31241-2.

[16] T. Ioroi, Z. Siroma, N. Fujiwara, S. Yamazaki, K. Yasuda. Sub-stoichiometric titanium oxide-supported platinum electrocatalyst for polymer electrolyte fuel cells. *Electrochem. Commun*., 2005, **7**, 183-188. ISSN 1388-2481.

[17] J. Rajeswari, B. Viswanathan, T.K. Varadarajan. Tungsten trioxide nanorods as supports for platinum in methanol oxidation. *Mater. Chem. Phys*., 2007, **106**, 168-174. ISSN 0254-0584.

[18] E.C.G. Rufino, F.L.S. Purgato, P. Olivi. Investigation on the stability of Pt/C and Pt-RuO_x/C catalysts. *ECS Trans.*, 2011, **41**, 1131-1137. ISSN 1938-5862.

[19] J. Parrondo, F. Mijangos, B. Rambabu. Platinum/tin oxide/carbon cathode catalyst for high temperature PEM fuel cell. *J. Power Sources*, 2010, **195**, 3977-3983. ISSN 0378-7753.

[20] T. Mori, D.R. Ou, J. Zou, J. Drennan. Present status and future prospect of design of Pt-cerium oxide electrodes for fuel cell applications. *Prog. Nat. Sci.*, 2012, **22**, 561-571. ISSN 1002-0071.

[21] A. Dekanski, J. Stevanovic, R. Stevanovic, B.Z. Nikolic, V.M. Jovanovic. Glassy carbon electrodes I. Characterization and electrochemical activation. *Carbon*, 2001, **39**, 1195-1205. ISSN 0008-6223.

[22] F. Rodríguez-Reinoso. The role of carbon materials in heterogeneous catalysis. *Carbon*, 1998, **36**, 159-175. ISSN 0008-6223.

[23] J.M. Solar, F.J. Derbyshire, V.H.J. de Beer, L.R. Radovic. Effects of surface and structural properties of carbons on the behavior of carbon-supported molybdenum catalysts. *J. Catal.*, 1991, **129**, 330-342. ISSN 0021-9517.

[24] J.M. Solar, C.A. Leon y Leon, K. Osseo-Asare, L.R. Radovic. On the importance of the electrokinetic properties of carbons for their use as catalyst supports. *Carbon*, 1990, **28**, 369-375. ISSN 0008-6223.

[25] M.A. Farga, E. Jordao, M.J. Mendes, M.M.A. Freitas, J.L. Faria, J.L. Figueiredo. Properties of carbon-supported platinum catalysts: role of carbon surface sites. *J. Catal.*, 2002, **209**, 355-364. ISSN 0021-9517.

[26] W.H. Lizcano-Valbuena, D.C. de Azevedo, E.R. Gonzalez. Supported metal nanoparticles as electrocatalysts for low-temperature fuel cells. *Electrochim. Acta*, 2004, **49**, 1289-1295. ISSN 0013-4686.

[27] M. Watanabe, S. Saegusa, P. Stonehart. High platinum electrocatalyst utilizations for direct methanol oxidation. *J. Electroanal. Chem.*, 1989, **271**, 213-220. ISSN 0022-0728.

[28] F. Gloaguen, J.M. Leger, C. Lamy. Electrocatalytic oxidation of methanol on platinum nanoparticles electrodeposited onto porous carbon substrates. *J. Appl. Electrochem.*, 1997, **27**, 1052-1060. ISSN 0021-891X.

[29] O.V. Cherstiouk, P.A. Simonov, E.R. Savinova. Model approach to evaluate particle size effects in electrocatalysis: preparation and properties of Pt nanoparticles supported on GC and HOPG. *Electrochim. Acta*, 2003, **48**, 3851-3860. ISSN 0013-4686.

[30] P. Wang, F. Li, X. Huang, Y. Li, L. Wang. In situ electrodeposition of Pt nanoclusters on glassy carbon surface modified by monolayer choline film and their electrochemical applications. *Electrochem commun*., 2008, **10**, 195-199. ISSN 1388-2481.

[31] R. Ryoo, S.H. Joo, M. Kruk, M. Jaroniec. Ordered mesoporous carbons. *Adv. Mater.*, 2001, **13**, 677-681. ISSN 0935-9648.

[32] S.H. Joo, S.J. Choi, I. Oh, J. Kwak, Z. Liu, O. Terasaki, R. Ryoo. Ordered nanoporous arrays of carbon supporting high dispersions of platinum nanoparticles. *Nature*, 2001, **412**, 169-172. ISSN 0028-0836.

[33] N.Y. Hsu, C.C. Chien, K.T. Jeng. Characterization and enhancement of carbon nanotube-supported PtRu electrocatalyst for direct methanol fuel cell applications. *Appl. Catal. B*, 2008, **84**, 196-203. ISSN 0926-3373.

[34] Z. Tang, D.H.C. Chua. Investigation of Pt/CNT-based electrodes in proton exchange membrane fuel cells using AC impedance spectroscopy. *J. Electrochem. Soc*., 2010, **157**, B868-B873. ISSN 0013-4651.

[35] G. An, P. Yu, L. Mao, Z. Sun, Z. Liu, S. Miao, Z. Miao, K. Ding. Synthesis of PtRu/carbon nanotube composites in supercritical fluid and their application as an electrocatalyst for direct methanol fuel cells. *Carbon*, 2007, **45**, 536-542. ISSN 0008-6223.

[36] Y.M. Liang, H.M. Zhang, B.L. Yi, Z.H. Zhang, Z.C. Tan. Preparation and characterization of multi-walled carbon nanotubes supported PtRu catalysts for proton exchange membrane fuel cells. *Carbon*, 2005, **43**, 3144-3152. ISSN 0008-6223.

[37] C. Wang, M. Waje, X. Wang, J.M. Tang, R.C. Haddon, Y. Yan. Proton exchange membrane fuel cells with carbon nanotube based electrodes. *Nano Lett.*, 2004, **4**, 345-348. ISSN 1530-6984.

[38] M.S. Saha, R.Y. Li, X.H. Sun. High loading and monodispersed Pt nanoparticles on multiwalled carbon nanotubes for high performance proton exchange membrane fuel cells. *J. Power Sources*, 2008, **177**, 314-322. ISSN 0378-7753.

[39] Peter M. Martin. Handbook of deposition technologies for films and coatings: science, applications and technology. *William Andrew Publishing*, USA, 2009, 936 pages. ISBN 978-0-8155-2031-3.

[40] G. Haugstad. Atomic force microscopy: understanding basic modes and advanced applications. *John Wiley & Sons, Inc., Hoboken*, NJ, USA, 2012, 520 pages. ISBN 978-1-1183-6066-8.

[41] S. Hüfner. Photoelectron **s**pectroscopy: principles and applications. *Springer*, Berlin, 2003, 662 pages. ISBN 978-3-540-41802-3.

[42] S. Fabris, S. de Gironcoli, S. Baroni, G. Vicario, G. Balducci. Taming multiple valency with density functionals: A case study of defective ceria. *Phys. Rev. B*, 2005, **71**, 041102(R). ISSN 1098-0121.

[43] Q. Fu, H. Saltsburg, M. Flytzani-Stephanopoulos. Active nonmetallic Au and Pt species on ceria-based water-gas shift catalysts. *Science*, 2003, **301**, 935-938. ISSN 0036-8075.

[44] M. Nolan. Enhanced oxygen vacancy formation in ceria (111) and (110) surfaces doped with divalent cations. *J. Mater. Chem.*, 2011, **21**, 9160-9168. ISSN 0959-9428.

[45] C. Hardacre, R.M. Ormerod, R.M. Lambert. Platinum-promoted catalysis by ceria: A study of carbon monoxide oxidation over Pt(111)/CeO_2. *J. Phys. Chem.*, 1994, **98**, 10901-10905. ISSN 0022-3654.

[46] S. Bernal, G. Blanco, M.A. Cauqui, M.P. Corchado, C. Larese, J.M. Pintado, J.M. Rodriguez-Izquierdo. Cerium-terbium mixed oxides as alternative components for three-way catalysts: a comparative study of Pt/$CeTbO_x$ and Pt/CeO_2 model systems. *Catal. Today*, 1999, **53**, 607-612. ISSN 0920-5861.

[47] S. Bernal, G. Blanco, M.A. Cauqui, P. Corchado, J.M. Pintado, J.M. Rodriguez-Izquierdo. Oxygen buffering capacity of mixed cerium terbium oxide: a new material with potential applications in three-way catalysts. *Chem. Commun.*, 1997, **16**, 1545-1546. ISSN 1359-7345.

[48] W. Liu, M. Flytzani-Stephanopoulos. Total Oxidation of carbon-monoxide and methane over transition metal fluorite oxide composite catalysts: II. Catalyst characterization and reaction-kinetics. *J. Catal*., 1995, **153**, 317-332. ISSN 0021-9517.

[49] I. Manuel, C. Thomas, H. Colas, N. Matthess, G. Djéga-Mariadassou. A new approach in the kinetic modelling of three-way catalytic reactions. *Top. Catal.*, 2004, **30**, 311-317. ISSN 1022-5528.

[50] D. Pierre, W. Deng, M. Flytzani-Stephanopoulos. The importance of strongly bound Pt-CeO_x species for the water-gas shift reaction: catalyst activity and stability evaluation. *Top. Catal.*, 2007, **46**, 363-373. ISSN 1022-5528.

[51] X.L. Tang, B.C. Zhang, Y. Li, Y. Xu, Q. Xin, W.J. Shen. The role of Sn in Pt-Sn/CeO_2 catalysts for the complete oxidation of ethanol. *J. Mol. Catal. A: Chem.*, 2005, **235**, 122-129. ISSN 1381-1169.

[52] S. Imamura, T. Higashihara, Y. Saito, H. Aritani, H. Kanai, Y. Matsumura, N. Tsuda. Decomposition of methanol on Pt-loaded ceria. *Catal. Today*, 1999, **50**, 369-380. ISSN 0920-5861.

[53] G. Panzera, V. Modafferi, S. Candamano, A. Donato, F. Frusteri, P.L. Antonucci. CO selective oxidation on ceria-supported Au catalysts for fuel cell application. *J. Power Sources*, 2004, **135**, 177-183. ISSN 0378-7753.

[54] W.L. Deng, J. De Jesus, H. Saltsburg, M. Flytzani-Stephanopoulos. Low-content gold-ceria catalysts for the water-gas shift and preferential CO oxidation reactions. *Appl. Catal. A.*, 2005, **291**, 126-135. ISSN 0926-860X.

[55] P. Concepcion, S. Carrettin, A. Corma. Stabilization of cationic gold species on Au/CeO_2 catalysts under working conditions. *Appl. Catal. A.*, 2006, **307**, 42-45. ISSN 0926-860X.

[56] A.M. Venezia, G. Pantaleo, A. Longo, G. Di Carlo, M.P. Casaletto, F.L. Liotta, G. Deganello. Relationship between structure and CO oxidation activity of ceria-supported gold catalysts. *J. Phys. Chem. B*, 2005, **109**, 2821-2827. ISSN 1520-6106.

[57] C.L. Campos, C. Roldan, M. Aponte, Y. Ishikawa, C.R. Cabrera. Preparation and methanol oxidation catalysis of Pt-CeO_2 electrode. *J. Electroanal. Chem*., 2005, **581**, 206-215. ISSN 0022-0728.

[58] M. Takahashi, T. Mori, F. Ye, A. Vinu, H. Kobayashi, J. Drennan. Design of high-quality Pt-CeO_2 composite anodes supported by carbon black for direct methanol fuel cell application. *J. Am. Ceram. Soc*., 2007, **90**, 1291-1294. ISSN 0002-7820.

[59] A. Pfau, K.D. Schierbaum. The electronic structure of stoichiometric and reduced CeO_2 surfaces: an XPS, UPS and HREELS study. *Surf. Sci*., 1994, **321**, 71-80. ISSN 0039-6028.

[60] G. Vicario, G. Balducci, S. Fabris, S. de Gironcoli, S. Baroni. Interaction of hydrogen with cerium oxide surfaces: a quantum mechanical computational study. *J. Phys. Chem. B*, 2006, **110**, 19380-19385. ISSN 1520-6106.

[61] P. Bera, A. Gayen, M.S. Hedge, N.P. Lalla, L. Spadaro, F. Frusteri, F. Arena. Promoting effect of CeO_2 in combustion synthesized Pt/CeO_2 catalyst for CO oxidation. *J. Phys. Chem. B*, 2003, **107**, 6122-6130. ISSN 1520-6106.

[62] G. Dutta, U.V. Waghmare, T. Baidya, M.S. Hedge. Hydrogen spillover on CeO_2/Pt: enhanced storage of active hydrogen. *Chem. Mater*., 2007, **19**, 6430-6436. ISSN 0897-4756.

[63] W.T. Lim, C.H. Lee. Highly oriented ZnO thin films deposited on Ru/Si substrates. *Thin Solid Films*, 1999, **353**, 12-15. ISSN 0040-6090.

[64] E. Slavcheva, G. Gansk, G. Topalov, W. Mokwa, U. Schnakenberg. Effect of sputtering parameters on surface morphology and catalytic efficiency of thin platinum films. *Appl. Surf. Sci*., 2009, **255**, 6479-6486. ISSN 0169-4332.

[65] B. Smid, Z.J. Li, A. Dohnalkova, B.W. Arey, R.S. Smith, V. Matolin, B.D. Kay, Z. Dohnalek. Characterization of nanoporous WO_3 films grown via ballistic deposition. *J. Phys. Chem. C*, 2012, **116**, 10649-10655. ISSN 1932-7447.

[66] R.N. Tait, T. Smy, M.J. Brett. Modeling and characterization of columnar growth in evaporated films. *Thin Solid Films*, 1993, **226**, 196-201. ISSN 0040-6090.

[67] K.M. Beck, M. Henyk, C.M. Wang, P.E. Trevisanutto, P.V. Sushko, W.P. Hess, A.L. Shluger. Site-specific laser modification of MgO nanoclusters: Towards atomic-scale surface structuring. *Phys Rev. B*, 2006, **74**, 045404-5. ISSN 1098-0121.

[68] J. Kim, Z. Dohnalek, B.D. Kay. Structural characterization of nanoporous Pd films grown via ballistic deposition. *Surf. Sci*., 2005, **586**, 137-145. ISSN 0039-6028.

[69] K. Robbie, M.J. Brett. Sculptured thin films and glancing angle deposition: Growth mechanics and applications. *J. Vac. Sci. Technol. A*, 1997, **15**, 1460-1465. ISSN 0734-2101.

[70] V. Matolín, M. Cabala, V. Chab, I. Matolínová, K.C. Prince, M. Škoda, F. Šutara, T. Skála, K. Veltruská. A resonant photoelectron spectroscopy study of $Sn(O_x)$ doped CeO_2 catalysts. *Surf. Interface Anal*., 2008, **40**, 225-230. ISSN 0142-2421.

[71] X.L. Tang, B.C. Zhang, Y. Li, Y. Xu, Q. Xin, W.J. Shen. The role of Sn in Pt-Sn/CeO_2 catalysts for the complete oxidation of ethanol. *J. Mol. Catal. A: Chem*., 2005, **235**, 122-129. ISSN 1381-1169.

[72] J.R. McBride, G.W. Graham, C.R. Peters, W.H. Weber. Growth and characterization of reactively sputtered thin-film platinum oxides. *J. Appl. Phys*., 1991, **69**, 1596-1604. ISSN 0021-8979.

[73] V. Matolín, I. Matolínová, M. Václavů, I. Khalakhan, M. Vorokhta, R. Fiala, I. Piš, Z. Sofer, J. Poltierova-Vejpravova, T. Mori, V. Potin, H. Yoshikawa, S. Ueda, K. Kobayashi. Platinum-doped CeO_2 thin film catalysts prepared by magnetron sputtering. *Langmuir*, 2010, **26**, 12824-12831. ISSN 0743-7463.

[74] V. Matolín, I. Khalakhan, I. Matolínová, M. Václavů, K. Veltruská, M. Vorokhta. $Pt^{2+,4+}$ ions in CeO_2 rf-sputtered thin films. *Surf. Interface Anal*., 2010, **42**, 882-885. ISSN 0142-2421.

[75] V. Matolín, R. Fiala, I. Khalakhan, J. Lavková, M. Václavů, M. Vorokhta. Nanoporous Pt^{n+}-CeO_x catalyst films grown on carbon substrates. *Int. J. Nanotechnol*., 2012, **9**, 680-694. ISSN 1475-7435.

[76] I. Matolínová, R. Fiala, I. Khalakhan, M. Vorokhta, Z. Sofer, H. Yoshikawa, K. Kobayashi, V. Matolín. Synchrotron radiation photoelectron spectroscopy study of metal-oxide thin film catalysts: Pt-CeO_2 coated CNTs. *Appl. Surf. Sci*., 2012, **258**, 2161-2164. ISSN 0169-4332.

[77] M. Vorokhta, I. Khalakhan, I. Matolínová, M. Kobata, H. Yoshikawa, K. Kobayashi, V. Matolín. Nanostructured Pt-CeO_2 thin film catalyst grown on graphite foil by magnetron sputtering. *Appl. Surf. Sci*., 2013, **267**, 119-123. ISSN 0169-4332.

[78] T. Skála, F. Šutara, K.C. Prince, V. Matolín. Cerium oxide stoichiometry alteration via Sn deposition: Influence of temperature. *J. Electron. Spectrosc. Relat. Phenom*., 2009, **169**, 20-25. ISSN 0368-2048.

[79] V. Matolín, M. Cabala, I. Matolínová, M. Škoda, J. Libra, M. Václavů, K.C. Prince, T. Skála, H. Yoshikawa, Y. Yamashita, S. Ueda, K. Kobayashi. Au^+ and Au^{3+} ions in CeO_2 rf-sputtered thin films. *J. Phys. D: Appl. Phys*., 2009, **42**, 115301-6. ISSN 0022-3727.

[80] Y.C. Liu, L.C. Juang. Electrochemical methods for the preparation of gold-coated TiO_2 nanoparticles with variable coverages. *Langmuir*, 2004, **20**, 6951-6955. ISSN 0743-7463.

[81] G. Ertas, U.K. Demirok, S. Suzer. Enhanced peak separation in XPS with external biasing. *Appl. Surf. Sci*., 2005, **249**, 12-15. ISSN 0169-4332.

[82] I. Khalakhan, M. Vorokhta, M. Chundak, V. Matolín. Au-CeO_2 nanoporous films/carbon nanotubes composites prepared by magnetron sputtering. *Appl. Surf. Sci.*, 2013, **267**, 150-153. ISSN 0169-4332.

[83] I. Radev, E. Slavcheva, E. Budevski. Investigation of nanostructured platinum based membrane electrode assemblies in “EasyTest” cell. *Int. J. Hydrogen Energy*, 2007, **32**, 872-877. ISSN 0360-3199.

[84] N. Um, M. Miyake, T. Hirato. Dissolution of cerium oxide in sulfuric acid. *Zero-Carbon Energy Kyoto* 2011, *Springer*, 2011, 165-170. ISBN: 978-4-431-53909-4.

[85] N.M.D. Brown, N. Cui, A. McKinley. A study of the topography of a glassy carbon surface following low-power radio-frequency oxygen plasma treatment. *Appl. Surf. Sci*., 1998, **133**, 157-165. ISSN 0169-4332.

[86] H.X. You, N.M.D. Brown, K.F. Al-Assadi. Radio-frequency (RF) plasma etching of graphite with oxygen: a scanning tunnelling microscope study. *Surf. Sci*., 1993, **284**, 263-272. ISSN 0039-6028.

[87] A. Rizk, L. Holland. Sputtering and chemical etching of carbon in a dc glow discharge. *Vacuum*, 1977, **27**, 601-604. ISSN 0042-207X.

[88] Z. Hou, B. Cai, H. Liu, D. Xu. Ar, O_2, CHF_3, and SF_6 plasma treatments of screen-printed carbon nanotube films for electrode applications. *Carbon*, 2008, **46**, 405-413. ISSN 0008-6223.

[89] I. Khalakhan, M. Dubau, S. Haviar, J. Lavková, I. Matolínová, V. Potin, M. Vorokhta, V. Matolín. Growth of nano-porous Pt-doped cerium oxide thin films on glassy carbon substrate. *Ceram. Int.*, 2013, **39**, 3765-3769. ISSN 0272-8842.

[90] I. Petrov, P.B. Barna, L. Hultman, J.E. Greene. Microstructural evolution during film growth. *J. Vac. Sci. Technol. A*, 2003, **21**, 117-128. ISSN 0734-2101.

[91] G.S. Selwyn. Spatially resolved detection of O atoms in etching plasmas by two-photon laser-induced fluorescence. *J. Appl. Phys*., 1986, **60**, 2771-4. ISSN 0021-8979.

[92] M.A. Hartney, D.W. Hess, D.S. Soane. Oxygen plasma etching for resist stripping and multilayer lithography. *J. Vac. Sci. Technol. B*, 1989, **7**, 1-13. ISSN 1071-1023.

[93] M.A. Baker. Plasma cleaning and the removal of carbon from metal surfaces. *Thin solid films*, 1980, **69**, 359-368. ISSN 0040-6090.

[94] G.Q. Lu, C.Y. Wang, T.J. Yen, X. Zhang. Development and characterization of a silicon-based micro direct methanol fuel cell. *Electrochim. Acta*, 2004, **49**, 821-828. ISSN 0013-4686.

[95] R. Fiala, I. Khalakhan, I. Matolínová, M. Václavů, M. Vorokhta, Z. Sofer, S. Huber, V. Potin, V. Matolín. Pt-CeO_2 coating of carbon nanotubes grown on anode gas diffusion layer of the polymer electrolyte membrane fuel cell. *J. Nanosci. Nanotechnol*., 2011, **11**, 5062-5067. ISSN 1533-4880.

[96] G.N. Vayssilov, Y. Lykhach, A. Migani, T. Staudt, G.P. Petrova, N. Tsud, T. Skala, A. Bruix, F. Illas, K.C. Prince, V. Matolín, K.M. Neyman, J. Libuda. Support nanostructure boosts oxygen transfer to catalytically active platinum nanoparticles. *Nat. Mater.*, 2011, **10**, 310-315. ISSN 1476-1122.

[97] M.D. Ackermann, T.M. Pedersen, B.L.M. Hendriksen, O. Robach, S.C. Bobaru, I. Popa, C. Quiros, H. Kim, B. Hammer, S. Ferrer, J.W.M. Frenken. Structure and Reactivity of Surface Oxides on Pt(110) during Catalytic CO Oxidation. *Phys. Rev. Lett.*, 2005, **95**, 255505-4. ISSN 0031-9007.

[98] H.P. Bonzel, R. Ku. Mechanisms of the catalytic carbon monoxide oxidation on Pt (110). *Surf. Sci.*, 1972, **33**, 91-106. ISSN 0039-6028.

[99] W.D. Westwood, C.D. Bennewitz. Formation of PtO films by reactive sputtering. *J. Appl. Phys.*, 1974, **45**, 2313-2316. ISSN 0021-8979.

[100] Y. Abe, M. Kawamura, K. Sasaki. Preparation of PtO and α-PtO_2 thin films by reactive sputtering and their electrical properties. *Jpn. J. Appl. Phys.*, 1999, **38**, 2092-2096. ISSN 0021-4922.

[101] N. Seriani, Z. Jin, W. Pompe, L.C. Ciacchi. Density functional theory study of platinum oxides: From infinite crystals to nanoscopic particles. *Phys. Rev. B*, 2007, **76**, 155421-10. ISSN 1098-0121.

[102] O. Muller, R. Roy. Formation and stability of the platinum and rhodium oxides at high oxygen pressures and the structures of Pt_3O_4, β-PtO_2 and RhO_2. *J. Less-Comm. Met.*, 1968, **16**, 129-146. ISSN 0022-5088.

[103] D. Cahen, J.A. Ibers, J.B. Wagner. Platinum bronzes. IV. Preparation, crystal chemistry, and physical properties. *Inorg. Chem.*, 1974, **13**, 1377-1388. ISSN 0020-1669.

[104] R.D. Shannon. Synthesis and properties of two new members of the rutile family RhO_2 and PtO_2. *Solid State Commun.*, 1968, **6**, 139-143. ISSN 0038-1098.

[105] D.B. Rogers, R.D. Shannon, A.W. Sleight, J.L. Gillson. Crystal chemistry of metal dioxides with rutile-related structures. *Inorg. Chem.*, 1969, **8**, 841-849. ISSN 0020-1669.

[106] L. Maya, L. Riester, T. Thundat, S. Yust. Characterization of sputtered amorphous platinum dioxide films. *J. Appl. Phys.*, 1998, **84**, 6382-6386. ISSN 0021-8979.

[107] C.R. Aita. Optical behavior of sputter-deposited platinum-oxide films. *J. Appl. Phys*., 1985, **58**, 3169-3173. ISSN 0021-8979.

[108] H. Neff, S. Henkel, E. Hartmannsgruber, E. Steinbeiss, W. Michalke, K. Steenbeck, H.G. Schmidt. Structural, optical, and electronic properties of magnetron-sputtered platinum oxide films. *J. Appl. Phys*., 1996, **79**, 7672-7675. ISSN 0021-8979.

[109] M.C. Jung, H.D. Kim, M. Han, W. Jo, D.C. Kim. X-ray photoelectron spectroscopy study of Pt-oxide thin films deposited by reactive sputtering using O-2/Ar gas mixtures. *Jpn. J. Appl. Phys., Part 1: Regular Papers and Short Notes and Review Papers,* 1999, **38**, 4872-4875. ISSN 0021-4922.

[110] J.J. Blackstock, D.R. Stewart, Z. Li. Plasma-produced ultra-thin platinum-oxide films for nanoelectronics: physical characterization. *Appl. Phys. A: Mater. Sci. Process*, 2005, **80**, 1343-1353. ISSN 0947-8396.

[111] M. Hecq, A. Hecq, J.P. Delrue, T. Robert. Sputtering deposition, XPS and X-ray diffraction characterization of oxygen-platinum compounds. *J. Less-Comm. Met*., 1979, **64**, P25-P37. ISSN 0022-5088.

[112] W.L. Masterton, J.J. Demo Jr. Reduction of oxides by hydrogen: A quantitative experiment for general chemistry laboratory. *J. Chem. Educ*., 1958, **35**, 242-244. ISSN 0021-9584.

[113] X.L. Tang, B.C. Zhang, Y. Li, Y. Xu, Q. Xin, W.J. Shen. The role of Sn in Pt-Sn/CeO_2 catalysts for the complete oxidation of ethanol. *J. Mol. Catal. A: Chem*., 2005, **235**, 122-129. ISSN 1381-1169.

[114] M.A. Henderson. The interaction of water with solid surfaces: fundamental aspects revisited. *Surf. Sci. Rep*., 2002, **46**, 1-308. ISSN 0167-5729.

[115] W.P. Lee, A.F. Routh. Why Do Drying Films Crack? *Langmuir*, 2004, **20**, 9885-9888. ISSN 0743-7463.

List of Tables

List of Abbreviations

AFM	Atomic Force Microscope
BSE	Backscatter Electron
CNT	Carbon Nanotubes
CVD	Chemical Vapor Deposition
DC	Direct Current
DFT	Density Functional Theory
DMF	Dimethylformamide
EDS	Energy Dispersive X-ray Spectrometer
FIB	Focused Ion Beam
GC	Glassy Carbon
GDL	Gas Diffusion Layer
GLAD	Glancing Angle Deposition
HOPG	Highly Ordered Pyrolytic Graphite
MEA	Membrane Electrode Assembly
MWCNT	Multiwall Carbon Nanotubes
ND	Normal Deposition
PD	Power Density
PEM	Polymer Electrolyte Membrane (Proton Exchange Membrane)
PEMFC	Proton Exchange Membrane Fuel Cell
PVD	Physical Vapor Deposition
RF	Radio Frequency
SE	Secondary Electron
SEM	Scanning Electron Microscope
SP	Specific Power
TEM	Transmission Electron Microscope
UHV	Ultra-High Vacuum
XPS	X-ray Photoelectron Spectroscopy